PONTIFICIA UNIVERSIDAD CATÓLICA DEL PERÚ

Escuela de Posgrado

Advances in Quantum State Tomography and Strong
Measurements of Quantum Weak Values

Tesis para obtener el grado académico de Doctor en Física que
presenta:

David Reinaldo Alejandro Ruelas Paredes

Asesor:

Eduardo Rubén Massoni Kamimoto

Lima, 2023

Informe de Similitud

Yo, Eduardo Ruben Massoni Kamimoto , docente de la Escuela de Posgrado de la Pontificia Universidad Católica del Perú, asesor de la tesis del trabajo de investigación titulado: *"Advances in Quantum State Tomography and Strong Measurements of Quantum Weak Values"*, del autor David Reinaldo Alejandro Ruelas Paredes

dejo constancia de lo siguiente:

- El mencionado documento tiene un índice de puntuación de similitud de 11%. Así lo consigna el reporte de similitud emitido por el software *Turnitin* el 25/10/2023.
- He revisado con detalle dicho reporte y la Tesis o Trabajo de Suficiencia Profesional, y no se advierte indicios de plagio.
- Las citas a otros autores y sus respectivas referencias cumplen con las pautas académicas.

Lugar y fecha: Lima, 25 de octubre de 2023

Apellidos y nombres del asesor: Massoni Kamimoto Eduardo Ruben	
DNI: 07465269 ORCID: 0000-0002-8333-6954	Firma

Advances in Quantum State Tomography and Strong Measurements of Quantum Weak Values

David Reinaldo Alejandro Ruelas Paredes

Propuesto para el Grado de Doctor en Física

2023

Resumen

Este trabajo contiene dos contribuciones al campo de la teoría cuántica. La primera viene por doble partida: un protocolo óptico para producir y realizar tomografía de estados puros, arbitrarios, de dos qubits codificados en grados de libertad de camino y polarización; y un protocolo generalizado para hacer tomografía de estados mixtos del mismo tipo. Se reporta una realización con luz láser del primer esquema, la cual sirve como prueba de concepto. La segunda contribución es un modelo dentro del paradigma de von Neumann para las mediciones. Su utilidad yace en que permite estudiar el efecto de la fuerza del acoplamiento entre sistema y puntero sobre la incertidumbre estadística y los errores sistemáticos que resultan de medir valores débiles cuánticos y estados puros. Esta propuesta –cuya implementación con luz láser o con fotones individuales es también explicada– fue demostrada usando sistemas de computación cuántica provistos por IBM. Los resultados obtenidos mediante mediciones con distintos grados de fuerza disipan la idea de que las mediciones fuertes siempre dan mejores resultados que sus contrapartes débiles. Quizá más importante todavía, esta realización experimental aporta evidencia de que es posible maximizar la precisión y exactitud de los parámetros medidos si se elige adecuadamente el acoplamiento de la medición.

Advances in Quantum State Tomography and Strong Measurements of Quantum Weak Values

David Reinaldo Alejandro Ruelas Paredes

Presented in candidacy for the degree of Doctor in Physics

2023

Abstract

This work consists of two contributions to the broader field of quantum theory. The first contribution is twofold: an all-optical protocol for producing and measuring arbitrary, pure, two-qubit states that are encoded in path and polarization degrees of freedom; and a generalized protocol for characterizing mixed states of the same kind. A laser light realization of the former scheme is reported, which serves as a proof of principle. The second contribution concerns a model within the von Neumann measurement paradigm. Its usefulness lies in that it enables the study of what effects system-pointer coupling strength has on the statistical uncertainty and systematic errors arising from the measurement of quantum weak values and pure states. This proposal – whose implementation with laser light or individual photons is also explained – was demonstrated in IBM's quantum computing systems. The results obtained in a range of measurement strengths dispel the notion that strong measurements always perform better than their weaker counterparts. Perhaps more importantly, this experimental realization provides evidence that it is possible to maximize the precision and accuracy of the measured parameters with a properly chosen coupling.

Acknowledgements

A lot of people worked with me and helped me out throughout my spell at the Quantum Optics Group. I am deeply thankful to Ricardo and Niel of the Physics Department for all the work they do and the immense practical help they have provided for generations of physicists, especially for my colleagues and I. Along these lines, I would also like to thank Yonny Yugra for his guidance and advice in all my experimental endeavors. Elmer Suárez and Diego Barberena hold a special place in this list because of their immense patience and comradery during my first months at the Quantum Optics Group. Thank you all.

My lab mates Jean Paul Marrou and Carlos Montenegro did a big part of the work that eventually became our first published paper in the Group. For that and for their patience in dealing with my impatient self, I am tremendously thankful.

My former lab mate Mariano Uria's influence in my graduate studies cannot be understated. Just to mention his contributions in the past couple of years, he provided the context and know-how for working with IBM's quantum systems, completed the weak value measurement proposal, carried out many simulations and experiments, and shared comments on an earlier draft of this document. Were it not for him, probably this entire work would outright not exist. Thank you so much for all your help.

Professors Pankaj Agrawal and Sk Sazim generously advised me while I flirted with the idea of delving into the study of quantum correlations. In the end, I opted for a different path. But, for their help and encouragement, I owe them my gratitude.

I also thank professors Alberto Gago, Pepe Bazo, and Rolf Grieseler, whose disinterested help made this dissertation possible. On these grounds as well as on countless others, I thank my bosses and colleagues, professors Francisco De Zela and Eduardo

Massoni. They were supportive, considerate, and understanding from day one, and a huge help all the way through to the last day. My deepest thanks to both of you.

I would also like to thank my non-work friends, who made my life better and nicer to transit. And finally, my parents, on whose love and labor every good thing in my life is built, which makes me feel more grateful and blessed than I will ever be able to properly convey. Thank you both, always.

Contents

List of Figures

Chapter 1

Introduction

In this first chapter, I introduce the overarching themes of the present thesis, motivate the schemes proposed and reported in chapters 2 and 3, and provide the necessary background for their discussion.

1.1 Overview

Quantum mechanics is a broad, sprawling field of knowledge and research. Within it, foundational topics such as entanglement [1, 2] (a type of correlation believed for decades to be the distinguishing feature of quantum systems), locality [2–4] (the property whereby two or more systems are statistically independent from one another), and the mathematical description of measurements [5] (the processes that destroy the current state of a system in order to extract probabilistic information from it) have birthed a breadth of intertwined disciplines that seem inexhaustible. One of the most exciting and fast-growing of them is quantum information theory. In classical information theory–more commonly known simply as information theory–information is conveyed by a sender to a receiver via a carrier. When the carriers are quantum systems, a non-classical treatment becomes necessary and unexpected results follow suit. Roughly speaking, quantum information theory encompasses the study of how quantum systems transmit, store, and process information. Nearly half a century of inquiry in this subject has, in turn, brought about new fields with a life of their own. Let us explore three such cases.

First, the inescapable task of ascertaining quantum states has created the discipline known as *quantum state tomography*, which studies methods that characterize experimental states and their uncertainties in ever more efficient and advantageous ways.

Second, the potential, enabled by entanglement and/or other quantum correlations [6–9], for computational power far exceeding that of traditional computers has, for its part, engendered a new domain of both basic science and technology: *quantum computation*. Although actual realizations of its preeminent promises, such as the factorization of large integers [10] and efficient search in databases [11], are still pending, significant progress has been made so far. Current research on quantum computation is carried out in large part by private companies [12], some of whose devices can be accessed for free by people all over the world through cloud services. The availability of these powerful instruments advances a plethora of research subjects [13–16]. And third, the study of philosophical questions regarding the arrow of time has produced a curious type of objects, christened *quantum weak values* [17]. Since their appearance, they have been used for both theoretical and experimental explorations [18–23], perhaps most interestingly at the frontiers of quantum theory [24–27], as well as in an impressive range of experimental applications such as signal amplification, quantum state characterization, and the measurement of quantities of physical interest [28].

The adjective "quantum" has qualified all topics thus far mentioned. However, an important through-line that connects all of them is the existence of analogs in classical systems. More than two decades ago [29, 30], scientists had arrived at a signal insight: many properties of the phenomena that fall under the scope of quantum information theory stem from the wave nature of states, which evidently does not pertain exclusively to the realm of quantum systems. A wealth of studies have shown that Bell-type inequality violations [31–36], information theoretical protocols [37–39], and weak values [19, 40–43] occur also in classical light experiments. The thread that knits together these subjects at a fundamental level is the linear vector space nature of their mathematical descriptions. The proposals and results hereafter reported represent further manifestations of this fact.

The aim of this thesis is twofold. First, it will deal with two proposals for performing state tomography in experiments with either classical light (laser beams) or quantum light (individual photons); one of them concerns pure states, whereas the other refers to arbitrary mixed states. To this end, in section 1.2 I will give an overview of the literature on quantum state tomography–with special emphasis on the works that directly set the stage for the present contributions–which will motivate and lay the groundwork for

2

the proposals. In chapter 2, I will introduce the protocols, comment on their realization, and show the experimental results of a proof of principle for the pure state protocol that was implemented in a classical light setting [44]. Second, this thesis will set forth a scheme for the measurement of weak values in experiments where the interaction between system and pointer is not constrained to being "weak". At first sight, this assertion may seem contradictory. Rather, it reflects the fact that the name "weak values" owes its permanence in the community's parlance only to historical reasons. This idea was inspired on work done by Denkmayr *et al.* [45, 46], but instead of putting it to test in neutron interferometry experiments, as in the original papers, my colleagues and I carried it out in quantum computers facilitated by the International Business Machines (IBM) Corporation. In section 1.3, I will motivate the formal definition of weak values, trace the history of their empirical realizations, and focus in on previous studies on the relation between strong measurements and weak values. For conceptual clarity and completeness, in section 1.4 I will also outline the foundational literature on quantum computation, the basic functioning of superconducting quantum computers, and the use of IBM's cloud-based quantum systems. Thereafter, in chapter 3 I will generalize and extend Denkmayr *et al.*'s model, as well as present the results of its quantum computational implementation. Finally, in chapter 4 I will summarize the work done and suggest possible research questions that arise from it.

1.2 Quantum State Tomography

The postulates of quantum mechanics dictate that, when a system is measured, its state is projected onto the subspace corresponding to the recorded eigenvalue of the observable under consideration.[1] Such a dictum makes it impossible to both know the state of a single system and preserve it. Yet, in certain contexts, a source of essentially infinite copies of the same state is available. In such cases, we can extract information about the state–or even completely specify it–by measuring an appropriate set of operators and combining the outcomes. The families of protocols which, from minimal assumptions about the state's nature, reconstruct the wave function or density matrix of interest via repeated measurements on copies of a system (whose state is assumed to be constant)

---

1. See, e.g., section III.B.3.c of volume 1 of [47] or section 1.4 of [48].

comprise the corpus known as quantum state tomography. By definition, these schemes work for arbitrary states of a given kind, so they are said to be *universal*.

Despite prior theoretical models that aimed at obtaining a complete experimental description of states [49–52], quantum state tomography was born from quantum optics – more specifically, from a proposal made by Vogel and Risken in 1989 [53] for converting so-called quadrature probability densities into the Wigner function W, wherefrom the quantum state in the form of a density matrix can be computed.[2] The set of steps required to achieve this conversion from raw data into the desired state are called *postprocessing*. We shall use this term in a general sense, even though it has occasionally appeared in the literature with somewhat different meanings [28, 56, 57]. Since mathematical methods imported from the discipline of medical tomographic imaging are utilized for postprocessing in Vogel and Risken's framework, the name quantum state tomography smoothly transitioned into the lexicon [55].

In the 1990s, quantum tomography schemes served to reconstruct vacuum and quadrature-squeezed states of light [58], squeezed states of light [59], and phase-modulated states [60], to name a few examples. At the same time, tomography was also implemented in contexts outside of quantum optics: 9-dimensional hydrogen states [61], infinitely dimensional diatomic molecular vibration states [62], and two-qubit states encoded in the spin of carbon and hydrogen nuclei [63], too, were successfully characterized. But a limitation of tomography protocols soon emerged: because of experimental uncertainties in the measured probabilities, the resulting density matrices do not always have positive eigenvalues, which renders them unphysical and invalid for various calculations. In such cases, the logical approach would entail finding a *constrained estimator* for the density operator – i.e., a matrix that is consistent with the measured data and represents a physical state.[3] Several estimation methods have been developed over the decades [64]. Of historical importance is Hradil's 1997 suggestion of a technique based on *maximum likelihood estimation* as a solution [65]. Hradil's outline of its general implementation was quickly built upon [66, 67] and deployed in multiple

---

2. For more details on the early developments of tomography, especially in the province of quantum optics, see chapters 1 and 3 of [54] and section I of [55].

3. While state estimation is part of the postprocessing stage, it is not always necessary: many tomography protocols, most manifestly those for pure states, produce valid results by construction (see, e.g., sections 2.1.2 and 3.2.2).

laboratory settings.

Among these, James *et al.*'s 2001 implementation of maximum likelihood estimation in polarization tomography [68] stands out as the most relevant to the present work. After proving the general result that arbitrary, n-qubit state tomography can be done with 4^n measurements, the authors expounded the protocol for two-qubit states in which the qubits are the polarization of photon pairs created through the process known as spontaneous parametric downconversion.[4] They prescribed a set of 16 photon-count measurements and derived a formula for reconstructing two-qubit states as linear functions of said outcomes. As noted above, this prescription often produces density matrices that are not positive semidefinite, so they cannot be used to compute quantities which depend on their eigenvalues–e.g., von Neumann entropy, Wootters concurrence, and quantum discord. Such a drawback could doom any attempt at employing this protocol in research on quantum information. James *et al.* overcame this difficulty by concocting and demonstrating a practical implementation of maximum likelihood estimation that has since become standard practice in the field.

An improvement on James *et al.*'s work was presented in 2008 by de Burgh *et al.* [71]. Although the one- and two-qubit measurement sets prescribed in [68] are *optimal*– i.e., they consist of the minimum number of measurements necessary for completely determining the state–they are by no means the best ones. The authors of [71] related different one- and two-qubit tomography sets to the quality of the reconstructed state, as quantified by a figure of merit such as fidelity[5] or the quantum Chernoff bound. The measurement sets advanced by de Burgh *et al.* are obtained by considering Platonic solids–the tetrahedron (4 faces), cube (6), octahedron (8), dodecahedron (12), and icosahedron (20)–and picturing the Bloch sphere inscribed in each of them, which is tangent to each face at its center. With this picture in mind, the tetrahedron set is comprised of the 4 Bloch vectors that coincide with the tangent points of the sphere, and higher order sets are defined in a similar fashion. As shown in [71], these Platonic measurement sets perform much better than those of James *et al.*, even when the sets are of

---

4. See, for example, [69, 70] for modern introductory reviews on the production of photon pairs.

5. By definition, the fidelity $\mathcal{F}$ between two density operators ρ_1 and ρ_2 is $\mathcal{F}(\rho_1, \rho_2) \equiv \mathrm{Tr}\sqrt{\sqrt{\rho_1}\rho_2\sqrt{\rho_1}}$. If one of the density operators represents a pure state, this expression simplifies to $\mathcal{F}(|\psi_1\rangle\langle\psi_1|, \rho_2) = \sqrt{\langle\psi_1|\rho_2|\psi_1\rangle}$. If both are pure states, their fidelity further reduces to $\mathcal{F}(|\psi_1\rangle\langle\psi_1|, |\psi_2\rangle\langle\psi_2|) = |\langle\psi_1|\psi_2\rangle|$ (see, e.g., section 9.2.2 of [72] for more details).

the same size (the tetrahedron for single qubits; the tensor product of two tetrahedrons for two-qubits). Larger improvements, alas, come at a sizable cost: already the two-qubit cube set requires of 36 measurements, more than double the size of the optimal set.

In any event, the cardinalities of the measurement sets proposed in [68] and, most markedly, in [71] stand in stark contrast to two later results undergirded by the assumption that the target states are pure. The first comes from Ma *et al.*'s study of the minimum number of measurements needed to identify pure states unequivocally [73]. More precisely, let $\mathbf{A}$ be a set of m linearly independent observables and $\boldsymbol{\alpha}$ the set of m outcomes that result from a measurement of $\mathbf{A}$ on some state. We say that a pure state is *uniquely determined among all pure states* (UDP) by measuring $\mathbf{A}$ when there exists no other pure state which would yield the same $\boldsymbol{\alpha}$ when $\mathbf{A}$ is measured on it. Similarly, we say that a pure state is *uniquely determined among all states* (UDA) by measuring $\mathbf{A}$ when there exists no other state (either pure or mixed) which returns the same $\boldsymbol{\alpha}$ upon a measurement of $\mathbf{A}$. There is not a unique set $\mathbf{A}$ for which a given state is UDP or UDA; further, these sets can have different sizes. We can expect that the smallest set for which a pure state is UDA would be larger than the smallest set for which it is UDP: after all, since they are equivalent to density matrices with one eigenvalue equal to 1 and the rest to 0, pure states make up a minuscule subset (of measure zero) of the set of all states. Ma *et al.* found that all pure, two-qubit states are UDA from just 11 measurements, whereas James *et al.* [68] had shown that any two-qubit state can be UDA with $4^2 = 16$. For three-qubit states, the comparison is more striking: pure states can be UDA from 31 measurements [73], instead of the $4^3 = 64$ required for full tomography. Purity, we must conclude, unleashes the potential for much less resource-intensive reconstruction of quantum states.

Second, and closely related to Ma *et al.*'s results, were Heinosaari *et al.*'s findings [74] about the smallest number of measurements, denoted by $\mathfrak{m}$, that can uniquely determine any pure state ("an unknown quantum state which is constrained by prior information", in the authors' words) among all pure states. The results of [74] relevant for our purposes are upper and lower bounds on $\mathfrak{m}$ for states of dimension $d = 4$. Heinosaari *et al.*'s Theorem 3 establishes $4d - 5 - \alpha$ as an upper bound of $\mathfrak{m}$ for even $d \geq 4$, with α being the number of 1s in the binary form of $d - 1$, i.e. 2 in the case that occupies us because $(d-1)_{10} = 3_{10} = 11_2$. Theorem 6 of [74] states that $\mathfrak{m} > 4d - 4 - 2\alpha$.

For $d = 4$ (as well as for $d \leq 7$) both bounds give a definite result: $\mathfrak{m} = 9$ is the size of the optimal set of measurements for uniquely determining any pure state among all pure states.

A recent paper by Gonzales *et al.* [75] put forward a procedure for uniquely determining pure, two-qubit states among all pure states. In a nutshell, they present an all-optical setup that produces and characterizes arbitrary pure states encoded in the path and polarization degrees of freedom of laser light that propagates through an interferometer. Gonzales *et al.*'s characterization algorithm prescribes 9 measurements–two instances of single-qubit tomography, which account for 8 measurements, and one interferometric measurement–the theoretical minimum found by Heinosaari *et al.* Unfortunately, their proposal entails a host of problems. On a practical level, the protocol requires utmost precision when preparing the state's phases, necessitates an stabilizing electronic circuit, and demands drastically changing the layout of the instruments–by inserting new ones inside the arrangement–in the interferometric step. But its fundamental flaw is that this scheme does not work without knowledge of the target state, for it determines the experimental state up to the sign of one phase. Thence, it is not, *stricto sensu*, a tomography protocol.

In short order, my colleagues and I managed to overcome the drawbacks of [75]. We developed a protocol, also for path-polarization systems, that by simply shifting optical instruments to specific configurations can easily generate arbitrary pure states (see section 2.1.1), and by performing 12 measurements can completely determine said states without any need for knowledge of the target state (see section 2.1.2). Our proposal, nonetheless, still left open the question of how to characterize mixed, path-polarization states. In this dissertation, I introduce the missing mixed state tomography protocol, which consists of 16 measurements, generalizes the foregoing pure state scheme naturally (section 2.2.1), and calls for an estimation procedure to impose physicality (section 2.2.2). As a proof of principle for the pure state proposal, our group carried out multiple experiments which put it to test [44]. The results (section 2.3) are in excellent agreement with the predictions, which attests the validity of the protocol.

1.3 Quantum Weak Values

Quantum weak values were first defined by Aharonov, Albert, and Vaidman in 1988 [17] when addressing the apparently unphysical outcomes of certain measurements, which they called "weak measurements". More in general, a von Neumann measurement[6] on a quantum system S requires an ancilla system, conventionally referred to as pointer, P, whose coupling to S is described by an interaction Hamiltonian of the form[7]

$$H_{\text{int}} = gA_S \otimes B_P = gA_S B_P. \tag{1.1}$$

In the above equation, g is, in general, a function of time that determines the coupling (or, equivalently, the interaction) strength, A_S represents an observable of the system, and B_P an observable of the pointer that we interpret as a momentum operator–i.e., $B_P|p\rangle = p|p\rangle$. Accordingly, there exists a position observable in the pointer space, X_P, conjugated to the momentum: $X_P|x\rangle = x|x\rangle$ and $[X_P, B_P] = i$, in the continuous case, with $\hbar = 1$. For example, consider the neutron interferometry experimental setting of [45, 46, 77], and let S be the neutrons' spin and P the path they follow inside the interferometer, wherein a magnetic field of magnitude B_z is applied along an axis perpendicular to both paths. If the field points upwards for neutrons in path 0_P and downwards in path 1_P, the interaction Hamiltonian has the form

$$H_{\text{int}} = -\mu B_z \sigma_S^z |0_P\rangle\langle 0_P| + \mu B_z \sigma_S^z |1_P\rangle\langle 1_P| = -\mu B_z \sigma_S^z \sigma_P^z, \tag{1.2}$$

where μ is the neutron's magnetic moment and $\sigma_{S,P}^z$ are system and pointer Pauli spin operators. The strength of the measurement, hence, depends on the field intensity. Typically, the measured value of the system observable A_S is proportional to the shift in the pointer's position. To see this, let us assume the general superposition

$$|\psi_S\rangle = \sum_n \alpha_n |a_n\rangle, \quad \text{with} \quad A_S|a_n\rangle = a_n|a_n\rangle, \tag{1.3}$$

as the initial system state, and $|\Phi(0)\rangle$, a Gaussian wave packet centered at $x = 0$ with spread σ, as that of the pointer. In the momentum representation, this pointer state is

---

6. See pp. 442–445 of [5] for the original formulation of this measurement model. A modern, accessible account of it and a proposal for its optical implementation are given in [76].

7. Throughout this thesis, the tensor product symbol is usually omitted for notational simplicity, but its presence will be brought up in some places where a reminder may be convenient.

centered at $p = 0$, has a spread $1/\sigma$, and reads

$$|\eta_P\rangle = |\Phi(0)\rangle = \int \mathrm{d}p\, \tilde{\phi}(p)|p\rangle = \int \mathrm{d}p \left(\frac{2\sigma^2}{\pi}\right)^{1/4} \exp\left(-\sigma^2 p^2\right)|p\rangle. \tag{1.4}$$

That the system and pointer states become entangled during the interaction is proved by employing the evolution operator

$$U(\epsilon) \equiv \exp\left(-i \int_0^{\Delta t} \mathrm{d}t'\, H_{\text{int}}\right) = \exp(-i\epsilon A_S B_P), \tag{1.5}$$

where $\epsilon \equiv \int_0^{\Delta t} g\, \mathrm{d}t'$, a parameter we will consider positive, quantifies the coupling strength.[8] The exponential in equation 1.5 is expanded in terms of the eigenprojectors of $A_S B_P$, and then applied on the initial state. After collapsing one sum and one integral, we are left with

$$U(\epsilon)|\psi_S\rangle|\eta_P\rangle = \sum_n \alpha_n \int \mathrm{d}p \exp(-i\epsilon a_n p)\, \tilde{\phi}(p)|a_n\rangle|p\rangle. \tag{1.6}$$

We now insert the pointer-space identity operator in the form $\int \mathrm{d}x\, |x\rangle\langle x|$ and get

$$\begin{aligned} U(\epsilon)|\psi_S\rangle|\eta_P\rangle &= \sum_n \alpha_n|a_n\rangle \int \mathrm{d}p \exp(-ip\epsilon a_n)\, \tilde{\phi}(p) \int \mathrm{d}x\, |x\rangle\langle x|p\rangle \\ &= \sum_n \alpha_n|a_n\rangle \int \mathrm{d}p\, \mathrm{d}x \exp[ip(x - \epsilon a_n)]\, \tilde{\phi}(p)|x\rangle, \end{aligned} \tag{1.7}$$

which by virtue of an inverse Fourier transform reduces to

$$U(\epsilon)|\psi_S\rangle|\eta_P\rangle = \sum_n \alpha_n|a_n\rangle \int \mathrm{d}x\, \phi(x - \epsilon a_n)|x\rangle = \sum_n \alpha_n|a_n\rangle|\Phi(\epsilon a_n)\rangle. \tag{1.8}$$

Thus, the system-pointer state evolves to a superposition of eigenstates of A_S coupled to Gaussian wave packets with spread σ and central value $x = \epsilon a_n$. A measurement of A_S is done by reading off the pointer's position X_P. We define *strong measurements* as those for which $\epsilon(a_{n+1} - a_n) \gg \sigma$, i.e., those where the pointer wave packets are distributed without overlapping, so that X_P is found to be unambiguously correlated to the measured eigenvalue of A_S. This situation is illustrated in figure 1.1. Conversely, *weak measurements* are those characterized by $\epsilon(a_{n+1} - a_n) \not\gg \sigma$, meaning that the Gaussians in equation 1.8 do overlap, which in turn implies that the pointer's position has no clear correlation with any single eigenvalue a_n, as shown in figure 1.2.

---

8. We can interpret Δt as the time interval during which the measurement apparatus interacts with the system. While the interaction takes place, all other terms in the total Hamiltonian that describes the joint system can be safely neglected in favor of H_{int}. In our previous example, $\epsilon = \alpha/2 \equiv -\mu B_z \Delta t$, with Δt being the neutron's transit time in the magnetic field region and α the spin rotation angle.
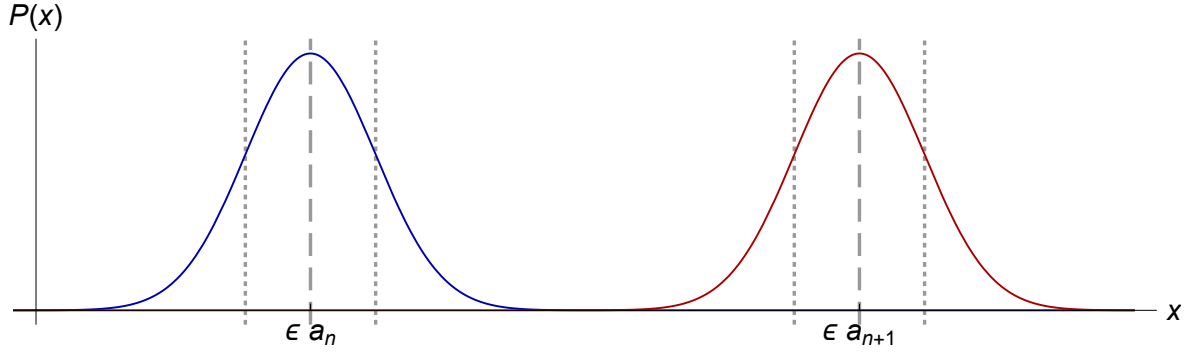
Figure 1.1: Non-overlapping Gaussian wave packets of a pointer entangled with a system in a strong interaction, for which $\epsilon(a_{n+1} - a_n) \gg \sigma$. A reading of the pointer's position x is uniquely correlated to a single eigenvalue of the system operator A_S. Vertical lines indicate the Gaussians' spread σ and central value.
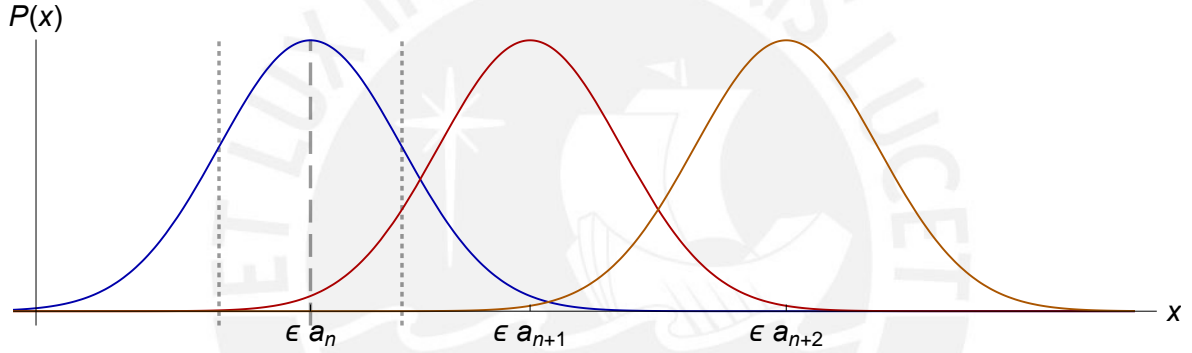
Figure 1.2: Overlapping Gaussian wave packets of a pointer entangled with a system in a weak interaction, for which $\epsilon(a_{n+1} - a_n) \not\gg \sigma$. A reading of the pointer's position x is not uniquely correlated to any eigenvalue of the system operator A_S. Vertical lines indicate the leftmost Gaussian's spread σ (shared by the others) and central value.

In the latter case, the interaction disturbs the state slightly and a subsequent strong measurement, known as *postselection*, can be done on S. Since postselection is achieved by projecting the system state onto a vector $|\xi_S\rangle$, the (unnormalized) final pointer state will be

$$|\zeta_P\rangle = \langle \xi_S | U(\epsilon) | \psi_S \rangle | \eta_P \rangle. \tag{1.9}$$

Weak values enter the picture when we expand $\langle \xi_S | U(\epsilon) | \psi_S \rangle$ as a series in the pointer-space operator:

$$\langle \xi_S | U(\epsilon) | \psi_S \rangle = \left\langle \xi_S \left| \mathbb{1}_{SP} - i\epsilon A_S B_P + \frac{(-i\epsilon)^2}{2} A_S^2 B_P^2 + \dots \right| \psi_S \right\rangle$$

$$= \left(\langle \xi_S | \psi_S \rangle \mathbb{1}_P - i\epsilon \langle \xi_S | A_S | \psi_S \rangle B_P + \frac{(-i\epsilon)^2}{2} \langle \xi_S | A_S^2 | \psi_S \rangle B_P^2 + \dots \right)$$

$$= \langle \xi_S | \psi_S \rangle \left(\mathbb{1}_P - i\epsilon \frac{\langle \xi_S | A_S | \psi_S \rangle}{\langle \xi_S | \psi_S \rangle} B_P + \frac{(-i\epsilon)^2}{2} \frac{\langle \xi_S | A_S^2 | \psi_S \rangle}{\langle \xi_S | \psi_S \rangle} B_P^2 + \dots \right). \quad (1.10)$$

By defining the weak value of A_S for the *preselection* state $|\psi_S\rangle$ and the postselection state $|\xi_S\rangle$ as the complex number

$$\langle A_S \rangle_w \equiv \frac{\langle \xi_S | A_S | \psi_S \rangle}{\langle \xi_S | \psi_S \rangle}, \quad (1.11)$$

and more generally the nth-order weak value of A_S as

$$\langle A_S^n \rangle_w \equiv \frac{\langle \xi_S | A_S^n | \psi_S \rangle}{\langle \xi_S | \psi_S \rangle}, \quad (1.12)$$

equation 1.10 becomes

$$\langle \xi_S | U(\epsilon) | \psi_S \rangle = \langle \xi_S | \psi_S \rangle \left(\mathbb{1}_P - i\epsilon \langle A_S \rangle_w B_P + \frac{(-i\epsilon)^2}{2} \langle A_S^2 \rangle_w B_P^2 + \dots \right). \quad (1.13)$$

We can see how weak values appear in the physical state of the pointer with the following series of approximations. If we apply equation 1.13 to the Gaussian pointer in equation 1.4 in order to compute equation 1.9, we get

$$|\zeta_P\rangle = \langle \xi_S | \psi_S \rangle \left(\mathbb{1}_P - i\epsilon \langle A_S \rangle_w B_P + \frac{(-i\epsilon)^2}{2} \langle A_S^2 \rangle_w B_P^2 + \dots \right) \int \mathrm{d}p \, \tilde{\phi}(p) |p\rangle$$

$$= \langle \xi_S | \psi_S \rangle \int \mathrm{d}p \left(1 - i\epsilon \langle A_S \rangle_w p + \frac{(-i\epsilon)^2}{2} \langle A_S^2 \rangle_w p^2 + \dots \right) \tilde{\phi}(p) |p\rangle. \quad (1.14)$$

In the spirit of Duck *et al.* [78], we approximate the sum in parentheses as an exponential of the complex number in the first-order term by considering that 1) the magnitude of the zeroth-order term is much larger than the magnitudes of every other term, and 2) the magnitude of the first-order term is much larger than the magnitudes of every higher order term, i.e.,

$$1 \gg \left| \frac{(-i\epsilon)^n}{n!} \frac{\langle \xi_S | A_S^n | \psi_S \rangle}{\langle \xi_S | \psi_S \rangle} p^n \right|, \quad \forall n \geq 1, \quad (1.15a)$$

$$\left| -i\epsilon \frac{\langle \xi_S | A_S | \psi_S \rangle}{\langle \xi_S | \psi_S \rangle} p \right| \gg \left| \frac{(-i\epsilon)^n}{n!} \frac{\langle \xi_S | A_S^n | \psi_S \rangle}{\langle \xi_S | \psi_S \rangle} p^n \right|, \quad \forall n \geq 2. \quad (1.15b)$$

Clearly, the previous expressions contain a degree of redundancy: if equation 1.15a is valid for $n = 1$, and equation 1.15b holds, then equation 1.15a also holds for $n \geq 2$. After simplifying the expressions that remain, we are left with

$$1 \gg \epsilon |p \langle A_S \rangle_w|, \quad (1.16a)$$

11

$$|\langle \xi_S|A_S|\psi_S\rangle| \gg \frac{\epsilon^{n-1}}{n!} \left| p^{n-1}\langle \xi_S|A_S^n|\psi_S\rangle \right|, \quad \forall n \geq 2. \tag{1.16b}$$

To eliminate the redundancy lingering in equation 1.16b we rewrite it as

$$\left(n! \frac{|\langle \xi_S|A_S|\psi_S\rangle|}{|\langle \xi_S|A_S^n|\psi_S\rangle|} \right)^{1/(n-1)} \gg \epsilon\,|p|\,, \quad \forall n \geq 2, \tag{1.17}$$

and notice that, if this inequality is satisfied for the minimum value of the left-hand side, then it holds for all $n \geq 2$. Moreover, although the integration variable p ranges from $-\infty$ to ∞, the integral in equation 1.14 results mostly from contributions centered around $p = 0$ with spread $1/\sigma$ because $\tilde{\phi}(p)$ is a Gaussian function. We can thus substitute $1/\sigma$, a quantity representative of the relevant values of p, into equations 1.16a and 1.17, and thereby attain the weakness conditions

$$\frac{1}{|\langle A_S\rangle_w|} \gg \frac{\epsilon}{\sigma}, \tag{1.18a}$$

$$\min_{n=2,3,\dots} \left(n! \frac{|\langle \xi_S|A_S|\psi_S\rangle|}{|\langle \xi_S|A_S^n|\psi_S\rangle|} \right)^{1/(n-1)} \gg \frac{\epsilon}{\sigma}, \tag{1.18b}$$

under which equation 1.14 now takes the form[9]

$$|\zeta_P\rangle \approx \langle \xi_S|\psi_S\rangle \int \mathrm{d}p \exp(-i\epsilon\langle A_S\rangle_w p)\,\tilde{\phi}(p)|p\rangle. \tag{1.19}$$

Finally, we proceed as we did in equations 1.7 and 1.8 to obtain

$$
\begin{aligned}
|\zeta_P\rangle &\approx \langle \xi_S|\psi_S\rangle \int \mathrm{d}p \exp(-i\epsilon\langle A_S\rangle_w p)\,\tilde{\phi}(p) \int \mathrm{d}x\,|x\rangle\langle x|p\rangle \\
&= \langle \xi_S|\psi_S\rangle \int \mathrm{d}x\,\mathrm{d}p \exp(-i\epsilon\langle A_S\rangle_w p)\exp(ipx)\tilde{\phi}(p)|x\rangle \\
&= \langle \xi_S|\psi_S\rangle \int \mathrm{d}x\,\phi(x-\epsilon\langle A_S\rangle_w)|x\rangle \\
&= \langle \xi_S|\psi_S\rangle \int \mathrm{d}x\,\frac{1}{(2\pi\sigma^2)^{1/4}} \exp\left(-\frac{(x-\epsilon\langle A_S\rangle_w)^2}{2\sigma^2}\right)|x\rangle \\
&= \langle \xi_S|\psi_S\rangle|\Phi(\epsilon\langle A_S\rangle_w)\rangle. \tag{1.20}
\end{aligned}
$$

A weak value of A_S is a complex number whose real and imaginary parts can take values much greater than any eigenvalue of A_S, depending on how little the pre- and postselection states overlap.[10] For this reason, its emergence as the central value of the

---

9. See Appendix A of [79] for complementary observations about the validity of equation 1.19.

10. Weak values $\langle A_S\rangle_w$ that exceed the range of eigenvalues of A_S are said to be *strange* [80, 81] or *nonclassical* [81, 82].

wave packet that describes the final pointer state might seem unfathomable, but it must be understood in the light of equation 1.18a.

Much removed from its origins as a mathematical curiosity that sprouted from a philosophical discussion about the arrow of time [83] are the manifold appearances the weak value has made in experimental endeavors. In 1991, Ritchie *et al.*'s experiment [40], carried out with laser light, demonstrated the first measurement of weak values. Over the next decade, weak values were realized only in classical or semiclassical settings–meaning that they could "be explained semiclassically using a wave equation derived from Maxwell's equations"–until Pryde *et al.*'s single-photon experiments achieved "the first unambiguously quantum-mechanical" realization [84]. Already in 1989, Duck *et al.* [78] foresaw the possibility of weak values having "applications to the detection of very tiny signals."[11] Notable examples of parameter amplification via weak values include the measurement of angles of only a few hundred femtoradians and displacements of a few tens of femtometers [85], as well as the measurement of displacements of about 1 angstrom, which confirmed the existence of the photonic version of the spin Hall effect [86].

A parallel line of inquiry deals with the use of weak values to measure complex-valued quantities, whereof the probability amplitudes of pure states and the density matrix elements of mixed states stand out. This particular usage insinuates a connection to quantum state tomography. As we saw in section 1.2, tomography requires a series of measurements, whose outcomes must be then postprocessed. Let us distinguish between two types of postprocessing: one has to do with converting data into the state parameters, which is typically done via inversion algorithms;[12] the other refers to imposing physicality on the reconstructed state, a task wherefore estimation routines are usually employed. All methods that demand inversion postprocessing can be suitably called *indirect*. In contrast, techniques that yield as outcomes the real and imaginary parts of either the amplitudes of a state vector or the entries of a density matrix are said to be *direct*. In 2011, Lundeen *et al.* [87] put forward and successfully tested the first *direct state measurement* protocol. It exploits the proportionality between the com-

---

11. See section IV.A of [28] and references therein for a pedagogical primer on this topic.

12. See, e.g., equation (3.20) of [68], or, in the present thesis, equations 2.11–2.15 of section 2.1.2, and equations 2.20–2.21 of section 2.2.1.

plex amplitudes of a pure state and appropriate weak values, which, to first order in the coupling strength, are read off straight by measuring a pointer observable. Later, Lundeen and Bamber [88] presented two generalizations, valid for mixed states, whose first realizations were reported in laser light experiments [42, 43]. Let us note for future reference that the alluded schemes involve a weak measurement followed by postselection (a strong measurement). In neither [87] nor [88] was the posibility entertained of abandoning weak measurements.

But Lundeen *et al.*'s original technique [87] suffers from a flaw which precludes it from being a tomography protocol: it is not universal. As Haapasalo *et al.* [89] argued, due to its origin as an approximation to first order in the system-pointer coupling, the procedure fails at reconstructing states that have a small overlap with the postselection state.[13] This finding begs two questions: 1) How weak must measurements be in order for weak values to be obtainable from them? 2) Would eschewing the weakness hypothesis in Lundeen *et al.*'s scheme produce a proper tomography protocol? As early as 2007, Johansen [82] had found that the answer to the first question was, squarely, not at all. He derived a model for determining the real and imaginary parts of a weak value exclusively through projective measurements. Forays beyond the weak regime looked promising.

The positive answer to the second question manifests in at least two distinct forms. In a system-pointer measurement setting, Zhang *et al.* [91] defined special pointer operators as functions of the interaction strength. They showed that, by measuring joint expectation values of these "coupling-deformed" observables, information about weak values can be extracted through measurements of arbitrary strength. A follow-up publication by Zhu *et al.* [92] formulated a quantum state tomography scheme based on measurements of said coupling-deformed observables. An altogether independent path was followed by Calderaro *et al.* [56], who considered a setup in which a system is coupled to two pointers. These authors proposed and demonstrated in single-photon experiments two proper tomography techniques that involve subsequent measurements of arbitrary coupling, each one with a different pointer. The proposals by both groups [56, 91, 92] constitute actual state tomography protocols.

---

13. Credit goes to Dressel *et al.* [28] as well as Maccone and Rusconi [90] for this interpretation of Haapasalo *et al.*'s equations (14)–(16) [89].

Besides enabling universality, what other merits are there for strong system-pointer interactions in state measurement schemes? We can point out two. As for the first, Maccone and Rusconi [90] had found that Lundeen *et al.*'s protocols [87, 88] present an inherent bias: the states they reconstruct have an unavoidable degree of discrepancy with respect to their corresponding target states, regardless of how many copies are averaged over. Both [91] and [92] provide evidence that Zhu *et al.*'s tomography technique [91, 92] eliminates said bias. In addition, a state measurement scheme advanced by Zou *et al.* [93] which uses a strong coupling also exhibits no such bias, in spite of its being non-universal. The disappearance of the original proposals' bias correlates to the renouncing of the weakness hypothesis.

The second benefit, not entirely unrelated to the first, pertains to two aspects of the results yielded by all measurement procedures: *accuracy* and *precision*. Despite their apparent synonymy, these terms have exact, distinct meanings in the research that we will presently review. Accuracy shall refer to the degree to which an experimental result differs from its theoretical counterpart. This trait can be assessed by any quantifier of *systematic errors*. Precision, on the other hand, will be a measure of how much a particular outcome fluctuates. So defined, it represents the *statistical uncertainty* in the results.[14] A lower precision (accuracy) is marked by larger statistical uncertainties (systematic errors), and viceversa.

Starting in 2014, a series of results bolstered the thesis that state reconstruction protocols can be made more accurate and precise when employed with strong rather than weak system-pointer couplings. Das and Arvind [95] propounded a qubit characterization scheme consisting of two consecutive measurements of variable strength (albeit not too strong) followed by a projective measurement. Their numerical simulations showed that, as the system-pointer interaction increases, the mean fidelity between reconstructed and reference states (which serves as a measure of systematic errors) reaches a maximum, and said fidelity's standard deviation (which quantifies its statistical uncertainty) bottoms out. Vallone and Dequal [94] generalized Lundeen *et al.*'s original proposal [87] to account for arbitrary measurement strengths. By using the so-called mean square statistical error, they contrasted the precision of their scheme

---

14. Also customarily called statistical error, as in [56] and [94].

at its "highest" coupling value[15] to that of the weak scheme. The fluctuations of the former were much smaller than those of the latter. As reported by Gross *et al.* [96], furthermore, the fidelity of the outcomes produced by Vallone and Dequal's procedure, i.e., their accuracy, can be maximized at specific strong couplings. Later, Calderaro *et al.* [56] analyzed the precision of their direct state tomography protocol in the same manner as in [94], and its accuracy via the trace distance between reconstructed and target states.[16] Their figures of merit strongly suggest that, the stronger the measurements are, the more accurate and precise will the reconstruction be. Xu *et al.* [57] applied the principle of system-pointer measurements to the context of quantum detector tomography, in which the unknowns are the operators comprising a tomography apparatus. These authors quantified systematic errors via the trace distance and statistical uncertainty with the variance of the measured operators. Based on their experimental results in single-photon experiments, they asserted that strong measurements allowed them "to improve the precision of the tomography without loss of accuracy."

The aforementioned thesis, however, must be appended with a caveat on the following accounts. The fidelity and standard deviation in Das and Arvind's measurement scheme [95] are not monotonous functions of the interaction strength: as it grows, both metrics reach an extremum, but then continue to either decrease or increase, respectively. In Gross *et al.*'s analysis [96], the fidelity exhibits the same behavior. For their part, Zhu *et al.* [92] chose the trace distance and the variance to assess systematic errors and statistical uncertainties, respectively. Through error propagation theory and numerical simulations, they showed that both quantities depend identically on the coupling parameter, and are thus minimized when it takes a certain value. In all, these findings paint a clear-cut picture: stronger measurements can optimize precision and accuracy, but must not be regarded as synonymous with them.

The preceding historical excursus notwithstanding, it is a series of works on matter-

---

15. In chapter 3 we shall have more to say about the range of values that the strength parameter can take.

16. The trace distance $\mathcal{D}$ between two density operators ρ_1 and ρ_2 is defined as $\mathcal{D}(\rho_1, \rho_2) \equiv \frac{1}{2}\mathrm{Tr}\,|\rho_1 - \rho_2|$, with the absolute value of an operator O given by $|O| \equiv \sqrt{O^\dagger O}$, the positive square root of $O^\dagger O$. If the two density operators represent pure states, their trace distance and fidelity are interchangeable: $\mathcal{D}(|\psi_1\rangle\langle\psi_1|, |\psi_2\rangle\langle\psi_2|) = \sqrt{1 - \mathcal{F}^2(|\psi_1\rangle\langle\psi_1|, |\psi_2\rangle\langle\psi_2|)} = \sqrt{1 - |\langle\psi_1|\psi_2\rangle|^2}$ (see sections 9.2.1 and 9.2.3 of [72] for more details).

wave interferometry what sets the scene for the contributions reported in this dissertation. Using weak measurements, Sponar *et al.* [77] ascertained the weak values of a neutron's Pauli spin operator. As Pryde *et al.* had done before [84], these authors touted the exclusively quantum-mechanical nature of their results by stressing that "no classical theory can describe these weak measurement results in contrast to the case of photon experiments." In two subsequent works [45, 46], the same group developed a model for characterizing $\langle \sigma_z^p \rangle_w$, the weak value of a spin operator of the path degree of freedom, with arbitrarily strong system-pointer couplings. Knowledge of this weak value enables reconstruction of the preselection path state. The authors then put their model to test in the same interferometric setup as [77] for two different couplings—one weak and one strong. Denkmayr *et al.* presented the parameters of the preselection state in [45] and the weak values in [46]. Both publications showed good agreement between theory and experiment for both strengths, and claimed, arguably without sufficient reserve, that stronger measurements produce lower statistical and systematic errors than weaker ones. Indeed, Denkmayr *et al.* concluded that "experimental evidence is given that strong interactions are superior [...] in terms of accuracy and precision, as well as required measurement time" and that their model "can be used for any coupling between two two-level quantum systems" [45, 46].

My coworkers and I took them up on their suggestion. In section 3.1 of this thesis I derive an extended version of Denkmayr *et al.*'s model, which measures weak values of arbitrary Pauli spin operators $\sigma_\mathbf{n} = \mathbf{n} \cdot \boldsymbol{\sigma}$, with $\mathbf{n}$ a real unit vector. As I show in sections 3.2.1 and 3.2.2, this protocol can be implemented in both an all-optical setting and a quantum computational context. Section 3.2.2 also describes a state characterization technique based on the same measurements that yield the referred weak values. We tested these schemes across a wider range of couplings than [45, 46] by using quantum computers, which allow for much more versatile realizations than neutron interferometry, and even than optical interferometry. Our results, recounted in section 3.3, are consistent with Denkmayr *et al.*'s, but also confirm two features of the model that had been overlooked: it breaks down for certain strengths, and it cannot be accepted as an actual instance of strong measurements being always more accurate and precise than weak ones.

1.4 Quantum Computing

Quantum computing is, broadly speaking, the realization of computational tasks that harnesses the resources of quantum systems. Its origins date back to Benioff's 1980 quantum mechanical model of computers [97], which described the operation of Turing machines with the Schrödinger equation. Shortly thereafter, Manin [98] and Feynman [99] put forward proposals for the use of quantum systems for computation, while Benioff continued to develop a framework for quantum Turing machines [100, 101]. The seeds for the flourishing of quantum computing were thus planted, and discoveries in quantum information theory provided proper nourishment. Results such as the no-cloning theorem [102] and the quantum noiseless-channel coding theorem [103], as well as protocols like cryptographic key distribution [104], error correction [105], and entanglement distillation [106] would, in time, become key components of the discipline. The decade of 1990 was showered by quantum computation algorithms whose names are nowadays synonymous with the virtues of quantum over classical computing. Among these number the Deutsch-Josza [107] and Simon [108] algorithms for the eponymous problems, as well as the landmark algorithms by Shor for large integer factorization [10] and Grover for database search [11, 109].

Mathematically, effecting a quantum computation merely requires that we write a state, apply some unitary operators on it, compute the resulting state, and measure some projector or observable. Physically, these tasks are immensely more difficult, for they must be realized in devices (computers) capable of operating in a controlled manner. In 2000, DiVincenzo [110] highlighted seven criteria for the physical realization of quantum information processing tasks and protocols: five for quantum computation on its own, and two more for quantum communication. Known commonly as the DiVincenzo criteria, these conditions are "deceptively simple", which "made them the guiding principles for researchers trying to build quantum computers over the past two decades" [111]. To introduce the central concepts that will underlie the work presented in chapter 3, let us name and briefly survey the first five requirements:[17]

1. *A scalable physical system with well characterized qubits.* Two-level quantum systems

---

17. The latter two requirements, while essential for quantum key distribution, quantum teleportation, *inter alia,* are beyond the scope of the present thesis.

are the basic building blocks of quantum computers. They exist in a myriad of physical systems where one quantity can take two values: horizontal and vertical polarization of light, spin up or down of a particle, ground and first excited state of an atom, as well as the vacuum and single photon state of an electromagnetic field, to mention the most elementary examples. Some "effective" qubits consist of two states within which a transition is allowed, even though the system admits other blocked states [112]. We say that qubits are well characterized if we know with precision the couplings between the states of interest and the rest, and if we can minimize and control the rate of unwanted transitions. To construct devices that bring about the promises of quantum computation, a capacity for scaling the number of qubits becomes imperative.

2. *The ability to initialize the state of the qubits to a simple fiducial state.* The first step of any quantum computation demands that the initial state of the system under consideration be readily accessible and known with as much certainty as possible. This reference, or fiducial, state typically takes the form of the tensor product of the ground states of each qubit. In practice, ground state initialization can be a complicated endeavor.[18]

3. *Long relevant decoherence times.* The phenomenon whereby a system that interacts with its environment (i.e., any real-world physical system) experiences an irreversible transformation from a coherent state, say, $a|0\rangle + b|1\rangle$, to an incoherent mixed state, e.g., $|a|^2 |0\rangle\langle0| + |b|^2 |1\rangle\langle1|$, is called *decoherence* [113]. It addresses the question of why some quantum states are extremely fragile and sensitive to environmental couplings. For any quantum computation to be of use, qubits must, on average, be operated and measured before they undergo decoherence, otherwise the outcome turns into meaningless noise. A simple framework for understanding this phenomenon is the Bloch-Redfield model of decoherence, wherein the longitudinal and transverse relaxation times T_1 and T_2 characterize the time scales in which qubit decoherence occurs, and thus represent the time scales of relevance.[19]

---

18. See, e.g., [110], p. 774, and references therein for details on how setting a qubit to a standard state hinges on the nature of both the task at hand and the particular type of quantum computer it is implemented in.

19. See section III B 2 of [114] for an introductory account of the model.

4. *A "universal" set of quantum gates.* Within the field of quantum computing, unitary operators are called *quantum gates*. DiVincenzo [115] proved that two-qubit gates are *universal* for quantum computation, viz. that they suffice for constructing a general quantum circuit of any number of qubits. The physical realization of quantum gates entails the design and operation of a wealth of dynamical processes between elements of the computer.[20] Quantum computers must be capable of implementing arbitrary operations on their qubits, for which a small number of one- and two-qubit gates, a non-unique *universal set,* is necessary. Quantum gates, unfortunately, do not operate with 100% certainty; instead, they are characterized by an *error rate*.

5. *A qubit-specific measurement capability.* The last step of a computation is the measurement stage. In order to realize it, quantum computers must be equipped with appropriate measurement instruments. Ideally, a measurement would return the outcome 0 with probability p, and 1 with probability $1 - p$. But present-day quantum computers are imperfect, which is reflected in, among other things, their qubit *readout error rates* [116].[21]

Regardless of the daunting difficulties involved in physical quantum computations, the 1990s saw progress in the experimental lane spurred on by Monroe *et al.*'s [117] demonstration of a two-qubit quantum gate (the so-called controlled NOT gate, part of a universal gate set), with the two qubits codified in the internal and external degrees of freedom of cold, trapped ions. In 1998, Jones and Mosca [118] as well as Chuang *et al.* [63] experimentally demonstrated a quantum algorithm for the first time: both groups successfully carried out Grover's search algorithm in two-qubit nuclear magnetic resonance quantum computers. That same year, Linden *et al.* [119] implemented the Deutsch-Josza algorithm for the first time in a three-qubit computer of the same kind; it would take until the year 2000 for that number of qubits to rise up to five [120]. In the meantime, Nakamura *et al.* [121] would show how to use a superconducting circuit to perform quantum computations. A short digression on superconductivity is in order before discussing the quantum computers that occupy us.

---

20. See, e.g., section IV of [114] for details on quantum gate implementation in superconducting quantum computers.

21. See section V of [114] for details on several readout methods for superconducting qubits.

Superconductivity is the quantum mechanical phenomenon wherein certain substances have virtually zero electrical resistance at extremely low absolute temperatures. The Nobel Prize-winning Bardeen-Cooper-Schrieffer theory of low-temperature superconductivity condenses a successful description of superconductor properties. Among them we find the existence of net attractive forces between electrons in an ion lattice, which result in bound pairs of electrons called *Cooper pairs*. Because their effective spin has integer values (either 0 or 1), all Cooper pairs in the material are described by a single wave function. Thus, the study of macroscopic quantum effects becomes possible in superconducting materials [122]. Macroscopic qubits are constructed, for instance, by connecting an electrode to a reservoir (both superconductors) through a thin insulator (a *Josephson junction*), as in the case of *charge qubits* [123, 124]. Cooper pairs experience tunneling through the junction, which can be conveniently tuned so that only transitions among the two lowest-energy states (the macroscopic ground state, $|0\rangle$, and the state with one additional Cooper pair, $|1\rangle$) take place, thereby achieving a macroscopic qubit [121]. Besides charge qubits, many other superconducting qubit archetypes exist, such as flux qubits, phase qubits, as well as hybridizations of the first three types: C-shunt flux qubits, 0-π qubits, and, most relevant for our purposes, transmon-type qubits, to name just a few.[22]

After the invention of transmon superconducting qubits in 2007 [126], the International Business Machines Corporation undertook the design of transmon qubit-based quantum processors. In order to attain good computational results, these qubits must remain in a given state for a suitable amount of time before the onset of decoherence. By 2012, IBM's transmon qubits had achieved this goal [127]. At the time of this writing, the qubits employed by IBM users are "made from superconducting materials such as niobium and aluminum, patterned on a silicon substrate." They consist of two energy levels separated by a characteristic frequency around 5 GHz; are protected from stray electromagnetic fields via shielding; and are kept inside so-called dilution refrigerators at 15 mK in order to "minimize ambient noise or heat that could excite the superconducting qubit and increase the error probability." [128].

Research done over the past decade and a half culminated in the milestone 2016

---

22. See [125] for a recent review of progress in superconducting quantum computing and for more details on the different archetypes.

release of IBM Quantum Experience, a cloud-based platform that gave users free access to a five-qubit superconducting quantum processor (or system, in the parlance of IBM). Since its unveiling, IBM Quantum Experience has undergone significant changes. Most manifest among these are its unfolding into IBM Quantum Composer and IBM Quantum Lab, as well as the addition of new systems, some of which contain 7 qubits.[23] Researchers seized these new tools rapidly and have since carried out with them various experimental proposals: violations of Mermin inequalities (generalized Bell inequalities) [129]; realizations of "quantum error correction, quantum arithmetic, quantum graph theory, and fault-tolerant quantum computation" [130]; mitigation of decoherence via dynamical decoupling [131]; automated error correction and nondestructive state discrimination [132]; detector characterization [133]; entanglement purification and swapping [134]; and verification of the Jakob-Bergou relations between visibility, distinguishability, and entanglement [135], to name just a few examples. In some cases, researchers arrived at interesting conclusions and recommendations for hardware revision [133]. Clearly, increased access to quantum processors has fostered a rich feedback loop between end users and providers that can give rise to further advances in quantum technologies.

But perhaps the most significant changes in IBM's quantum computing platform were the introduction of new functionalities and coding environments–such as the Python-based software development kit Qiskit [136]–as well as its integration with Jupyter notebooks, an interactive web browser-based platform where notebook documents can be edited and executed. After completing a few registration formalities, users can control IBM's quantum systems remotely via simple Python scripts. By virtue of this enhanced ease of use and of the fact that these tools allow for experimental settings to be varied effortlessly, quantum processors represent a much more versatile alternative to traditional laboratory contexts, such as neutron or optical interferometry.

The mention of such contexts, as well as the unreservedness of my stated intention to experiment with IBM's quantum processors instead of them could, understandably, give readers pause. After all, why should anyone expect currently-existing quantum

---

23. At the time of this writing, four 7-qubit and four 5-qubit processors are available for free users, as well as up to 433-qubit processors for paid users (see online). It must be stressed, though, that IBM can, at any point in time, retire its processors from service and also bring in new ones into its catalog (see below).

devices to produce outcomes comparable to those obtained in well-established experimental paradigms? Addressing such a non-trivial question is beyond the scope of this work. In lieu of a complete answer, I now lay out an argument by analogy for the use of present-day transmon-based quantum computers as a testing ground for the particular kind of study reported in chapter 3. All-optical setups that consist of interferometers and polarization-altering instruments frequently regard the propagation path and polarization of either laser light or individual photons as two qubits of interest. Within these arrangements, we can prepare target states, implement operations, and carry out measurements. As light traverses the device, it encounters beam splitters, mirrors, phase shifters, birefringent wave plates, polarizing filters, etc. At each stage, a degree of uncertainty is added to the polarization qubit's state and, by extension, the overall two-qubit state: every instrument reflects and absorbs a (not always minuscule) fraction of incident light, can be operated with limited accuracy, and is subject to the experimentalist's correct handling. Moreover, the lengths of the interferometer's arms experience uncontrolled variations uninterruptedly due to ambient mechanical perturbations. As a consequence of all the referred factors, the setup's output resembles the target output to a limited extent.

On the other hand, the quality of the results of experiments performed in IBM's quantum systems depends, on average, on 1) how much longer the qubits' decoherence times T_1 and T_2 are than the total circuit operation time, and 2) the cumulative effect of the error rates of each step in the computation. As per DiVincenzo's second criterion, all qubits are initialized in the ground state $|0\rangle$ before running a circuit. A specific sequence of quantum gates is then applied which, ideally, produces the desired outcome. However, one-qubit (two-qubit) gates have error rates between 0.02% and 0.06% (0.6% and 1%),[24] and take a few tens (hundreds) of nanoseconds to be carried out. Additionally, measurement results are read with readout error rates ranging from 1% to 14%, a process which lasts about one thousand nanoseconds. These individual durations must be contrasted to T_1 and T_2, which vary from a few tens up to a few hundreds of microseconds. As in

_____

24. The parameters reported here and elsewhere in this thesis correspond, for concreteness and with no loss of generality, to ibm_oslo, the system used for our calculations (see below). Before it was retired from service in early May, 2023, most of its parameters were available in the IBM Compute resources website. To the best of my knowledge, documentation for ibm_oslo is not found in the public domain anymore.

the optical case, we obtain an outcome that differs from the expected result depending on a series of factors. Both contexts, therefore, allow us to realize the proposal outlined at the end of section 1.3 with comparable degrees of precision and accuracy. Since, as argued before, quantum computers are more versatile, we employed them to realize the experiments described in chapter 3.

IBM provides access to *backends*: either simulators or real quantum devices that do quantum computations. At the time our work took place, IBM's open services portfolio consisted of six backends. Our computations were carried out in the ibm_oslo backend – a seven-qubit system of processor type Falcon r5.11H[25] with the H-shaped qubit connectivity graph shown in figure 1.3. This diagram illustrates how the actual superconducting qubits are connected in the physical quantum processor: qubit 0 is coupled only to qubit 1, which in turn is linked to qubits $0, 2$, and 3, and so forth. Qubit connections are relevant when considering what quantum gates to act on qubit pairs. For the experiments presented in section 3.3, only two qubits were required, for which qubits 0 and 1 were chosen. We selected ibm_oslo for our calculations in a trade-off between its workload and its average decoherence times in comparison to the other backends. For qubit 0, T_1 and T_2 averaged $142\,\mu$s and $101\,\mu$s, respectively, whereas for qubit 1 they averaged $135\,\mu$s and $26\,\mu$s during data recollection.

In accordance to DiVincenzo's fourth criterion, each quantum system is characterized by a universal set of basis gates that can operate on either individual qubits or pairs of qubits. In particular, ibm_oslo could realize the following operations: the X gate, a Pauli σ_x operator; SX, the square root of σ_x, which in the basis of σ_z is represented as

$$SX = \frac{1}{2}\begin{pmatrix} 1+i & 1-i \\ 1-i & 1+i \end{pmatrix};$$

(1.21)

$RZ(\alpha)$, a rotation of the form $\exp(-i\alpha\sigma_z/2)$; the identity gate ID; as well as the two-qubit controlled X gate, $\mathrm{C}X$, which can be applied on the connected pairs of qubits in figure 1.3 and has the representation

$$\mathrm{C}X = \begin{pmatrix} 1 & 0 & 0 & 0 \\ 0 & 1 & 0 & 0 \\ 0 & 0 & 0 & 1 \\ 0 & 0 & 1 & 0 \end{pmatrix}.$$

(1.22)

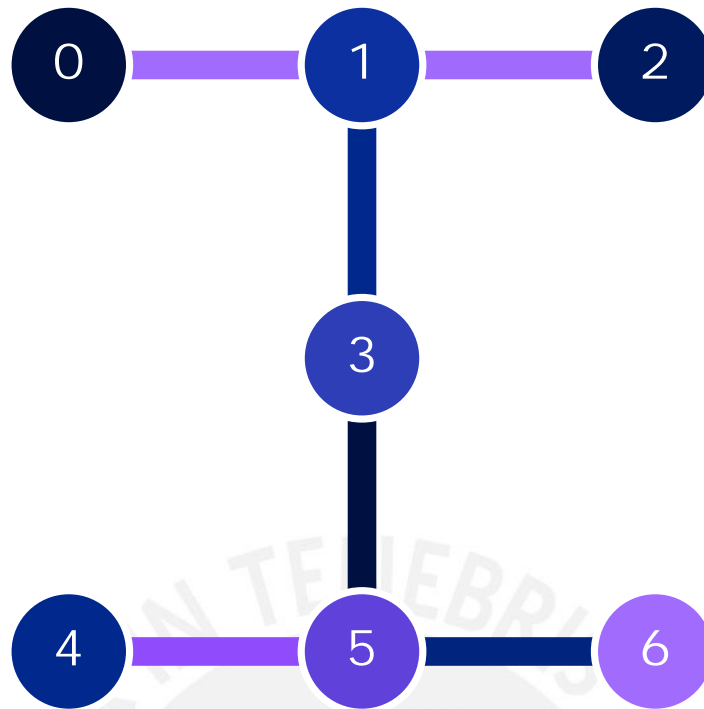25. See the IBM Quantum processor types website for details.

Figure 1.3: Qubit connectivity graph for the ibm_oslo backend. Credit: IBM Quantum.

Whenever a different operation, either not listed in the foregoing or not existing for an unconnected pair of qubits, is demanded of the backend, a *transpilation* process rewrites it in terms of the physically available gates. If the transpiler returns gate sequences longer than those present in the original circuit, the total run time increases, as does the decoherence probability commensurately. The results of a circuit run are obtained through measurements of the Pauli operator $\sigma_z = |0\rangle\langle 0| - |1\rangle\langle 1|$ on each qubit (DiVincenzo's fifth criterion). Each measurement is stored as a count of either the $|0\rangle$ state or the $|1\rangle$ state.

To close this chapter, let us introduce a critical parameter of interest for quantum computations: the *number of shots*, defined as the number of times a circuit is executed on a quantum system. This parameter "determines the precision of the output probability distribution over repeated executions". Each shot is a realization of the circuit. The ibm_oslo backend admitted experimental runs with up to $20\,000$ shots. Each run with a given number of shots is called an *experiment*. Free users of IBM's quantum systems can queue a maximum of 100 experiments at a time. A collection of experiments comprises a *job*. Naturally, the computation time grows with the number of shots, so the total number of shots in a job can represent a bottleneck for the realization of several exper-

iments in series. It is desirable, hence, to assess the minimal number of shots needed to obtain an intended precision in the output probability distribution. To make an educated estimation thereof, we turned to inferential statistics.[26] Let ζ be the outcome of each measurement, which is a random variable following a Bernoulli distribution because it answers a yes-no question. For p the (unknown) probability of measuring $|1\rangle$ and $1-p$ the probability of $|0\rangle$, the expected value of ζ is p and its standard deviation $\sqrt{p(1-p)}$. Given a large number of samples (i.e., shots), n, the sample mean follows a normal distribution with mean p and standard deviation $\sqrt{p(1-p)/n}$. A *confidence interval* for the mean of ζ at a level of confidence c is a range of values wherein p lies with probability c, and reads

$$\left[\hat{p} - z_{\frac{1-c}{2}}\sqrt{\frac{p(1-p)}{n}}, \hat{p} + z_{\frac{1-c}{2}}\sqrt{\frac{p(1-p)}{n}}\right]. \tag{1.23}$$

In the above equation, $\hat{p}$ stands for an estimator for the mean of ζ, whereas $z_{\frac{1-c}{2}}$ denotes the *critical value at confidence level* c for a confidence interval of $N(0,1)$, the normal distribution with mean 0 and standard deviation 1. The error in the mean of ζ can be approximated as

$$\mathcal{E} \approx z_{\frac{1-c}{2}}\sqrt{\frac{p(1-p)}{n}}. \tag{1.24}$$

By inverting this relation, we get a formula for the number of shots as a function of the confidence level, the desired error, and the mean. Since the mean is unknown, we can find a bound for the number of shots: the standard deviation has a maximum at $p = 1/2$, so our approximate number of shots becomes

$$n \approx \left(\frac{z_{\frac{1-c}{2}}}{2\mathcal{E}}\right)^2. \tag{1.25}$$

For a 95% confidence interval, the critical value is known to be $z_{0.025} = 1.96$. An error between 2% and 3% can be achieved appropriately with 1100-2400 shots. We chose $n = 2000$ for the experiments reported in chapter 3.[27]

---

26. See, e.g., chapter 7 of [137], especially section 7.5, or [138] for references on this topic.

27. A 2020 survey by Patel *et al.* [139] compared how different IBM quantum systems perform with different settings at various standard computational tasks. Its observations represent invaluable practical information for IBM Quantum users.

Chapter 2

Pure and Mixed State Tomography Protocols

This chapter presents two quantum state tomography protocols – one for pure states, the other for mixed states. The former is accompanied by an experimental setup that can readily generate arbitrary, pure, path-polarization states. A preliminary version of this proposal was explored in [140]. The final version was published as [44], on which part of this chapter is heavily based. The second protocol, valid for arbitrary, mixed, path-polarization states, generalizes the first one. It is followed by a necessary digression on how to ensure positive semidefiniteness in the reconstructed mixed states via maximum likelihood estimation. Afterwards, the results of experimentally testing the pure state generation and characterization procedures speak for their usefulness and applicability. The final section addresses the number of measurements required for the pure state protocol, the centrality of the purity assumption, and the indirect character of the reconstruction schemes.

2.1 Pure State Generation and Tomography

2.1.1 State Generation

Consider a source of coherent, polarized light, such as a laser beam or single photons. Its polarization state can be described as a linear combination of horizontal and vertical polarization states, $|h\rangle$ and $|v\rangle$, which constitute a basis for a polarization qubit's Hilbert space. Upon entering an interferometer, the light's path state is written as a combination of $|x\rangle$ and $|y\rangle$ (x and y being labels for each path), a basis for the path qubit's respec-

tive Hilbert space. Thus, a pure, path-polarization state can be expressed in the tensor product basis $\{|x\rangle, |y\rangle\} \otimes \{|h\rangle, |v\rangle\} = \{|x\rangle \otimes |h\rangle, \ldots\} = \{|xh\rangle, \ldots\}$ and is of the form

$$\alpha\, e^{i\phi_\alpha}|xh\rangle + \beta\, e^{i\phi_\beta}|xv\rangle + \gamma\, e^{i\phi_\gamma}|yh\rangle + \delta|yv\rangle, \tag{2.1}$$

with $\alpha^2 + \beta^2 + \gamma^2 + \delta^2 = 1$. Such a state depends on 6 real parameters because the amplitudes must satisfy the normalization condition and the physical content in the state is independent of its global phase.
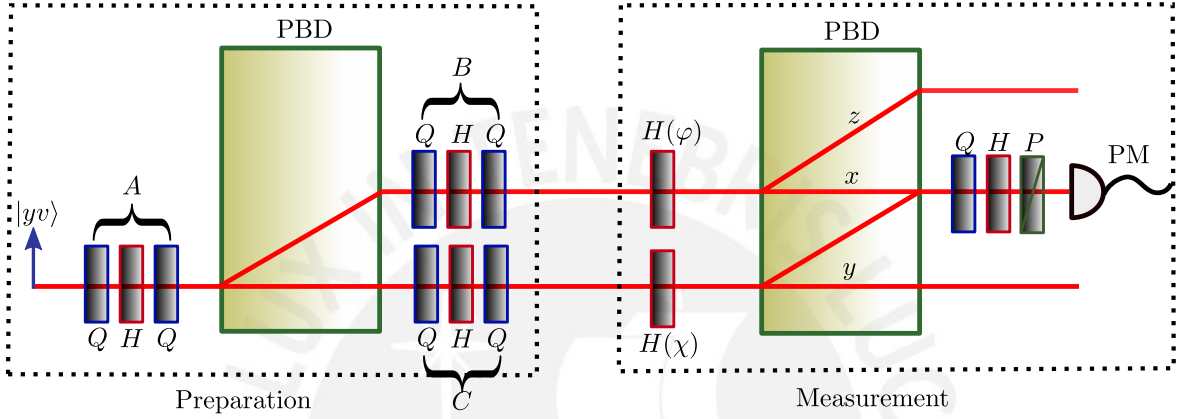

Figure 2.1: Proposed setup for preparing and measuring arbitrary pure states. In the preparation stage, a vertically polarized state travels along path y and undergoes a quarter-half-quarter (QHQ) polarization transformation. The resulting state passes through a polarizing beam displacer (PBD), which separates it along two paths in accordance with its polarization: the horizontal component is shifted towards path x, whereas the vertical component continues along path y. Each path contains a QHQ device set at specific angles (see equations 2.3), which prepare the state in equation 2.4. The state then enters the measurement stage, wherein it is acted upon by a half-wave plate on each path. Depending on their angles, the second PBD will combine the light in both paths accordingly. The x-arm exit presents a standard polarization tomography device (Q and H plates followed by a polarizer, P). The measurements are recorded, in a laser light experiment, by a power meter (PM), which completes the arrangement.

The above state can be prepared in the setup shown in figure 2.1. First, light in the state $|yv\rangle$ is submitted to two quarter-wave plates (Q) and a half-wave plate (H), which are labelled A in figure 2.1. The wave plates act on incident light as the polarization-

space linear operators

$$Q(\alpha) = \frac{1}{\sqrt{2}} \left[(1 - i\cos 2\alpha)|h\rangle\langle h| - i\sin 2\alpha(|h\rangle\langle v| + |v\rangle\langle h|) + (1 + i\cos 2\alpha)|v\rangle\langle v| \right],$$

(2.2a)

$$H(\beta) = -i[\cos 2\beta(|h\rangle\langle h| - |v\rangle\langle v|) + \sin 2\beta(|h\rangle\langle v| + |v\rangle\langle h|)],$$ (2.2b)

where α and β are the angles made by the plates' fast axes with respect to the vertical direction. The resulting state enters a polarizing beam displacer, PBD for short, which transmits (displaces) vertically (horizontally) polarized light. Two new QHQ devices, labelled B and C, operate on the separate light beams. If the three QHQ gadgets have their angles set to

$$A : Q\left(\frac{\pi}{4}\right) H\left(\frac{-4\theta_1 - \phi_\beta + \phi_\gamma - \phi_\alpha - 2\pi}{8}\right) Q\left(\frac{\pi}{4} - \theta_1\right),$$ (2.3a)

$$B : Q\left(\frac{\pi}{4}\right) H\left(\frac{2\phi_2 + \phi_\beta - \phi_\alpha}{4}\right) Q\left(\phi_2 - \frac{\pi}{4}\right),$$ (2.3b)

$$C : Q\left(\frac{\pi}{4}\right) H\left(\frac{-2\phi_1 - \phi_\gamma}{4}\right) Q\left(-\phi_1 - \frac{\pi}{4}\right),$$ (2.3c)

where the rightmost plate acts first, we can show straightforwardly that the resulting state is

$$\sin\theta_1 \sin\phi_2\, e^{i\phi_\alpha}|xh\rangle + \sin\theta_1 \cos\phi_2\, e^{i\phi_\beta}|xv\rangle + \cos\theta_1 \cos\phi_1\, e^{i\phi_\gamma}|yh\rangle + \cos\theta_1 \sin\phi_1|yv\rangle.$$ (2.4)

Up to normalization and global phase, equation 2.4 represents the most general pure, two-qubit state. It is worth mentioning that fewer wave plates can be sufficient and, most importantly, preferable, when only states that depend on fewer parameters are required.

2.1.2 State Tomography

Before presenting the tomography protocol for two-qubit, pure states, I will briefly review standard (single-qubit) polarization tomography. Consider a general polarization state of the form

$$|\xi\rangle = c_1|h\rangle + c_2 e^{ic_3}|v\rangle,$$ (2.5)

with $c_{1,2,3} \in \mathbb{R}$, and its equivalent density matrix $\rho_\xi = |\xi\rangle\langle\xi|$. Its characterization requires a quarter- and a half-wave plate set to β and α, respectively, followed by a polarizer

29

and a detector. The measured quantities (either laser intensities or photon counts) are proportional to

$$\mathcal{I}(\alpha, \beta) = \text{Tr}\big(P(0)H(\alpha)Q(\beta)\rho_\xi Q^\dagger(\beta)H^\dagger(\alpha)\big), \tag{2.6}$$

where $P(0) = |h\rangle\langle h|$ stands for a polarizer that projects incident polarization onto the horizontal state. By choosing α and β conveniently, we find that the four quantities

$$i_h = \mathcal{I}(0,0) = c_1^2, \tag{2.7a}$$

$$i_v = \mathcal{I}(\pi/4, 0) = c_2^2, \tag{2.7b}$$

$$i_d = \mathcal{I}(\pi/8, \pi/4) = \frac{1}{2}(c_1^2 + c_2^2 + 2c_1 c_2 \cos c_3), \tag{2.7c}$$

$$i_r = \mathcal{I}(-\pi/8, 0) = \frac{1}{2}(c_1^2 + c_2^2 + 2c_1 c_2 \sin c_3), \tag{2.7d}$$

suffice to reconstruct $|\xi\rangle$. We call them the *horizontal, vertical, diagonal,* and *right-circular* components of $|\xi\rangle$. The amplitudes are equal to the square roots of i_h and i_v; the sign between them is fixed by the phase

$$c_3 = \tan^{-1}\left(\frac{2\,i_r - i_h - i_v}{2\,i_d - i_h - i_v}\right). \tag{2.8}$$

The signs of the numerator and denominator of equation 2.8 remove any ambiguity in the calculation of c_3. If, for instance, $2\,i_r - i_h - i_v = 0$, the sign of $2\,i_d - i_h - i_v$ decides whether $c_3 = 0$ or $c_3 = \pi$.

Having prepared the state in equation 2.4, the measurement stage shown in figure 2.1 serves to characterize it completely. First, two separate half-wave plates, one in each arm, act on the state. Thereupon, it enters a second PBD and thus exits the interferometer. The angles φ and χ of the respective half-wave plates in the x- and y-arms determine what is measured in the x-arm exit of the second PBD; the other two exits are led to beam dumps. Just as in the single qubit case, the final state is acted on by quarter- and half-wave plates, then by a polarizer, and finally a detector. The measurements done on the exit beam and the subsequent state reconstruction process are described in the rest of this section.

For clarity's sake, consider the most general, pure, two-qubit state:

$$|\psi\rangle = \alpha\,e^{i\phi_\alpha}|xh\rangle + \beta\,e^{i\phi_\beta}|xv\rangle + \gamma\,e^{i\phi_\gamma}|yh\rangle + \delta\,e^{i\phi_\delta}|yv\rangle. \tag{2.9}$$

In order to identify it without any extra information,[1] we must ascertain the four amplitudes as well as the 6 possible relative phases. Let us submit $|\psi\rangle$ to the measuring

---

1. In contrast to Gonzales *et al.*'s protocol [75].

device in figure 2.1. The state $|\psi\rangle_x$ that results from projecting on the x-arm after the second PBD is

$$|\psi\rangle_x = |x\rangle\big[\big(e^{i\phi_\gamma}\gamma\cos 2\chi + e^{i\phi_\delta}\delta\sin 2\chi\big)|h\rangle + \big(-e^{i\phi_\beta}\beta\cos 2\varphi + e^{i\phi_\alpha}\alpha\sin 2\varphi\big)|v\rangle\big]. \quad (2.10)$$

Suppose, without any loss of generality, that we work with a beam of coherent laser light. When the half-wave plates at the beginning of the measurement stage are set to $\varphi = 0$ and $\chi = \pi/4$, then the intensities which correspond to equations 2.7–i.e., which are obtained with the final quarter- and half-wave plates set at the respective angles–are proportional to

$$i_1 = \delta^2, \quad (2.11a)$$

$$i_2 = \beta^2, \quad (2.11b)$$

$$i_3 = \frac{1}{2}\big(\beta^2 + \delta^2 - 2\beta\delta\cos(\phi_\beta - \phi_\delta)\big), \quad (2.11c)$$

$$i_4 = \frac{1}{2}\big(\beta^2 + \delta^2 - 2\beta\delta\sin(\phi_\beta - \phi_\delta)\big). \quad (2.11d)$$

If instead the angles are $\varphi = \pi/4$ and $\chi = 0$, the corresponding intensities are

$$i_5 = \gamma^2, \quad (2.12a)$$

$$i_6 = \alpha^2, \quad (2.12b)$$

$$i_7 = \frac{1}{2}\big(\alpha^2 + \gamma^2 + 2\alpha\gamma\cos(\phi_\alpha - \phi_\gamma)\big), \quad (2.12c)$$

$$i_8 = \frac{1}{2}\big(\alpha^2 + \gamma^2 + 2\alpha\gamma\sin(\phi_\alpha - \phi_\gamma)\big). \quad (2.12d)$$

The diagonal and right-circular components become, for $\varphi = \chi = \pi/4$,

$$i_9 = \frac{1}{2}\big(\alpha^2 + \delta^2 + 2\alpha\delta\cos(\phi_\alpha - \phi_\delta)\big), \quad (2.13a)$$

$$i_{10} = \frac{1}{2}\big(\alpha^2 + \delta^2 + 2\alpha\delta\sin(\phi_\alpha - \phi_\delta)\big), \quad (2.13b)$$

whereas for $\varphi = \chi = 0$ they take the forms

$$i_{11} = \frac{1}{2}\big(\beta^2 + \gamma^2 - 2\beta\gamma\cos(\phi_\beta - \phi_\gamma)\big), \quad (2.14a)$$

$$i_{12} = \frac{1}{2}\big(\beta^2 + \gamma^2 - 2\beta\gamma\sin(\phi_\beta - \phi_\gamma)\big), \quad (2.14b)$$

respectively. In the last two configurations (equations 2.13 and 2.14), the horizontal and vertical components are equal to $i_{1,2,5,6}$, so they do not provide additional information. By direct inspection, the absolute values of the four amplitudes, α, β, γ, and δ, are found

to be equal to the square roots of i_6, i_2, i_5 and i_1. This way, the normalization condition, $\alpha^2 + \beta^2 + \gamma^2 + \delta^2 = 1$ acquires a functional meaning: any measured intensity must be divided by $i_0 = i_1 + i_2 + i_5 + i_6$ so as to correspond to $i_{1,...,12}$. The prescription for computing four relative phases completes the protocol:

$$\phi_\beta - \phi_\delta = \tan^{-1}\left(\frac{2\,i_4 - i_2 - i_1}{2\,i_3 - i_2 - i_1}\right), \tag{2.15a}$$

$$\phi_\alpha - \phi_\gamma = \tan^{-1}\left(\frac{2\,i_8 - i_6 - i_5}{2\,i_7 - i_6 - i_5}\right), \tag{2.15b}$$

$$\phi_\alpha - \phi_\delta = \tan^{-1}\left(\frac{2\,i_{10} - i_6 - i_1}{2\,i_9 - i_6 - i_1}\right), \tag{2.15c}$$

$$\phi_\beta - \phi_\gamma = \tan^{-1}\left(\frac{2\,i_{12} - i_2 - i_5}{2\,i_{11} - i_2 - i_5}\right), \tag{2.15d}$$

where the same caveat applies as for c_3 in equation 2.8. The other relative phases are obtained by subtracting conveniently the above equations: $\phi_\alpha - \phi_\beta = (\phi_\alpha - \phi_\delta) - (\phi_\beta - \phi_\delta)$ and $\phi_\delta - \phi_\gamma = (\phi_\alpha - \phi_\gamma) - (\phi_\alpha - \phi_\delta)$.

A final comment on the question of optimality is in order. At first sight, it might seem as if intensities $i_{1,...,10}$ suffice to complete the protocol–after all, only 3 phases are necessary to determine the state completely. However, suppose that we were given an unknown state with one amplitude equal to zero, e.g., $\delta = 0$. In this case, it would not be possible to use equations 2.15a and 2.15c to compute $\phi_\beta - \phi_\delta$ and $\phi_\alpha - \phi_\delta$ (and, from them, $\phi_\alpha - \phi_\beta$) because both the numerator and denominator of the inverse tangents' arguments would equal zero. That the three determinate phases of this state can be obtained from equations 2.15b and 2.15d illustrates the necessity of measuring twelve intensities to reconstruct arbitrary, unknown states.

2.2 Mixed State Tomography

2.2.1 Tomography Proposal

In practice, all quantum states are mixed, for no degree of freedom evolves perfectly isolated from the influence of any other degree of freedom. Yet, depending on the context, the states produced in a laboratory can be safely considered pure. For instance, whenever the laser source is stable, monochromatic, and linearly polarized, any additional polarization and wavelength modes are effectively suppressed, so it is reasonable

to assume state purity and use a protocol such as the one presented in section 2.1.2 in order to characterize the state. The degree to which this assumption is valid can be assessed by comparing experimental results to the theoretical predictions [34, 35, 75]. In contrast, settings wherein, e.g., photon-pair production takes place are prone to involve additional unwanted modes, which can undermine the purity assumption. The need becomes apparent in such cases to assume that the state is mixed and employ an appropriate tomography scheme.

Regarding our path-polarization states, for them to be mixed means that their matrix representation in, say, the $\{|x\rangle, |y\rangle\} \otimes \{|h\rangle, |v\rangle\}$ basis has the general form

$$\rho_0 = \begin{pmatrix} c_1 & c_5 + ic_6 & c_7 + ic_8 & c_9 + ic_{10} \\ c_5 - ic_6 & c_2 & c_{11} + ic_{12} & c_{13} + ic_{14} \\ c_7 - ic_8 & c_{11} - ic_{12} & c_3 & c_{15} + ic_{16} \\ c_9 - ic_{10} & c_{13} - ic_{14} & c_{15} - ic_{16} & c_4 \end{pmatrix}, \tag{2.16}$$

where $c_{1,\dots,16}$ are real numbers, $c_{1,2,3,4}$ are positive, and they satisfy

$$\operatorname{Tr} \rho_0 = c_1 + c_2 + c_3 + c_4 = 1, \quad \text{and} \quad \operatorname{Tr} \rho_0^2 \leq 1. \tag{2.17}$$

Such a state can be characterized from 16 measurements made with the device shown in figure 2.2. The action of quarter- and half-wave plates placed in both arms produces different combinations of the components of the state ρ_0, which enter the second PBD. The resulting state is

$$\rho_1 = H(\eta_y)Q(\lambda_y)H(\eta_x)Q(\lambda_x)\rho_0\, Q^\dagger(\lambda_x)H^\dagger(\eta_x)Q^\dagger(\lambda_y)H^\dagger(\eta_y), \tag{2.18}$$

where the respective path-space projector operators $(P_x = |x\rangle\langle x|, P_y = |y\rangle\langle y|)$ are implicit. As the state exits the second PBD, the y- and z-arms lead to beam dumps. We project along the x-arm and place quarter- and half-wave plates followed by a polarizer set to horizontal. Thereafter, the measurements can be recorded with either a power meter (for experiments with laser light) or a single photon counter (in the case of quantum light). The detected quantity is proportional to the only non-vanishing component of the operator

$$\rho_2 = P_h H(\nu)Q(\mu)P_x O_{\text{PBD}}\, \rho_1\, O_{\text{PBD}}^\dagger P_x Q^\dagger(\mu)H^\dagger(\nu)P_h, \tag{2.19}$$

where O_{PBD} represents the action of the beam displacer.

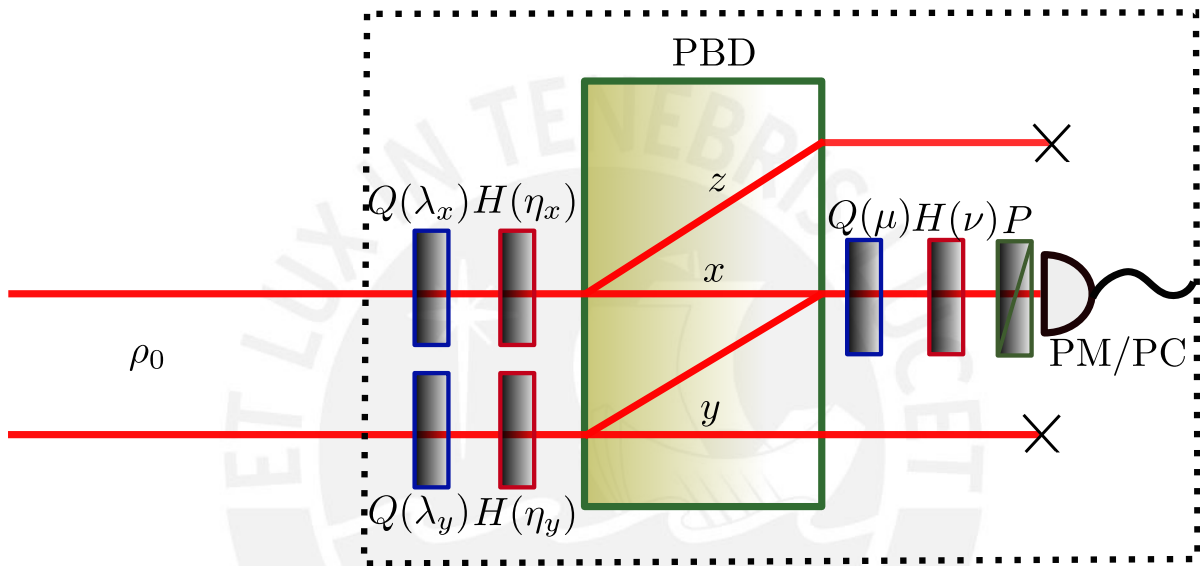Figure 2.2: Proposed setup for mixed state tomography. An arbitrary path-polarization state ρ_0 enters the measurement device, which consists of Q and H plates in each path, a polarizing beam displacer, Q and H plates, a linear polarizer, and a detector (either a power meter or a photon counter). Different wave plate configurations result in 16 measurements that serve to reconstruct the incident state.

Denote by n_i the coincidence count, in a photonic experiment, of a given configuration of the angles $\lambda_{x/y}, \eta_{x/y}, \mu$, and ν. The settings shown in table 2.1 yield coincidences that are functions of the state parameters. Said functions are

$$n_1 = c_3, \ n_2 = \frac{1}{2}(c_2 + c_3 - 2c_{12}), \ n_3 = \frac{1}{2}(c_2 + c_3 + 2c_{11}),$$

$$n_4 = c_2, \ n_5 = c_1, \ n_6 = \frac{1}{2}(c_1 + c_2 + 2c_5), \ n_7 = \frac{1}{2}(c_1 + c_2 + 2c_6),$$

$$n_8 = c_4, \ n_9 = \frac{1}{2}(c_1 + c_3 + 2c_8),$$

$$n_{10} = \frac{1}{4}(c_1 + c_3 + 2c_4 + 2c_8 - 2c_9 + 2c_{10} + 2c_{15} + 2c_{16}),$$

$$n_{11} = \frac{1}{4}(c_1 + c_3 + 2c_4 + 2c_8 + 2c_9 + 2c_{10} + 2c_{15} - 2c_{16}),$$

$$n_{12} = \frac{1}{4}\Big(3c_2 + c_4 + 2c_{13} - 2\sqrt{2}c_{14}\Big), \ n_{13} = \frac{1}{2}(c_1 + c_4 + 2c_{10}),$$

$$n_{14} = \frac{1}{2}(c_2 + c_4 + 2c_{14}), \ n_{15} = \frac{1}{2}(c_1 + c_3 - 2c_7),$$

$$n_{16} = \frac{1}{4}\Big(c_1 + c_2 + c_3 + c_4 - 2c_7 + 2c_{14} - \sqrt{2}(c_5 + c_6 - c_9 + c_{10} - c_{11} + c_{12} + c_{15} - c_{16})\Big). \tag{2.20}$$

After inverting the previous expressions, we find that the parameters as functions of the coincidences make up the system

$$c_1 = n_5, \ c_2 = n_4, \ c_3 = n_1, \ c_4 = n_8,$$

$$c_5 = \frac{1}{2}(2n_6 - n_4 - n_5), \ c_6 = \frac{1}{2}(2n_7 - n_4 - n_5),$$

$$c_7 = \frac{1}{2}(n_1 + n_5 - 2n_{15}), \ c_8 = \frac{1}{2}(2n_9 - n_1 - n_5),$$

$$c_9 = \frac{1}{2}\Big(n_1 - n_2 - n_3 - n_5 + n_6 + n_7 - n_8 - n_9 + 2n_{11} - \sqrt{2}n_{14} - \sqrt{2}n_{15} + 2\sqrt{2}n_{16}\Big),$$

$$c_{10} = \frac{1}{2}(2n_{13} - n_5 + n_8), \ c_{11} = \frac{1}{2}(2n_3 - n_1 - n_4),$$

$$c_{12} = \frac{1}{2}(n_1 + n_4 - 2n_{14}), \ c_{13} = \frac{1}{2}\Big(4n_{12} + 2\sqrt{2}n_{14} - \Big(3 + \sqrt{2}\Big)n_4 - \Big(1 + \sqrt{2}\Big)n_8\Big),$$

$$c_{14} = \frac{1}{2}(2n_{14} - n_4 - n_8), \ c_{15} = \frac{1}{2}(n_5 - n_8 - 2n_9 + 2n_{10} + 2n_{11} - 2n_{13}),$$

$$c_{16} = \frac{1}{2}\Big(n_1 - n_2 - n_3 - n_5 + n_6 + n_7 - n_8 - n_9 + 2n_{10} - \sqrt{2}n_{14} - \sqrt{2}n_{15} + 2\sqrt{2}n_{16}\Big), \tag{2.21}$$

which completes the prescription for reconstructing an arbitrary, mixed, path-polarization state.

	$Q(\lambda_x)$	$H(\eta_x)$	$Q(\lambda_y)$	$H(\eta_y)$	$Q(\mu)$	$H(\nu)$
n_1	0	0	0	0	0	$\pi/4$
n_2	0	0	0	0	$\pi/4$	$\pi/8$
n_3	0	0	0	0	0	$\pi/8$
n_4	0	$\pi/4$	0	0	0	0
n_5	0	$\pi/4$	0	0	0	$\pi/4$
n_6	0	$\pi/4$	0	0	$\pi/4$	$\pi/8$
n_7	0	$\pi/4$	0	0	0	$-\pi/8$
n_8	$\pi/4$	0	0	$\pi/4$	0	0
n_9	$\pi/4$	0	0	$\pi/4$	0	$\pi/4$
n_{10}	$\pi/4$	0	0	$\pi/4$	$\pi/4$	$-\pi/8$
n_{11}	$\pi/4$	0	0	$\pi/4$	0	$-\pi/8$
n_{12}	$\pi/4$	0	$\pi/8$	0	0	0
n_{13}	$\pi/2$	$\pi/4$	0	$\pi/4$	0	$-\pi/8$
n_{14}	$\pi/4$	$\pi/8$	$\pi/4$	$\pi/4$	0	0
n_{15}	$\pi/4$	$\pi/8$	$\pi/4$	$\pi/4$	0	$\pi/4$
n_{16}	$\pi/4$	$\pi/8$	$\pi/4$	$\pi/4$	$\pi/4$	$\pi/8$

Table 2.1: Tomography angles of the plates in the measurement device (see figure 2.2) for the coincidence measurements n_i that determine an arbitrary, mixed, path-polarization state.

2.2.2 Maximum Likelihood Estimation

Unfortunately, the states produced by the mixed state tomography protocol are not always physical. Any set of positive numbers $\{n_i\}_{i=1,\ldots,16}$ yields, via equations 2.21 and 2.16, a Hermitian, unit-trace matrix. For it to represent a physical state, said matrix must also have non-negative eigenvalues–i.e., it must be positive semidefinite. Due to random fluctuations in the measured counts, matrices with negative eigenvalues are likely to arise–especially when the target states have a high degree of purity [68], which implies that most of their eigenvalues are close to zero. The customary approach towards this problem [65, 68, 141–143] boils down to finding a matrix $T(t_{i=1,\ldots,16})$, whose parameters depend on the measured data $\{n_i\}$, such that

$$\rho_p(t_i) = \frac{T^\dagger(t_i)T(t_i)}{\mathrm{Tr}(T^\dagger(t_i)T(t_i))} \tag{2.22}$$

is a physical state by construction. The question of how to determine the parameters t_i that best correlate to the data can be answered by the maximum likelihood estimation (MLE) procedure to which this section is devoted.

Following James *et al.* [68], let ρ be the theoretical density matrix of the state generated in the experimental setup that precedes the arrangement depicted in figure 2.2. The state

$$\rho_{(\lambda_x,\lambda_y,\eta_x,\eta_y)} = (O_{\mathrm{PBD}}H(\eta_x)Q(\lambda_x)H(\eta_y)Q(\lambda_y))\rho(O_{\mathrm{PBD}}H(\eta_x)Q(\lambda_x)H(\eta_y)Q(\lambda_y))^\dagger \tag{2.23}$$

exits the interferometer, is projected along path x, and traverses the wave plates $Q(\mu)$, $H(\nu)$, and a horizontally-oriented polarizer, thereby yielding the expected counts

$$n_\zeta = \mathrm{Tr}\big(|xh\rangle\langle xh|H(\nu)Q(\mu)\rho_{(\lambda_x,\lambda_y,\eta_x,\eta_y)}Q(\mu)^\dagger H(\nu)^\dagger\big), \tag{2.24}$$

whose experimental counterparts are $\left\{n_\zeta^{(\mathrm{exp})}\right\}$, with $\zeta = (\lambda_x,\lambda_y,\eta_x,\eta_y,\mu,\nu)$ an index that runs from 1 to 16 (cf. equation 2.6). If, by hypothesis, all measurements occur independently from each other and the errors in each measurement follow a Gaussian distribution, then the probability that the matrix ρ could produce the 16 measured coincidences is proportional to

$$\prod_{\zeta=1}^{16} \exp\left[-\frac{\left(n_\zeta - n_\zeta^{(\mathrm{exp})}\right)^2}{2\sigma_\zeta^2}\right], \tag{2.25}$$

37

with the standard deviation of each Gaussian approximated by $\sigma_\zeta = \sqrt{n_\zeta}$. Additionally, consider the density matrix in equation 2.22 with $T(t_i)$ given, for instance, by the lower triangular matrix

$$
T(t_i) = \begin{pmatrix}
t_1 & 0 & 0 & 0 \\
t_5 + it_6 & t_2 & 0 & 0 \\
t_{11} + it_{12} & t_7 + it_8 & t_3 & 0 \\
t_{15} + it_{16} & t_{13} + it_{14} & t_9 + it_{10} & t_4
\end{pmatrix},
\tag{2.26}
$$

and the expected coincidence counts by

$$
n_\zeta^{(t)} = \mathrm{Tr}\big(|xh\rangle\langle xh|H(\nu)Q(\mu)\rho_p(t_1,\ldots,t_{16})Q(\mu)^\dagger H(\nu)^\dagger\big).
\tag{2.27}
$$

Then, the probability that $\rho_p(t_1,\ldots,t_{16})$ produces the measured counts is

$$
P = \frac{1}{N_0}\prod_{\zeta=1}^{16}\exp\left[-\frac{\left(n_\zeta^{(t)} - n_\zeta^{(\exp)}\right)^2}{2\sigma_\zeta^2}\right].
\tag{2.28}
$$

Maximizing P is equivalent to minimizing

$$
\mathcal{L} = \sum_{\zeta=1}^{16}\frac{\left[\mathrm{Tr}\big(|xh\rangle\langle xh|H(\nu)Q(\mu)\rho_p(t_1,\ldots,t_{16})Q(\mu)^\dagger H(\nu)^\dagger\big) - n_\zeta^{(\exp)}\right]^2}{2\sigma_\zeta^2(t_1,\ldots,t_{16})},
\tag{2.29}
$$

the so-called likelihood function, where $\sigma_\zeta(t_1,\ldots,t_{16}) = \sqrt{n_\zeta^{(t)}}$. Given a data set $\left\{n_\zeta^{(\exp)}\right\}$, the function $\mathcal{L}$ can be readily minimized with a numerical optimization algorithm. The t_i which minimize $\mathcal{L}$ are then inserted into $T(t_i)$, from where the desired physical state follows via equation 2.22.

Finally, a word of caution about maximum likelihood estimation. It has been pointed out [144] that MLE frequently results in matrices with one or more zero eigenvalues,[2] which implies that some measurement outcomes will never occur. Such an absolute implication conflicts with the inherent uncertainty of experimental data. In addition, MLE turns out single states (so-called point estimates) and no meaningful confidence region for them [145]. It has also been shown [146] that MLE and, more generally, any other estimator which imposes physicality is biased and will thus introduce systematic errors in quantities such as fidelity, bipartite negativity, and Fisher information that are derived from its output. From a mathematical standpoint, as a consequence of the

---

2. As in, most prominently, the example presented in the seminal paper [68].

asymptotic normality property, the MLE estimator will not be a good approximation to the real state when the latter is pure.[3] Fortunately, there exist proposals that tackle these flaws: Bayesian mean estimation returns a matrix with no zero eigenvalues and with error bars [144]; likelihood-ratio confidence regions generalize error bars for single point estimates [145]. Simple linear inversion (e.g., equations 2.21) is an unbiased estimator, so its use, when applicable, skirts systematic errors. Moreover, regardless of their physicality, matrices obtained via linear inversion can produce useful bounds for information-theoretic quantities [146]. All of which is to say that, while useful for fixing non-positive semidefinite results, MLE should be used judiciously where appropriate and its shortcomings should be addressed.

2.3 Experimental Realization and Results

As reported in [44], my colleagues and I put the pure state tomography protocol to test by using as a state source a linearly-polarized HeNe laser (633 nm) with output power of 11.5 mW. We prepared three sets of states with either the state generation device of section 2.1.1 or simpler wave plate setups. Afterwards, we followed the prescription of section 2.1.2 to measure the required intensities and reconstruct the states. It is important to note that, before each intensity measurement, we had to offset a path-difference phase by slightly realigning the second polarizing beam displacer. The results presented in this section were obtained from eight repetitions of each experiment. The uncertainties in the parameters were calculated as $\sqrt{\sigma_a^2 + \sigma_s^2}$, where σ_a is the propagated error made in reading the angles off the plates' mounts, and σ_s is the standard deviation of the eight measurements. We employed the squared fidelity between a target state and its experimental reconstruction,

$$\mathcal{F}^2(|\phi_{\text{target}}\rangle\langle\phi_{\text{target}}|, |\phi_{\text{exp}}\rangle\langle\phi_{\text{exp}}|) = |\langle\phi_{\text{target}}|\phi_{\text{exp}}\rangle|^2, \tag{2.30}$$

as a figure of merit for our results.

We first produced the Bell state

$$|\Phi^+\rangle = \frac{1}{\sqrt{2}}|xh\rangle + \frac{1}{\sqrt{2}}|yv\rangle. \tag{2.31}$$

---

3. See, e.g., [64], in particular section 3, for more details on the asymptotic properties of MLE and several other state estimators.
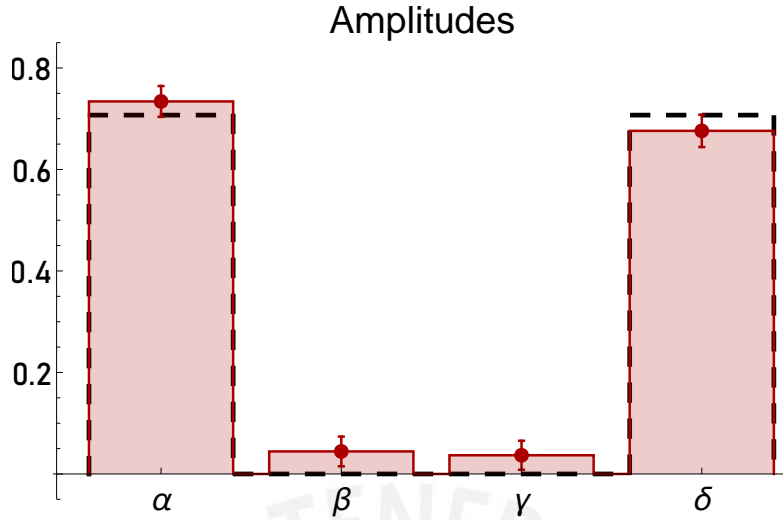
Figure 2.3: Experimentally reconstructed amplitudes of the Bell state $|\Phi^+\rangle$. The theoretical values are shown with dashed lines and correspond to $\alpha = \delta = 1/\sqrt{2} \approx 0.71$ and $\beta = \gamma = 0$. Experimental values are shown as solid bars, atop of which a small error bar illustrates the uncertainty in each parameter.

States in the Bell basis play a central role in quantum information processing. Hence, testing new techniques with them is standard practice. This particular state has only one determinate relative phase, $\phi_\alpha - \phi_\delta = 0$ in the notation of section 2.1.2. Our experiments yielded an average value of $\phi_\alpha - \phi_\delta = 0° \pm 7°$. Within experimental precision, this result matches the theoretical value satisfactorily. As for the amplitudes, they are shown in figure 2.3, where we can see that they, too, are within experimental precision from the theoretical values. Furthermore, the squared fidelity between $|\Phi^+\rangle$ and its experimental counterpart was found to be $\mathcal{F}^2 = 0.994 \pm 0.062$, another excellent fit.

For our second test, we prepared the state

$$|\Psi\rangle = \frac{1}{2}e^{i\frac{9\pi}{10}}|xh\rangle + \frac{1}{2}e^{-i\frac{2\pi}{5}}|xv\rangle + \frac{1}{2}e^{i\frac{\pi}{2}}|yh\rangle + \frac{1}{2}|yv\rangle \qquad (2.32)$$

with the arrangement described in section 2.1.1. In this case, no parameter vanishes: all basis states have the same weight, whereas the relative phases are all different and non-vanishing. Indeed, we note that $\phi_\alpha - \phi_\delta = 9\pi/10 = 162°$, $\phi_\beta - \phi_\delta = -2\pi/5 = -72°$, and $\phi_\gamma - \phi_\delta = \pi/2 = 90°$. The remaining relative phases are redundant, but they can be, in any case, immediately computed from the given ones. Figure 2.4 compares the theoretical and experimental phases, indicating again good agreement, to within
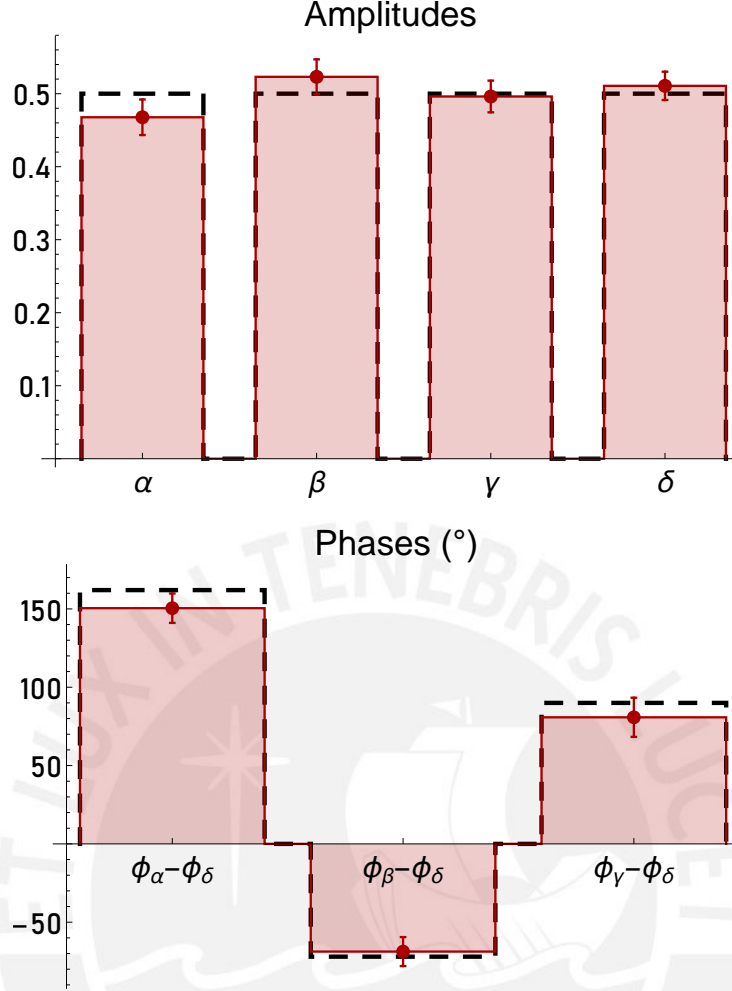
Figure 2.4: Experimentally reconstructed amplitudes (top) and relative phases (bottom) of the state $|\Psi\rangle$. The theoretical amplitudes, each equal to 0.5, are indicated with dashed lines, as are the theoretical relative phases $\phi_\alpha - \phi_\delta = 9\pi/10 = 162°$, $\phi_\beta - \phi_\delta = -2\pi/5 = -72°$, and $\phi_\gamma - \phi_\delta = \pi/2 = 90°$. The experimental values are shown as bars with solid lines; their uncertainties are given by the small error bar atop each bar.

experimental precision; it also displays the reconstructed amplitudes and how well they match the predictions. Fidelity calculations show that the prepared state largely agrees with the target state: $\mathcal{F}^2 = 0.986 \pm 0.044$.

For our last case, we studied a family of states that are functions of one variable angle. Incidentally, the tested states can be used to simulate the dynamics of an open system that interacts with an environment. Either the path or polarization qubit can play either role. In the case that concerns us, the simulated dynamics corresponds to the so-called amplitude-damping channel, which represents an energy loss process from a system
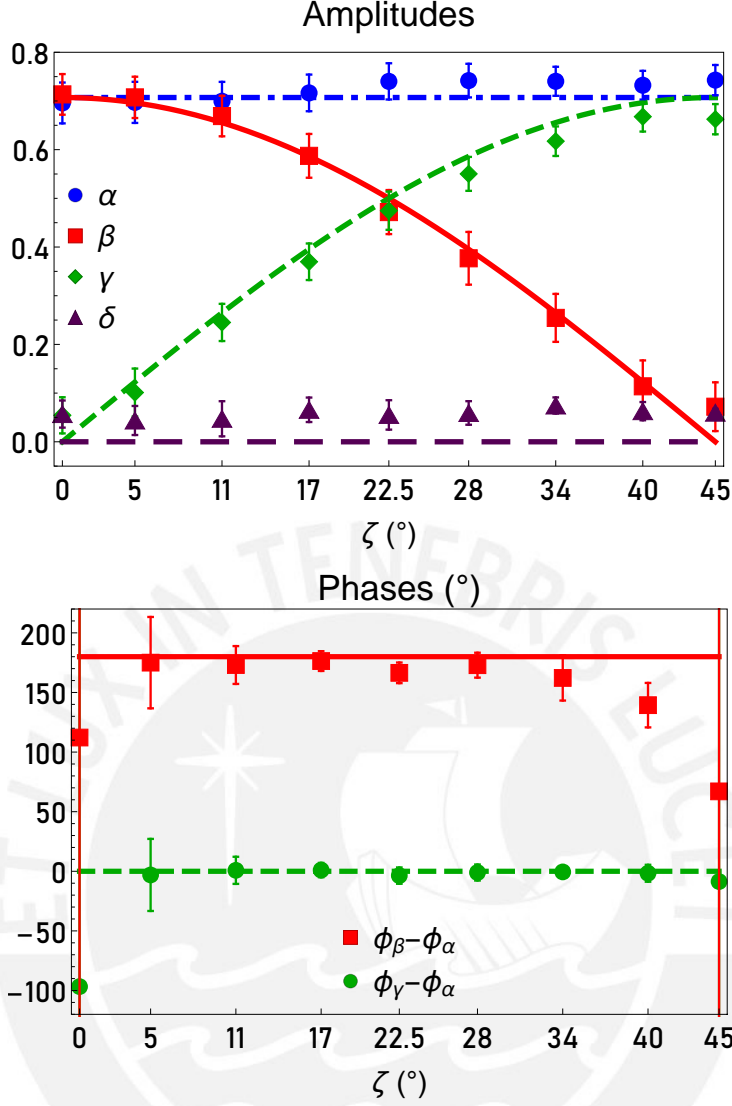
Figure 2.5: Experimentally reconstructed amplitudes (top) and non-vanishing relative phases (bottom) of the state $|\Gamma\rangle$ as functions of the angle ζ. The dashed and solid lines show the parameters' theoretical values; the constant amplitudes are $\alpha = 1/\sqrt{2} \approx 0.71$ and $\delta = 0$, whereas the phases are $\phi_\beta - \phi_\alpha = \pi = 180°$ and $\phi_\gamma - \phi_\alpha = 0°$. Each marker with its respective error bar indicates a experimental result and its uncertainty. The error bars for both $\phi_\beta - \phi_\alpha$ and $\phi_\gamma - \phi_\alpha$ become infinite when $\zeta = 0°$ and $45°$.

to its noisy environment, e.g., photon emission by a two-level atom.[4] This process is schematically described by the transition $|1\rangle_S|0\rangle_E \rightarrow \sqrt{1-\eta}|1\rangle_S|0\rangle_E + \sqrt{\eta}|0\rangle_S|1\rangle_E$. Here, one excitation goes from the system (S) to the environment (E) at a so-called damping rate given by the probability η that the photon is emitted. The previous digression

---

4. See, e.g., section 8.3.5 of [72] for more details on the damping channel.

notwithstanding, the target states we prepared were of the form

$$|\Gamma\rangle = \frac{1}{\sqrt{2}}|xh\rangle - \frac{1}{\sqrt{2}}\cos 2\zeta|xv\rangle + \frac{1}{\sqrt{2}}\sin 2\zeta|yh\rangle. \qquad (2.33)$$

In this family of states, one amplitude is $1/\sqrt{2}$, another is zero, and the other two vary with ζ; with regard to the relative phases, only $\phi_\beta - \phi_\alpha = \pi = 180°$ and $\phi_\gamma - \phi_\alpha = 0°$ are relevant. Figure 2.5 presents the results of applying the tomography protocol to 9 samples of the state $|\Gamma\rangle$, with $\zeta \in [0, \pi/4]$. As before, the experimental states mostly comport to their theoretical counterparts. We found that the squared fidelities between target states and their respective experimental states ranged from $\mathcal{F}^2 = 0.984 \pm 0.080$ to $\mathcal{F}^2 = 0.994 \pm 0.089$. In figure 2.5, two cases seem to show major discrepancies between prediction and reconstruction. However, when inspected closely, an explanation becomes apparent: for $\zeta = 0°$, the target state is $|\Gamma\rangle = |x\rangle \otimes (|h\rangle - |v\rangle)/\sqrt{2}$, which has two indeterminate phases, ϕ_γ and ϕ_δ, whereas for $\zeta = 45°$ the state takes the form $|\Gamma\rangle = (|x\rangle + |y\rangle) \otimes |h\rangle/\sqrt{2}$, for which ϕ_β and ϕ_δ are indeterminate. Randomly varying experimental measurements occur concomitantly with indeterminate phases in the theoretical states. The conspicuous standard deviations in figure 2.5 are a natural consequence thereof.

2.4 Discussion

We have demonstrated a tomography protocol that requires no estimation postprocessing because the states produced from its 12 measurements are physical by construction. This procedure can be simplified if, after a few initial measurements, the experimentalist concludes that either no amplitude is zero or which amplitude is zero.[5] In the former case, 10 measurements are necessary: 4 for the amplitudes, 6 for the three non-redundant determinate phases (see equations 2.11–2.14). In the latter, the indeterminate phases can be discounted, and the state can be characterized with 10 measurements (as in the case of $|\Gamma\rangle$) or just 8 (e.g., the Bell state $|\Phi^+\rangle$). Although Heinosaari *et al.* [74] had the purity assumption in mind when they referred to "prior information", our pure state scheme can, under adequate prior information, reconstruct states from even less measurements than the minimum of 9 proved by them.

---

5. See footnote 5 in [147] for a simple example of this in the description of spin states.

The purity assumption, despite not addressing states in all their generality, is of paramount importance for quantum information theory and tomography. So-called quantum state verification protocols are designed to certify whether or not a given state is the target state [148–150]. In certain information-theoretical scenarios where one party wishes to fool such a protocol, it can be proved that said party cannot benefit from employing mixed states [151]. On the other hand, numerical simulations have shown that if, instead of having an estimation algorithm performed on them, reconstructed multi-qubit density matrices are forced to be pure (i.e., their highest eigenvalue is set to 1 and the rest to 0), then their fidelity with respect to their target states is comparable to that between the latter states and the ones estimated via maximum likelihood, an enormously more expensive procedure than forcing purity [152]. These results underscore the importance of the purity assumption on economic grounds. The study of and interest in pure states is, therefore, more than justified.

Both the pure and mixed state tomography proposals presented in this chapter are of an indirect nature. In the pure case, equations 2.11–2.14 give access separately to both the squared amplitude and phase of the complex coefficients in the general wave function of equation 2.9, whereas the mixed protocol prescribes 16 measurements (equations 2.20) that must be combined in elaborate ways (equations 2.21) in order to produce the target state (equation 2.16). Lundeen *et al.*'s direct state measurement scheme for pure states [87] was not a tomography protocol, on account of its lack of universality [89]. Gross *et al.*'s analysis of this procedure [96] rebutted its claimed directness: individual amplitudes cannot be reconstructed without knowing the normalization constant, which requires full knowledge of the amplitudes. Still, Lundeen *et al.*'s technique does provide the ratios between amplitudes directly. For their part, Zhu *et al.* [92] contended that their modified direct state tomography is an actual direct method. In any event, as the literature illustrates, such claims should always be evaluated with care.

Chapter 3

Weak Values and State Characterization with Strong Measurements

This chapter first derives a proposal (based on the works of Denkmayr *et al.* [45, 46]) for characterizing the weak values of a Pauli spin operator via measurements not constrained to the weak interaction regime. Then, two implementations of said scheme are outlined: one in an all-optical laboratory setting, the other in a quantum computational context; the latter account includes an associated state measurement protocol. The proposal's realization in IBM's quantum systems is described before expounding the results and contrasting them with the theoretical predictions. To close, the place of this work and its contributions to the field are discussed.

3.1 Weak Value Measurement Scheme

Consider two qubits a and b along with their respective bases $\{|0_a\rangle, |1_a\rangle\}$ and $\{|0_b\rangle, |1_b\rangle\}$. Without any loss of generality, let qubit a be the system of interest and qubit b the pointer of a measurement apparatus. The act of measuring the observable $\sigma_{\mathbf{n}}^a$ can be described by the unitary operator

$$U(\epsilon) = \exp\big(-i\epsilon\sigma_{\mathbf{n}}^a \otimes \sigma_z^b\big), \tag{3.1}$$

where $\epsilon > 0$ quantifies the strength of the system-pointer interaction, $\mathbf{n}$ is a real unit vector, and

$$
\begin{aligned}
\sigma_{\mathbf{n}}^a = \mathbf{n}\cdot\boldsymbol{\sigma}^a, \quad \boldsymbol{\sigma}^a = \big(\sigma_x^a, \sigma_y^a, \sigma_z^a\big), \quad \text{with} \\
\sigma_x^a = |0_a\rangle\langle 1_a| + |1_a\rangle\langle 0_a|, \\
\sigma_y^a = -i|0_a\rangle\langle 1_a| + i|1_a\rangle\langle 0_a|, \\
\sigma_z^a = |0_a\rangle\langle 0_a| - |1_a\rangle\langle 1_a|,
\end{aligned}
\tag{3.2}
$$

45

with $\sigma_{x,y,z}^b$ defined similarly. In the so-called weak measurement regime,[1] equation 3.1 is approximated as the lowest-order terms of its Taylor series expansion,

$$U(\epsilon) \approx \mathbb{1}_a \otimes \mathbb{1}_b - i\epsilon\sigma_{\mathbf{n}}^a \otimes \sigma_z^b + \mathcal{O}(\epsilon^2). \tag{3.3}$$

However, there exists a general closed-form formula for it, whose derivation, recently outlined by De Zela [153], we elaborate here. First, let us write the exponential map as a power series,

$$U(\epsilon) = \exp\left(-i\epsilon\sigma_{\mathbf{n}}^a \otimes \sigma_z^b\right) = \sum_{n=0}^{\infty} \frac{\left(-i\epsilon\sigma_{\mathbf{n}}^a \otimes \sigma_z^b\right)^n}{n!}. \tag{3.4}$$

We note that even powers of both spin operators are equal to the respective identity operators,

$$\left(\sigma_{\mathbf{n}}^a\right)^{2k} = \mathbb{1}_a, \quad \left(\sigma_z^b\right)^{2k} = \mathbb{1}_b, \quad \text{with} \quad k = 0, 1, \ldots, \tag{3.5}$$

and that odd powers result in the original operators,

$$\left(\sigma_{\mathbf{n}}^a\right)^{2k+1} = \sigma_{\mathbf{n}}^a, \quad \left(\sigma_z^b\right)^{2k+1} = \sigma_z^b, \quad \text{with} \quad k = 0, 1, \ldots, \tag{3.6}$$

so we can split the power series in equation 3.4 into a sum over even powers and a sum over odd powers,

$$U(\epsilon) = \sum_{k=0}^{\infty} \frac{(-i\epsilon)^{2k}}{(2k)!}\mathbb{1}_{ab} + \sum_{k=0}^{\infty} \frac{(-i\epsilon)^{2k+1}}{(2k+1)!}\sigma_{\mathbf{n}}^a \otimes \sigma_z^b. \tag{3.7}$$

Even and odd powers of the imaginary unit i satisfy

$$(-i)^{2k} = (-1)^k, \quad \text{and} \quad (-i)^{2k+1} = -i(-1)^k, \tag{3.8}$$

which means that equation 3.7 reduces to the desired formula,

$$U(\epsilon) = \left(\sum_{k=0}^{\infty} \frac{(-1)^k\epsilon^{2k}}{(2k)!}\right)\mathbb{1}_{ab} - i\left(\sum_{k=0}^{\infty} \frac{(-1)^k\epsilon^{2k+1}}{(2k+1)!}\right)\sigma_{\mathbf{n}}^a \otimes \sigma_z^b$$
$$= \cos\epsilon - i\sin\epsilon\,\sigma_{\mathbf{n}}^a\sigma_z^b, \tag{3.9}$$

where in the last line the bipartite identity is implicit in the first term and we have dropped the tensor product symbol. From the last step we can determine the domain of the strength parameter. The sine and cosine power series are valid for all real numbers. Since both functions have period 2π, we can restrict ϵ to the interval $[0, 2\pi]$, which allows

---

1. For a detailed example of a weak measurement, see, e.g., section 1 of the supporting material for [22].

us in particular to study weak values under strong measurements. As a prelude for our implementation proposals, we write out the b-space operators in equation 3.9, regroup the terms conveniently, and employ the alluded closed-form, single-qubit exponential formula to obtain:

$$
\begin{aligned}
U(\epsilon) &= \cos\epsilon(|0_b\rangle\langle 0_b| + |1_b\rangle\langle 1_b|) - i\sin\epsilon\,\sigma_{\mathbf{n}}^a(|0_b\rangle\langle 0_b| - |1_b\rangle\langle 1_b|) \\
&= (\cos\epsilon - i\sin\epsilon\,\sigma_{\mathbf{n}}^a)\,|0_b\rangle\langle 0_b| + (\cos\epsilon + i\sin\epsilon\,\sigma_{\mathbf{n}}^a)\,|1_b\rangle\langle 1_b| \\
&= \exp\left(-i\epsilon\sigma_{\mathbf{n}}^a\right)|0_b\rangle\langle 0_b| + \exp\left(i\epsilon\sigma_{\mathbf{n}}^a\right)|1_b\rangle\langle 1_b| \\
&\equiv U_a^\dagger(\mathbf{n},\epsilon)\Pi_{0_b} + U_a(\mathbf{n},\epsilon)\Pi_{1_b}.
\end{aligned}
\tag{3.10}
$$

Here, $U_a(\mathbf{n},\epsilon)$ and its Hermitian conjugate are unitary maps that act only on qubit a, whereas the projectors $\Pi_{0_b,1_b}$ act on qubit b.

To measure the weak value $\langle\sigma_{\mathbf{n}}^a\rangle_w$, we must first prepare the preselection (system) state $|A_i\rangle$; the pointer state $|B_i\rangle$ as, for instance, $|+_b\rangle \equiv 2^{-1/2}(|0_b\rangle + |1_b\rangle)$; and apply the evolution operator to the initial joint state:

$$
\begin{aligned}
U(\epsilon)|A_i\rangle|B_i\rangle &= \left(\cos\epsilon - i\sin\epsilon\,\sigma_{\mathbf{n}}^a\sigma_z^b\right)|A_i\rangle|+_b\rangle \\
&= \cos\epsilon|A_i\rangle|+_b\rangle - i\sin\epsilon\,\sigma_{\mathbf{n}}^a|A_i\rangle|-_b\rangle,
\end{aligned}
\tag{3.11}
$$

where $|-_b\rangle \equiv 2^{-1/2}(|0_b\rangle - |1_b\rangle)$. Then we project the evolved state onto the postselection state $|A_f\rangle$ coupled to an auxiliary pointer state, $|B_f\rangle$, and rewrite the resulting expression in terms of the weak value of interest:

$$
\begin{aligned}
\langle A_f|\langle B_f|U(\epsilon)|A_i\rangle|B_i\rangle &= \cos\epsilon\langle A_f|A_i\rangle\langle B_f|+_b\rangle - i\sin\epsilon\langle A_f|\sigma_{\mathbf{n}}^a|A_i\rangle\langle B_f|-_b\rangle \\
&= \langle A_f|A_i\rangle\left(\cos\epsilon\langle B_f|+_b\rangle - i\sin\epsilon\,\langle\sigma_{\mathbf{n}}^a\rangle_w\langle B_f|-_b\rangle\right).
\end{aligned}
\tag{3.12}
$$

Let us now write the weak value, a complex number, in its algebraic form,

$$
\langle\sigma_{\mathbf{n}}^a\rangle_w = R + iI,
\tag{3.13}
$$

and define the eigenvectors of σ_y^b as $|r_b\rangle \equiv 2^{-1/2}(|0_b\rangle + i|1_b\rangle)$, and $|l_b\rangle \equiv 2^{-1/2}(|0_b\rangle - i|1_b\rangle)$. By choosing six $|B_f\rangle$ appropriately, simplifying equation 3.12, and squaring its norm, we obtain the measurable quantities

$$
|B_f\rangle = |+_b\rangle \longrightarrow i_0 = |\langle A_f|A_i\rangle|^2\cos^2\epsilon,
\tag{3.14a}
$$

$$
|B_f\rangle = |-_b\rangle \longrightarrow i_1 = |\langle A_f|A_i\rangle|^2\sin^2\epsilon\,|\langle\sigma_{\mathbf{n}}^a\rangle_w|^2,
\tag{3.14b}
$$

$$|B_f\rangle = |0_b\rangle \longrightarrow i_2 = \frac{1}{2}|\langle A_f|A_i\rangle|^2 \left[(\cos\epsilon + I\sin\epsilon)^2 + R^2\sin^2\epsilon\right], \tag{3.14c}$$

$$|B_f\rangle = |1_b\rangle \longrightarrow i_3 = \frac{1}{2}|\langle A_f|A_i\rangle|^2 \left[(\cos\epsilon - I\sin\epsilon)^2 + R^2\sin^2\epsilon\right], \tag{3.14d}$$

$$|B_f\rangle = |r_b\rangle \longrightarrow i_4 = \frac{1}{2}|\langle A_f|A_i\rangle|^2 \left[(\cos\epsilon + R\sin\epsilon)^2 + I^2\sin^2\epsilon\right], \tag{3.14e}$$

$$|B_f\rangle = |l_b\rangle \longrightarrow i_5 = \frac{1}{2}|\langle A_f|A_i\rangle|^2 \left[(\cos\epsilon - R\sin\epsilon)^2 + I^2\sin^2\epsilon\right], \tag{3.14f}$$

which we call intensities regardless of their physical meaning as light intensities, photon coincidence counts, etc. By subtracting equations 3.14d and 3.14f from equations 3.14c and 3.14e, respectively, we obtain

$$i_2 - i_3 = I|\langle A_f|A_i\rangle|^2 \sin 2\epsilon, \tag{3.15a}$$

$$i_4 - i_5 = R|\langle A_f|A_i\rangle|^2 \sin 2\epsilon. \tag{3.15b}$$

When it is feasible to solve equations 3.14a, 3.14b, 3.15a, and 3.15b for the squared magnitude, real part, and imaginary part[2] of $\langle\sigma_{\mathbf{n}}^a\rangle_w$ (i.e., when the pre- and postselection states are not orthogonal and $\sin 2\epsilon \neq 0$), we find that

$$|\langle\sigma_{\mathbf{n}}^a\rangle_w|^2 = \frac{i_1}{i_0}\cot^2\epsilon, \tag{3.16a}$$

$$R = \frac{i_4 - i_5}{2\,i_0}\cot\epsilon, \tag{3.16b}$$

$$I = \frac{i_2 - i_3}{2\,i_0}\cot\epsilon. \tag{3.16c}$$

These equations complete the prescription for determining weak values from measurements of almost arbitrary strength. The model is periodic in ϵ with period π, so we will further restrict our analysis to the interval $]0, \pi[$. Evidently, the model breaks down when $\epsilon = 0, \pi/2$, and π. We will see in section 3.3 what consequences these divergences have for the overall reconstructed weak values.

3.2 Implementation Proposals

3.2.1 All-Optical Setting

The foregoing proposal can be implemented in an all-optical setup that works with either laser light or individual photons. This section explains how to carry out each stage–

---

2. Although equation 3.16a might seem redundant in the face of equations 3.16b and 3.16c, it is much more practical for certain ends to use it to compute the weak value's squared magnitude as a function of just two intensities, instead of five.

preselection, evolution, postselection, and measurement–in an arrangement recently put forward by De Zela [154], which consists of three interferometers, of the type shown in figure 3.1, in series. These interferometric setups, originally proposed by Englert *et al.* [155], can each realize arbitrary, polarization-path unitary operations by using appropriately-placed phase shifters, quarter-, and half-wave plates.[3]
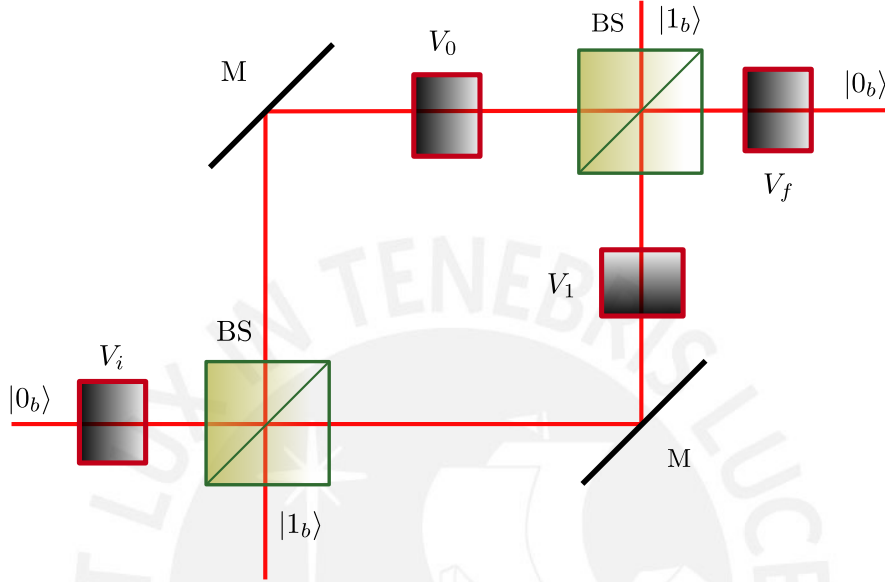

Figure 3.1: Interferometric setup proposed by Englert *et al.* [155] that performs arbitrary, two-qubit unitary transformations. Starting from the bottom left of the device, light travels through either the horizontal ($|0_b\rangle$) or vertical ($|1_b\rangle$) path, or both, and is acted on by specific unitary operators $V_{i,f,0,1}$, 50:50 beam splitters (BS), and mirrors (M). After it exits the second BS and undergoes V_f, the desired two-qubit map is achieved. $V_{i,f,0,1}$ can be implemented by at most one phase shifter and three wave plates.

In such an experimental setting, qubit a represents the polarization of light, with $|0_a\rangle$ ($|1_a\rangle$) the state of horizontal (vertical) polarization, whereas qubit b is the propagation path, so that $|0_b\rangle$ ($|1_b\rangle$) stands for the horizontal (vertical) path. A linearly-polarized state that propagates along a straight line usually plays the role of the initial state in optical experiments. We will assume it to be $|0_a\rangle|0_b\rangle$, so that it enters the preselection stage from the lower left port of figure 3.1. In general, the effect of such an array is described by

$$U_{\mathrm{MZ}} = (V_f \Pi_{0_b} + \Pi_{1_b})\, U_{\mathrm{BS}}\, (V_0 \Pi_{0_b} + V_1 \Pi_{1_b})\, U_{\mathrm{M}}\, U_{\mathrm{BS}}\, (V_i \Pi_{0_b} + \Pi_{1_b}), \qquad (3.17)$$

---

3. The three-interferometer device is presented for illustrative purposes only. Much simpler settings could certainly be devised that accomplish the same objective.

where

$$U_{\mathrm{BS}} = \frac{1}{\sqrt{2}} \left(\mathbb{1}_b + i\sigma_x^b \right), \tag{3.18a}$$

$$U_{\mathrm{M}} = -i\sigma_x^b \tag{3.18b}$$

represent the beam splitter and mirror operators, respectively, and $V_{i,f,0,1}$ are $U(2)$ transformations in the space of qubit a. For concreteness, let us say that we wish to prepare the state

$$|A_i\rangle|B_i\rangle = (\cos(\alpha_i/2)|0_a\rangle + \sin(\alpha_i/2)|1_a\rangle) \, |+_b\rangle, \tag{3.19}$$

for which we use the device in figure 3.1 with

$$V_0 = V_f = \mathbb{1}_a, \quad V_i = U_{\mathrm{H}}(\alpha_i/4), \quad V_1 = i\mathbb{1}_a, \tag{3.20}$$

where $U_{\mathrm{H}}(\beta)$ is given by equation 2.2b with the substitutions $|h\rangle \to |0_a\rangle$ and $|v\rangle \to |1_a\rangle$. The identity operators in equation 3.20 are trivially realized by not inserting any element in their respective locations, V_i by setting a half-wave plate with its fast axis at an angle $\alpha_i/4$, and V_1 by placing a phase shifter that introduces an $e^{i\pi/2}$ phase shift in the vertical with respect to the horizontal path.

Upon exiting the first interferometer, a mirror is placed in each path, which by virtue of equation 3.18b accords the state $|A_i\rangle|B_i\rangle$ only a global phase. Thereafter, both paths meet at and recombine in a second arrangement of the type shown in figure 3.1. Whereas the first procedure hinged on the choice of preselection state, the evolution stage depends only on the unit vector $\mathbf{n}$ and the coupling parameter ϵ, as indicated by equation 3.10. Direct comparison of this expression with equations (17) and (18) of [155] reveals that the unitaries in this case are given by

$$V_i = V_f = U_a^\dagger(\mathbf{n}, \epsilon), \quad V_0 = V_1 = U_a(\mathbf{n}, \epsilon). \tag{3.21}$$

Such operators can be implemented as products of two quarter-wave plates and one half-wave plate [156], which in general requires us to shift the angles of all plates for each different ϵ. Since we aim to study how the measurement strength affects the results' precision and accuracy, we would benefit from employing a sequence of plates that, for fixed $\mathbf{n}$, demands a minimal number of plates to be shifted. The solution to this conundrum was found by Bhandari and Dasgupta [157]: for the unit vector $\mathbf{n} =$

$(\sin\vartheta\cos\varphi, \sin\vartheta\sin\varphi, \cos\vartheta)$, the transformation $U_a(\mathbf{n}, \epsilon)$ and its adjoint are

$$U_a(\mathbf{n}, \epsilon) = U_Q\left(\frac{\pi+\varphi}{2}\right) U_Q\left(\frac{\vartheta+\varphi}{2}\right) U_H\left(\frac{-\pi+\vartheta+\varphi}{2} + \frac{\epsilon}{2}\right) U_Q\left(\frac{\vartheta+\varphi}{2}\right) U_Q\left(\frac{\varphi}{2}\right),$$
(3.22a)

$$U_a^\dagger(\mathbf{n}, \epsilon) = U_Q\left(\frac{\pi+\varphi}{2}\right) U_Q\left(\frac{\vartheta+\varphi+\pi}{2}\right) U_H\left(\frac{\vartheta+\varphi}{2} + \frac{\epsilon}{2}\right) U_Q\left(\frac{\vartheta+\varphi+\pi}{2}\right) U_Q\left(\frac{2\pi+\varphi}{2}\right),$$
(3.22b)

with $U_Q(\alpha)$ given by equation 2.2a. If we place these unitaries as prescribed in equations 3.21, we obtain the evolved state of equation 3.11.

Subsequently, the state $U(\epsilon)|A_i\rangle|B_i\rangle$ encounters two mirrors and acquires a relative positive sign between its terms (see equation 3.11). As a consequence, the roles of i_2 and i_3 in equations 3.14 alternate, as do those of i_4 and i_5. Because such a change is immaterial to our present ends, we will pay it no heed. The postselection and measurement stage necessitates three different versions of the setup in figure 3.1. Let us choose, for simplicity and concreteness, the postselection state

$$|A_f\rangle = |0_a\rangle.$$
(3.23)

Experimentally, a projection onto the above state is achieved by measuring the horizontal polarization of a beam. As shown in equations 3.14, we also need to project onto six different path states. By the nature of qubit b, it is only feasible to project onto states $|0_b\rangle$ and $|1_b\rangle$, i.e., to carry out measurements in the horizontal or vertical path. We must, therefore, employ our device to realize operations such that

$$\langle A_f|\langle 0_b|U_{MZ} = \langle A_f|\langle +_b|, \quad \langle A_f|\langle 1_b|U_{MZ} = \langle A_f|\langle -_b|$$
(3.24)

(cf. equations 3.12, 3.14a, and 3.14b), in order to measure $i_{0,1}$, and similar expressions for the other $|B_f\rangle$ states in equations 3.14c−3.14f. It can be easily shown that

$$U_{MZ} = \mathbb{1}_a \otimes H,$$
(3.25)

satisfies equation 3.24, with H being the Hadamard transformation

$$H = \frac{1}{\sqrt{2}}\left(|0_b\rangle\langle 0_b| + |0_b\rangle\langle 1_b| + |1_b\rangle\langle 0_b| - |1_b\rangle\langle 1_b|\right) = |+_b\rangle\langle 0_b| + |-_b\rangle\langle 1_b|,$$
(3.26)

which is called Hadamard gate in the context of quantum computation. The two-qubit operator of equation 3.25, in accordance to the algorithm described in [155], is implemented by setting

$$V_i = -\mathbb{1}_a, \quad V_f = \mathbb{1}_a, \quad V_0 = e^{i3\pi/4}\mathbb{1}_a, \quad V_1 = e^{-i3\pi/4}\mathbb{1}_a.$$
(3.27)

Again, the phases in these expressions result from the action of phase shifters placed in the corresponding locations. Intensities $i_{2,3}$ from equations 3.14c and 3.14d can be trivially obtained with

$$V_i = V_f = V_0 = V_1 = \mathbb{1}_a, \tag{3.28}$$

followed by measurements of the horizontal polarization on each path.[4] A two-qubit mapping such that

$$\langle A_f|\langle 0_b|U_{\mathrm{MZ}} = \langle A_f|\langle r_b|, \quad \langle A_f|\langle 1_b|U_{\mathrm{MZ}} = \langle A_f|\langle l_b|, \tag{3.29}$$

which produces $i_{4,5}$ (see equations 3.14e and 3.14f), is given by

$$U_{\mathrm{MZ}} = \mathbb{1}_a \otimes H\, S^\dagger. \tag{3.30}$$

Here, the operator

$$S^\dagger = |0_b\rangle\langle 0_b| + e^{-i\pi/2}|1_b\rangle\langle 1_b| = |0_b\rangle\langle 0_b| - i|1_b\rangle\langle 1_b|. \tag{3.31}$$

introduces a $-\pi/2$ phase shift between the states $|0_b\rangle$ and $|1_b\rangle$. Equation 3.30 results from employing Englert *et al.*'s arrangement with the unitaries

$$V_i = -i\mathbb{1}_a, \quad V_f = \mathbb{1}_a, \quad V_0 = e^{i\pi/4}\mathbb{1}_a, \quad V_1 = e^{i3\pi/4}\mathbb{1}_a. \tag{3.32}$$

Finally, we place a horizontally aligned polarizer and either a powermeter or a single photon counter in each path, and thereby measure the intensities $i_{0,\dots,5}$.

3.2.2 Quantum Computational Setting

To implement the proposal in a quantum computer, we must first select a particular axis of rotation for the Pauli spin operator. If we take, for instance, $\mathbf{n} = (-\sin\phi, \cos\phi, 0)$, with ϕ ranging by convention from $-\pi$ to π, we find that the $\exp(\pm i\epsilon\sigma^a_{\mathbf{n}})$ terms in equation 3.10 can be decomposed into the following products of rotation gates:

$$\begin{aligned}
\exp(\pm i\epsilon\sigma^a_{\mathbf{n}}) &= \cos\epsilon \pm i\sin\epsilon\left(-\sin\phi\,\sigma^a_x + \cos\phi\,\sigma^a_y\right) \\
&= \exp(-i\phi\,\sigma^a_z/2)\exp(\pm i\epsilon\sigma^a_y)\exp(i\phi\,\sigma^a_z/2) \\
&\equiv R_z(\phi)R_y(\mp 2\epsilon)R_z(-\phi),
\end{aligned} \tag{3.33}$$

---

4. Alternatively, these intensities can be obtained without the third interferometer by simply measuring on both paths after the evolution stage.

where to go from the first to the second line we have used the equivalence between the closed form of an $SU(2)$ operator's exponential map and its Euler angle form. How the quantum circuit functions can be clarified with the diagram shown in figure 3.2. Starting at the left from the joint state $|0_a\rangle|0_b\rangle$, we prepare the system's preselection state via a rotation,

$$|A_i\rangle = R_y(\alpha_i)|0_a\rangle = \exp\left(-i\alpha_i\sigma_y^a/2\right)|0_a\rangle = \cos(\alpha_i/2)|0_a\rangle + \sin(\alpha_i/2)|1_a\rangle, \qquad (3.34)$$

and the auxiliary state $|B_i\rangle = |+_b\rangle = H|0_b\rangle$ with a Hadamard gate (see equation 3.26). So as to reduce decoherence effects, $U(\epsilon)$ in equation 3.10 must be expressed with as few gates as possible – especially two-qubit gates – for which we write out the exponentials as in equation 3.33 and appropriately factor out the rotation gates:

$$
\begin{aligned}
U(\epsilon) &= R_z(\phi)R_y(2\epsilon)R_z(-\phi) \otimes \Pi_{0_b} + R_z(\phi)R_y(-2\epsilon)R_z(-\phi) \otimes \Pi_{1_b} \\
&= R_z(\phi)\left[R_y(2\epsilon)\Pi_{0_b} + R_y(-2\epsilon)\Pi_{1_b}\right]R_z(-\phi) \\
&= R_z(\phi)R_y(2\epsilon)\left[\Pi_{0_b} + R_y(-4\epsilon)\Pi_{1_b}\right]R_z(-\phi) \\
&= R_z(\phi)R_y(2\epsilon)\mathrm{C}R_y(-4\epsilon)R_z(-\phi). \qquad (3.35)
\end{aligned}
$$

Here, $\mathrm{C}R_y(\vartheta) \equiv \Pi_{0_b} + R_y(\vartheta)\Pi_{1_b}$ represents the controlled R_y gate, in which the state of qubit b controlls how qubit a is acted upon. The evolution operator in equation 3.35 works as follows: qubit a is subjected to $R_z(-\phi)$; if qubit b is in the state $|0_b\rangle$, a is then subjected to $R_y(2\epsilon)$, or otherwise to $R_y(-4\epsilon)$ followed by $R_y(2\epsilon)$; finally, $R_z(\phi)$ acts on a, which completes the evolution. For the last stage, we choose the postselection state $|A_f\rangle = |0_a\rangle$ and consider three different circuits, each characterized by a specific gate G (see figure 3.2). As in section 3.2.1, to measure the observables $i_{0,1}$ of equations 3.14a and 3.14b, we apply another Hadamard gate to qubit b (i.e., $\mathrm{G} = H$; cf. equation 3.25), and then project onto $\langle 0_a|\langle 0_b|$ and $\langle 0_a|\langle 1_b|$, respectively. Intensities $i_{2,3}$ require setting G equal to the identity (cf. equation 3.28), and projecting onto the same respective states. Finally, we use $\mathrm{G} = H\,S^\dagger$ (cf. equation 3.30), with the $S^\dagger$ gate given in equation 3.31, project again onto $\langle 0_a|\langle 0_b|$ and $\langle 0_a|\langle 1_b|$, and thereby obtain $i_{4,5}$. The required pre-measurement gates G for qubit b are summarized in table 3.1.
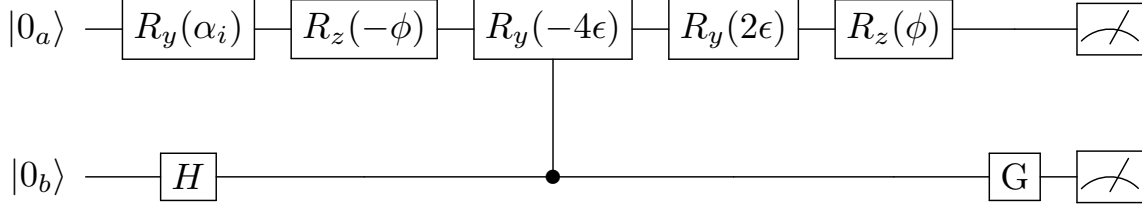
Figure 3.2: Quantum circuit for measuring weak values $\langle\sigma_{\mathbf{n}}^a\rangle_w$ and preselection state parameters with interaction strength ϵ. It prepares the initial state, acts $U(\epsilon)$ on it, and measures $i_{0,\dots,5}$ with the different gates G indicated in table 3.1.

Gate G	Observables
—H—	$i_{0,1}$
————	$i_{2,3}$
—$S^\dagger$—H—	$i_{4,5}$

Table 3.1: Gates G for measuring the respective intensities.

As explained in section 1.3, an important application of weak values is the measurement of quantum states. Despite the fact that such a procedure has traditionally been restricted to weak measurements [42, 87], it is possible, as demonstrated in [45], to implement it without need for the weakness hypothesis. Naturally, we can also carry out such a protocol with the same setup and outcomes described in this chapter. To this end, let us first note that, in general, any Pauli spin operator has two eigenvectors,

$$\sigma_{\mathbf{n}}^a|\mathbf{n}_\pm\rangle = \pm|\mathbf{n}_\pm\rangle, \tag{3.36}$$

which form the basis $\{|\mathbf{n}_+\rangle, |\mathbf{n}_-\rangle\}$ for qubit a and generate the eigenprojectors

$$\Pi_\pm^a = |\mathbf{n}_\pm\rangle\langle\mathbf{n}_\pm| = \frac{1}{2}(1 \pm \sigma_{\mathbf{n}}^a). \tag{3.37}$$

For the chosen pre- and postselection states, the theoretical weak value takes the form

$$\langle\sigma_{\mathbf{n}}^a\rangle_w = -\tan(\alpha_i/2)\left(\sin\phi + i\cos\phi\right) = -ie^{-i\phi}\tan\left(\alpha_i/2\right). \tag{3.38}$$

In what follows it will be convenient to distinguish between theoretical values and experimental mean values. Hence, let us denote the real and imaginary parts of equation 3.38 as

$$R_t = -\tan(\alpha_i/2)\sin\phi, \quad \text{and} \quad I_t = -\tan(\alpha_i/2)\cos\phi. \tag{3.39}$$

For the case that concerns us, the eigenvectors of $\sigma_{\mathbf{n}}^a$ are given by

$$|\mathbf{n}_\pm\rangle = \frac{1}{\sqrt{2}}\big(\pm|0_a\rangle + ie^{i\phi}|1_a\rangle\big), \tag{3.40}$$

and the weak values of the eigenprojectors in equation 3.37 by

$$\langle\Pi_\pm^a\rangle_w = \frac{1}{2}(1 \pm \langle\sigma_{\mathbf{n}}^a\rangle_w) = \frac{1}{2}\big(1 \mp ie^{-i\phi}\tan(\alpha_i/2)\big). \tag{3.41}$$

From the inner products between equations 3.40 and 3.34 we find that the components of the preselection state in the basis of the spin operator are

$$\langle\mathbf{n}_\pm|A_i\rangle = \pm\frac{1}{\sqrt{2}}\big(\cos(\alpha_i/2) \mp ie^{-i\phi}\sin(\alpha_i/2)\big). \tag{3.42}$$

The strong resemblance between equations 3.41 and 3.42 hints at a deeper connection. As Lundeen *et al.* showed, the preselection state can be written as a linear combination with coefficients proportional to the eigenprojectors' weak values[5] if we consider a postselection state such that the basis to which it belongs and the basis of $\sigma_{\mathbf{n}}^a$ are *mutually unbiased bases*.[6] In our case, $|A_f\rangle = |0_a\rangle$ forms, together with $|1_a\rangle$, the computational basis of qubit a, which is unbiased with respect to $\{|\mathbf{n}_+\rangle, |\mathbf{n}_-\rangle\}$:

$$|\langle 0_a|\mathbf{n}_+\rangle|^2 = |\langle 0_a|\mathbf{n}_-\rangle|^2 = |\langle 1_a|\mathbf{n}_+\rangle|^2 = |\langle 1_a|\mathbf{n}_-\rangle|^2 = 1/2. \tag{3.43}$$

The exact expression for $|A_i\rangle$ depends, furthermore, on the choice of $|A_f\rangle$. The overlaps of our postselection state with the eigenstates of $\sigma_{\mathbf{n}}^a$ are

$$\langle A_f|\mathbf{n}_\pm\rangle = \pm 1/\sqrt{2}. \tag{3.44}$$

Armed with equations 3.41, 3.42, and 3.44, as well as with the normalization condition, we can now write the desired formula for $|A_i\rangle$. Had both overlaps been positive,[7] we could have expressed the preselection state as in equation (8) of [45]. Since one of them is negative, our expression has a relative minus sign:

$$|A_i\rangle = \frac{\langle\Pi_+^a\rangle_w|\mathbf{n}_+\rangle - \langle\Pi_-^a\rangle_w|\mathbf{n}_-\rangle}{\sqrt{\big|\langle\Pi_+^a\rangle_w\big|^2 + \big|\langle\Pi_-^a\rangle_w\big|^2}}, \tag{3.45}$$

---

5. See equations (6) and (7) of [87], as well as the discussion on complementarity in the supplementary information document of the same article.

6. Two bases $\{|a_i\rangle\}$ and $\{|b_j\rangle\}$, with $i, j = 1, \ldots, d$, are said to be mutually unbiased if $|\langle a_i|b_j\rangle|^2 = 1/d$, for all i, j.

7. This can be achieved by choosing $|A_f\rangle = |1_a\rangle = 2^{-1/2}e^{-i(\phi+\pi/2)}(|\mathbf{n}_+\rangle + |\mathbf{n}_-\rangle)$, which is the "diagonal" state of $\sigma_{\mathbf{n}}^a$, up to a global phase. As a rule, there exists only one state in the basis of $|A_f\rangle$ for which all the overlaps are positive [158].

which, in our case, becomes

$$|A_i\rangle = \frac{1}{\sqrt{2}}\big(\cos(\alpha_i/2) - ie^{-i\phi}\sin(\alpha_i/2)\big)|\mathbf{n}_+\rangle - \frac{1}{\sqrt{2}}\big(\cos(\alpha_i/2) + ie^{-i\phi}\sin(\alpha_i/2)\big)|\mathbf{n}_-\rangle.$$
(3.46)

Following Denkmayr *et al.* [45], we define the normalization factor

$$\nu \equiv \left(\left|\langle\Pi_+^a\rangle_w\right|^2 + \left|\langle\Pi_-^a\rangle_w\right|^2\right)^{-1/2}$$
$$= \left(\frac{1}{2} + \frac{1}{2}\left|\langle\sigma_\mathbf{n}^a\rangle_w\right|^2\right)^{-1/2}.$$
(3.47)

Finally, we characterize the preselection state given by equation 3.45 in terms of equations 3.41 and 3.47 by combining the measured intensities (equations 3.14) as

$$\nu = \left(\frac{1}{2} + \frac{1}{2}\frac{i_1}{i_0}\cot^2\epsilon\right)^{-1/2},$$
(3.48a)

$$\alpha = 2\arctan\sqrt{\frac{i_1}{i_0}\cot^2\epsilon}\,,$$
(3.48b)

$$\phi = \arctan\left(\frac{i_4 - i_5}{i_2 - i_3}\right).$$
(3.48c)

Equations 3.16 and 3.48 complete our proposal for weak value characterization and direct state measurement. We employed them with our measured data to obtain the results that follow.

3.3 Results

As mentioned in section 1.4, our proposal was realized in the ibm_oslo backend. Figure 3.2 and table 3.1 imply that a complete set of intensities requires running 3 different circuits–one for each pair. For each circuit, at every sampled value of ϵ and ϕ, we ran 20 experiments with 2000 shots. These computations produced the intensities $i_{0,\dots,5}$. We averaged them and compounded their mean values in accordance to equations 3.16 and 3.48 to get the weak values of $\sigma_\mathbf{n}^a$ and the parameters of $|A_i\rangle$. As we did in equations 3.39, we denote the theoretical intensities as $i_{0t}, \dots, i_{5t}$; these will be given by equations 3.14 with the substitutions $|\langle A_f|A_i\rangle|^2 \to \cos^2(\alpha_i/2)$, $I \to I_t$, and $R \to R_t$. Likewise, we will write R_m and I_m for the measured real and imaginary parts of $\langle\sigma_\mathbf{n}^a\rangle_w$.

Concomitant to the average observables are their respective standard deviations, $\sigma_{i_0}, \dots, \sigma_{i_5}$. The statistical uncertainties in R_m and I_m stem from fluctuations in the

measured counts of $i_{0,\ldots,5}$, so they can be estimated with the multi-variable propagation formula as[8]

$$\sigma_R = \sqrt{\left(\frac{\partial R}{\partial i_0}\right)^2 \sigma_{i_0}^2 + \left(\frac{\partial R}{\partial i_4}\right)^2 \sigma_{i_4}^2 + \left(\frac{\partial R}{\partial i_5}\right)^2 \sigma_{i_5}^2}$$

$$= \frac{1}{\cos^2(\alpha_i/2)} \sqrt{\left(\frac{i_{4t} - i_{5t}}{i_{0t}}\right)^2 \frac{\sigma_{i_0}^2}{\sin^2 2\epsilon} + \frac{\sigma_{i_4}^2 + \sigma_{i_5}^2}{\sin^2 2\epsilon}}$$

$$= \frac{1}{\cos^2(\alpha_i/2)} \sqrt{\frac{\tan^2(\alpha_i/2) \sin^2\phi}{\cos^4\epsilon} \sigma_{i_0}^2 + \frac{\sigma_{i_4}^2 + \sigma_{i_5}^2}{\sin^2 2\epsilon}}, \tag{3.49a}$$

$$\sigma_I = \sqrt{\left(\frac{\partial I}{\partial i_0}\right)^2 \sigma_{i_0}^2 + \left(\frac{\partial I}{\partial i_2}\right)^2 \sigma_{i_2}^2 + \left(\frac{\partial I}{\partial i_3}\right)^2 \sigma_{i_3}^2}$$

$$= \frac{1}{\cos^2(\alpha_i/2)} \sqrt{\left(\frac{i_{2t} - i_{3t}}{i_{0t}}\right)^2 \frac{\sigma_{i_0}^2}{\sin^2 2\epsilon} + \frac{\sigma_{i_2}^2 + \sigma_{i_3}^2}{\sin^2 2\epsilon}}$$

$$= \frac{1}{\cos^2(\alpha_i/2)} \sqrt{\frac{\tan^2(\alpha_i/2) \cos^2\phi}{\cos^4\epsilon} \sigma_{i_0}^2 + \frac{\sigma_{i_2}^2 + \sigma_{i_3}^2}{\sin^2 2\epsilon}}. \tag{3.49b}$$

The derivatives in the above expressions are calculated from equations 3.16 and then evaluated at the theoretical intensities. The uncertainties in the parameters given by equations 3.48 are computed in a similar manner:

$$\sigma_\nu = \sqrt{\left(\frac{\partial \nu}{\partial i_0}\right)^2 \sigma_{i_0}^2 + \left(\frac{\partial \nu}{\partial i_1}\right)^2 \sigma_{i_1}^2}$$

$$= \sqrt{\frac{2\sin^6(\alpha_i/2) \csc^2\alpha_i}{\cos^4\epsilon} \sigma_{i_0}^2 + \frac{\cos^2(\alpha_i/2)}{2\sin^4\epsilon} \sigma_{i_1}^2}, \tag{3.50a}$$

$$\sigma_\alpha = \sqrt{\left(\frac{\partial \alpha}{\partial i_0}\right)^2 \sigma_{i_0}^2 + \left(\frac{\partial \alpha}{\partial i_1}\right)^2 \sigma_{i_1}^2}$$

$$= \sqrt{\frac{\tan^2(\alpha_i/2)}{\cos^4\epsilon} \sigma_{i_0}^2 + \frac{\cot^2(\alpha_i/2)}{\sin^4\epsilon} \sigma_{i_1}^2}, \tag{3.50b}$$

$$\sigma_\phi = \sqrt{\sum_{j=2}^{5} \left(\frac{\partial \phi}{\partial i_j}\right)^2 \sigma_{i_j}^2}$$

$$= 2\left|\frac{\csc\alpha_i}{\sin 2\epsilon}\right| \sqrt{2\sin^2\phi \left(\sigma_{i_2}^2 + \sigma_{i_3}^2\right) + 2\cos^2\phi \left(\sigma_{i_4}^2 + \sigma_{i_5}^2\right)}. \tag{3.50c}$$

We carried out our experiments for 23 different couplings. $N = 9$ samples of ϕ from $-\pi$ to π were taken at each ϵ, and α_i was set to $\pi/4$. Like Vallone and Dequal [94] as well as Denkmayr *et al.* [45], we analyzed the precision and accuracy (as defined in section 1.3) of our results, for which we now introduce the following notation for

---

8. See, e.g., section 4.2 of [159] for more details on this approach to error propagation.

theoretical parameters. Let μ be a placeholder for R, I, ν, α, or ϕ. Then, $\mu_{t,j}$ will either refer to equations 3.39 evaluated at ϕ_j, or be given by

$$\nu_{t,j} = \sqrt{2}\cos(\alpha_i/2), \tag{3.51a}$$

$$\alpha_{t,j} = \pi/4, \tag{3.51b}$$

$$\phi_{t,j} \in \{-\pi, -3\pi/4, \ldots, 3\pi/4, \pi\}. \tag{3.51c}$$

Parameter μ's uncertainty for $\phi = \phi_{t,j}$, denoted as $\sigma_{\mu,j}$, is calculated from equations 3.49 or 3.50, whereas $\mu_{m,j}$ represents its respective mean value. With this notation in mind, we define

$$\bar{\sigma}_\mu \equiv \sqrt{\frac{1}{N}\sum_j^N \sigma_{\mu,j}^2}, \tag{3.52a}$$

$$\bar{\Delta}_\mu \equiv \sqrt{\frac{1}{N}\sum_j^N \left(\mu_{t,j} - \mu_{m,j}\right)^2} \tag{3.52b}$$

to be our measures of statistical uncertainty and systematic errors, respectively, at a fixed strength ϵ. Being the root mean square value of the sample uncertainties, $\bar{\sigma}_\mu$ quantifies the average fluctuations in the N samples, and stands thus as a proxy for precision. $\bar{\Delta}_\mu$, similarly, is the root mean square value of the difference between the theoretical parameter and its experimental mean value. Unlike Vallone and Dequal, we did not assess the accuracy of our outcomes by using the trace distance as a metric for errors. Still, $\bar{\Delta}_\mu$ puts a similar figure on systematic errors because it accounts for incongruities between theoretical and experimental values.

Our experimental results are illustrated in figures 3.3–3.10. The reconstructed real and imaginary parts of $\langle\sigma_{\mathbf{n}}^a\rangle_w$ (blue circles and red squares, respectively) are shown in figure 3.3 alongside their theoretical counterparts (blue solid lines and red dashed lines), for twelve different couplings. Going from left to right and from the top down, we observe that, in the weak measurement regime (exemplified by $\epsilon = 0.02$), both R_m and I_m deviate considerably from R_t and I_t, and that the fluctuations in the outcomes are large. Such a behavior is to be expected: after all, both quantities originate from the subtraction of two very close numbers (see equations 3.14c–3.14f), which are then divided by a small number, $\sin 2\epsilon$ (equations 3.15a and 3.15b). As ϵ increases, the error bars decrease in size, and the mean values comport better to the curves (see $\epsilon = 0.1 \to 1.2$). However, at larger strengths, the discrepancies between experimental
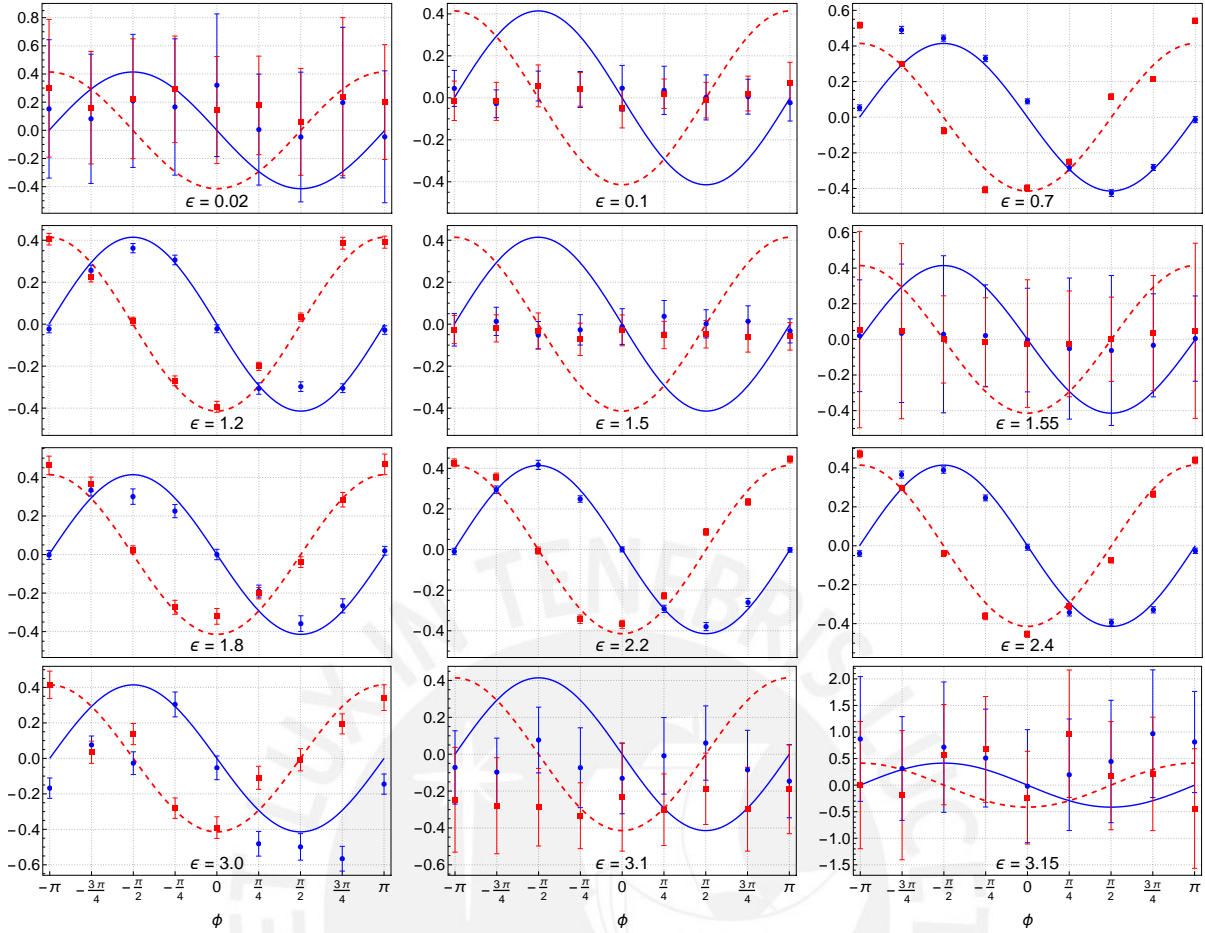
Figure 3.3: Real and imaginary parts of the weak values $\langle \sigma_{\mathbf{n}}^a \rangle_w$ as functions of ϕ, with $\alpha_i = \pi/4$, for different measurement strengths ϵ. Solid blue lines (circles) represent the theoretical (experimental) real part of the weak value, R_t (R_m). Dashed red lines (squares) indicate the theoretical (experimental) imaginary part of said weak value, I_t (I_m). Error bars stand for either σ_R or σ_I, which are given by equations 3.49.

and theoretical values as well as the fluctuations in the results begin to grow until they reach a maximum around $\epsilon = \pi/2$ (see $\epsilon = 1.5, 1.55$); afterwards, they subside again when the coupling increases up to $3\pi/4$ (see $\epsilon = 1.8 \to 2.4$), at which point, approximately, the trend reverses and both attain a new maximum as ϵ approaches π (see $\epsilon = 3.0 \to 3.15$). Evidently, certain strong measurements yield reconstructed weak values with comparable precision and accuracy to those of weak measurements.

Figure 3.3 has helped us describe qualitatively how our results depend on the interaction strength. For a quantitative assessment thereof, we turn to our metrics of statistical uncertainties and systematic errors, $\bar{\sigma}$ and $\bar{\Delta}$. As shown in figure 3.4, in the weak regime, $\bar{\sigma}_R$ and $\bar{\sigma}_I$ have relatively high values, which decrease as ϵ nears $\pi/4$ and then increase
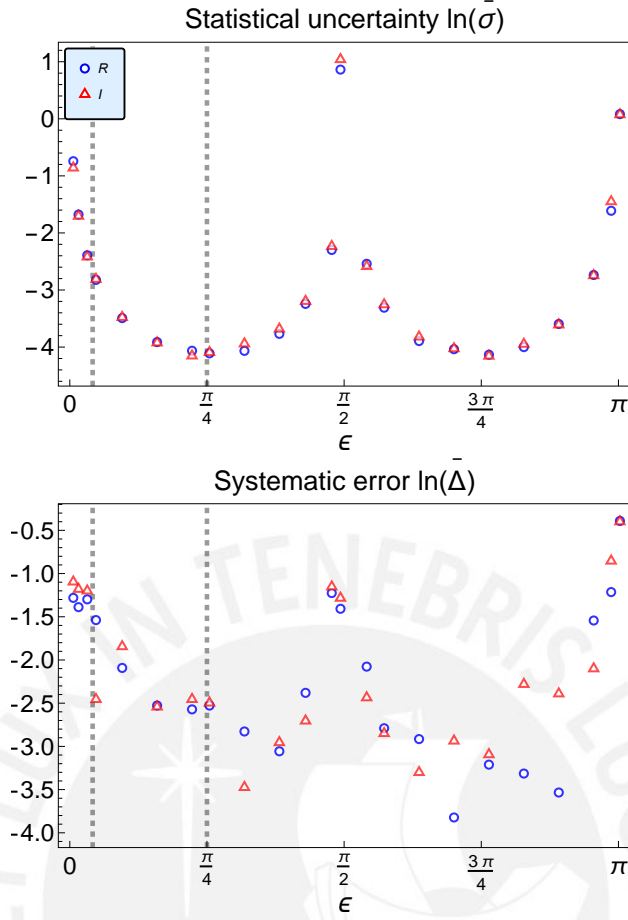
Figure 3.4: Logarithmic plot of the statistical uncertainties and systematic errors (see equations 3.52) of the real (R) and imaginary (I) parts of the weak value $\langle\sigma_{\mathbf{n}}^a\rangle_w$, as functions of the measurement strength parameter ϵ. The vertical dashed lines represent $\epsilon = \pi/24$ and $\epsilon = \pi/4$.

as it grows up to $\pi/2$; there, $\bar{\sigma}_{R,I}$ reach an apparent absolute maximum. For values of ϵ up to around $3\pi/4$, $\bar{\sigma}_{R,I}$ drop to a minimum, and then rise to the last maximum. Figure 3.4 shows a similar behavior across the domain of ϵ for $\bar{\Delta}_{R,I}$, as anticipated in the preceding paragraph. Systematic errors attain clear maxima near $\epsilon = 0, \pi/2$, and π: equations 3.16b and 3.16c diverge at those values, so the reconstructed R_m and I_m differ largely from R_t and I_t. In contrast, the locations of the minima of $\bar{\Delta}_{R,I}$ are not evident. Both plots in figure 3.4 depict vertical dashed lines at $\epsilon = \pi/24$ and $\pi/4$, the two values studied by Denkmayr *et al.* [45].[9] By comparing precision and accuracy in those cases, we come to the same conclusion as these authors: the strong measurement performs much better than the weak one. Nonetheless, our overall results reveal that

---

9. In their notation, these interaction strengths were denoted as $\alpha = \pi/12$ and $\pi/2$, respectively.
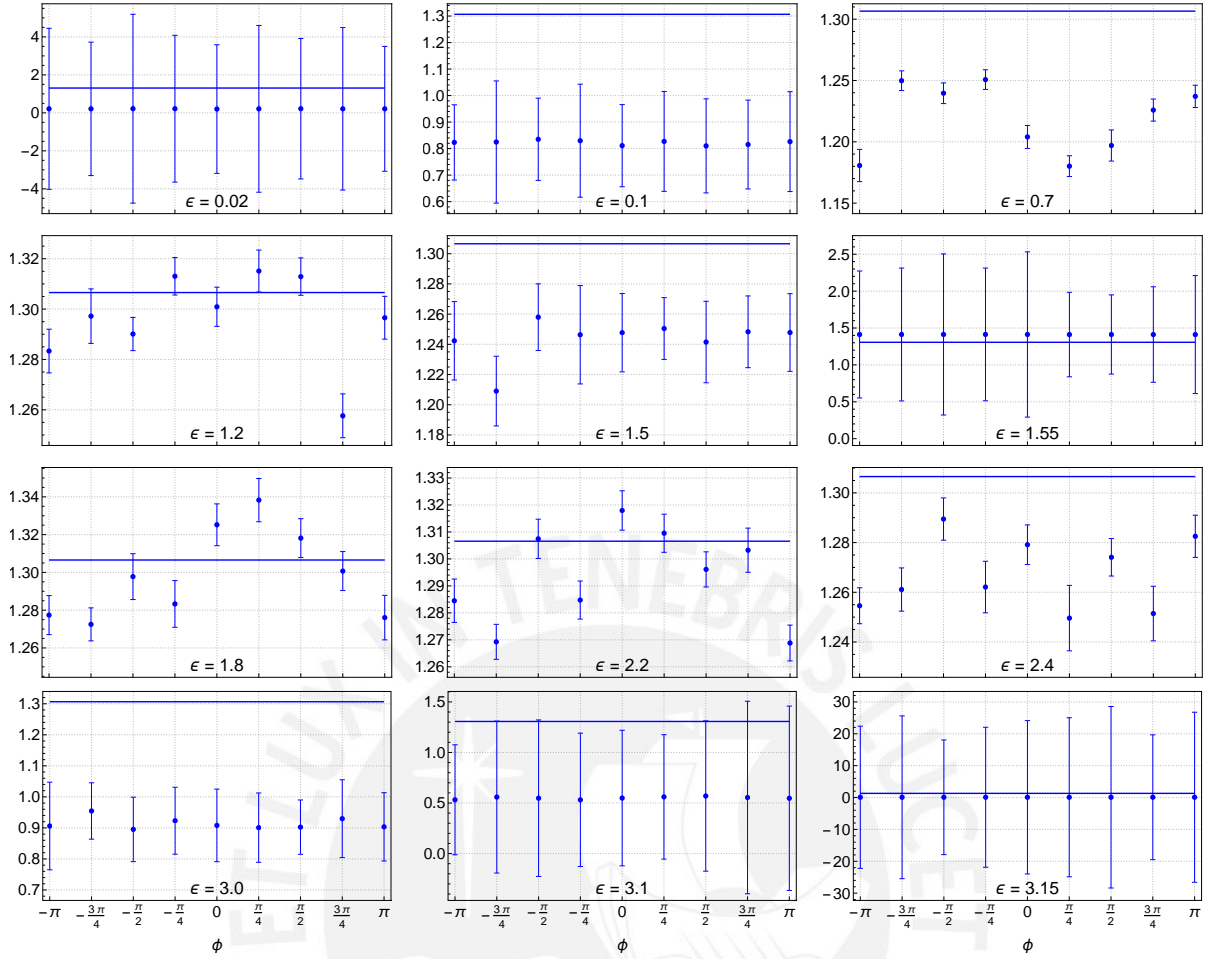
Figure 3.5: Normalization parameter ν of the preselection state $|A_i\rangle$ as a function of ϕ for different measurement strengths ϵ. The solid line indicates the theoretical value $\nu_t = \sqrt{2}\cos(\alpha_i/2) \approx 1.307$. The dots represent the average experimental values of ν, calculated via equation 3.48a, and the error bars are given by σ_ν in equation 3.50a.

strong measurements are not universally superior to weak measurements.

The trends present in figures 3.3 and 3.4 are also found in the preselection state parameters, their statistical uncertainties, and their systematic errors. Figure 3.5 illustrates the results for ν in the same format as figure 3.3 does for R and I. Here, the scale of the vertical axes makes clear how much the error bars, as well as the differences between theoretical and experimental values, vary with increasing measurement strength. These behaviors are indicative of a precision and an accuracy similar to those shown in figure 3.4 for the weak values, which figure 3.6 substantiates–albeit, in the present and following cases, the maximum at $\epsilon = \pi/2$ is manifestly lower than the other two maxima. Likewise, figure 3.7 plots the reconstructed and theoretical angle α_i for twelve
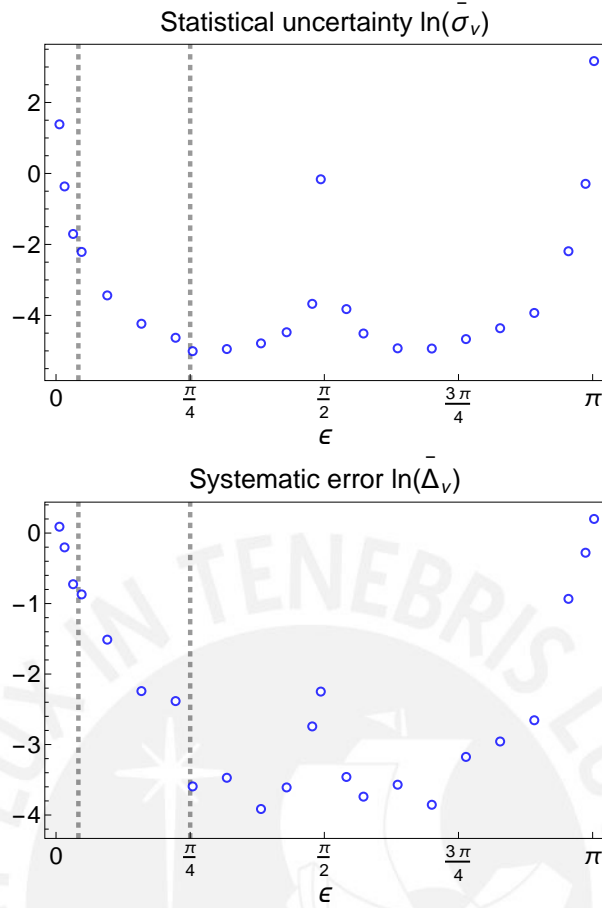
Figure 3.6: Logarithmic plot of the statistical uncertainties and systematic errors (see equations 3.52) of the normalization factor ν of the preselection state $|A_i\rangle$ (see equations 3.45 and 3.47) as functions of the measurement strength parameter ϵ. The vertical dashed lines represent $\epsilon = \pi/24$ and $\epsilon = \pi/4$.

couplings. The dependence of this parameter's precision and accuracy on ϵ, summarized in figure 3.8, resembles that of ν almost perfectly–ostensibly because both parameters stem from intensities i_0 and i_1. To discuss the phase ϕ, we must first observe that, since ϕ is computed from equation 3.48c, whenever $\tan\phi_j = 0$ (as in, say, the case of $\phi_j = -\pi$), the experimental value of ϕ results from subtracting two close numbers, i_4 and i_5. Due to uncontrollable fluctuations in the experiments, either of these numbers can be larger than the other. If, in our example, $i_4 < i_5$, then equation 3.48c will yield a phase with the correct sign (negative). On the other hand, if $i_4 > i_5$, the inverse tangent function introduces a spurious π term to the phase. This issue is addressed by computing ϕ as

$$\phi = \arctan\left|\frac{i_4 - i_5}{i_2 - i_3}\right|, \tag{3.53}$$

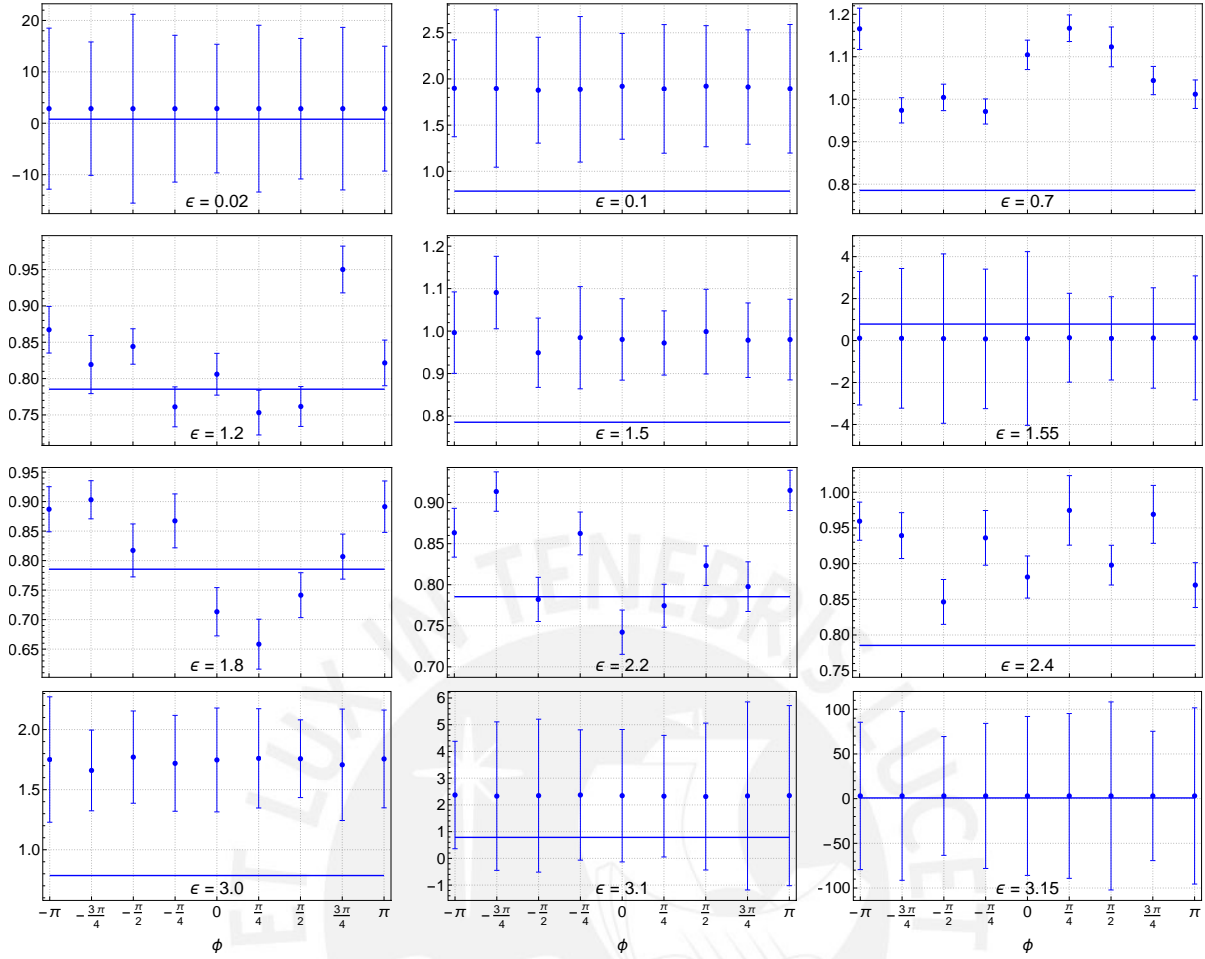which restricts the outputs to the first quadrant. Thence, $\phi_{t,j}$ belongs in practice to the

Figure 3.7: Angle α_i of the preselection state $|A_i\rangle$ as a function of ϕ for different measurement strengths ϵ. The solid line indicates the theoretical value $\alpha_i = \pi/4 \approx 0.785$. The dots represent the average experimental values of α_i, calculated via equation 3.48b, and the error bars are given by σ_α in equation 3.50b.

set $\{0, \pi/4, \pi/2\}$ (cf. equation 3.51c). The plots in figure 3.9 present the products of such calculations. They exhibit the same tendencies for statistical uncertainties and systematic errors as in the previous cases. Unsurprisingly, figure 3.10 shows that the precision and accuracy of ϕ behave similarly to those of ν and α_i. For all three parameters, it is once again true that the weak measurement studied by Denkmayr *et al.* [45] produces worse outcomes than the strong measurement from that same work, as seen from the results highlighted by the vertical dashed lines in figures 3.6, 3.8, and 3.10. Nevertheless, it must be stressed that this observation does not hold in general.
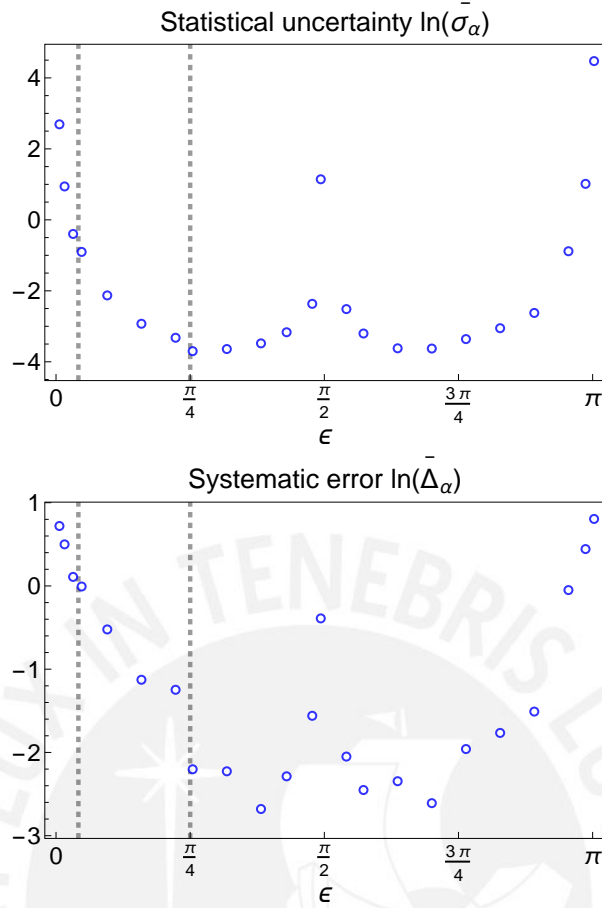
Figure 3.8: Logarithmic plot of the statistical uncertainties and systematic errors (see equations 3.52) of the angle α_i of the preselection state $|A_i\rangle$ (see equations 3.41 and 3.45) as functions of the measurement strength parameter ϵ. The vertical dashed lines represent $\epsilon = \pi/24$ and $\epsilon = \pi/4$.

3.4 Closing Remarks

Our derivation of the closed-form evolution operator (equation 3.9) and of the weak value measurement prescription (equations 3.16) led to a constraint for the coupling parameter ϵ: it ranges, by convention, from 0 to π. Previously, Vallone and Dequal [94] had stated an analogous formula for settings wherein the system is a qudit and the pointer a qubit,[10] which they as well as Zou *et al.* [93] and Calderaro *et al.* [56] used as if its domain were only half as big as ours, despite both being equal. Indeed, Gross

---

10. Equation (S1) of the supplementary information document for [94]. The system observable in the evolution operator (see equation (2) of the main text of [94]) is an arbitrary projector of the computational basis.
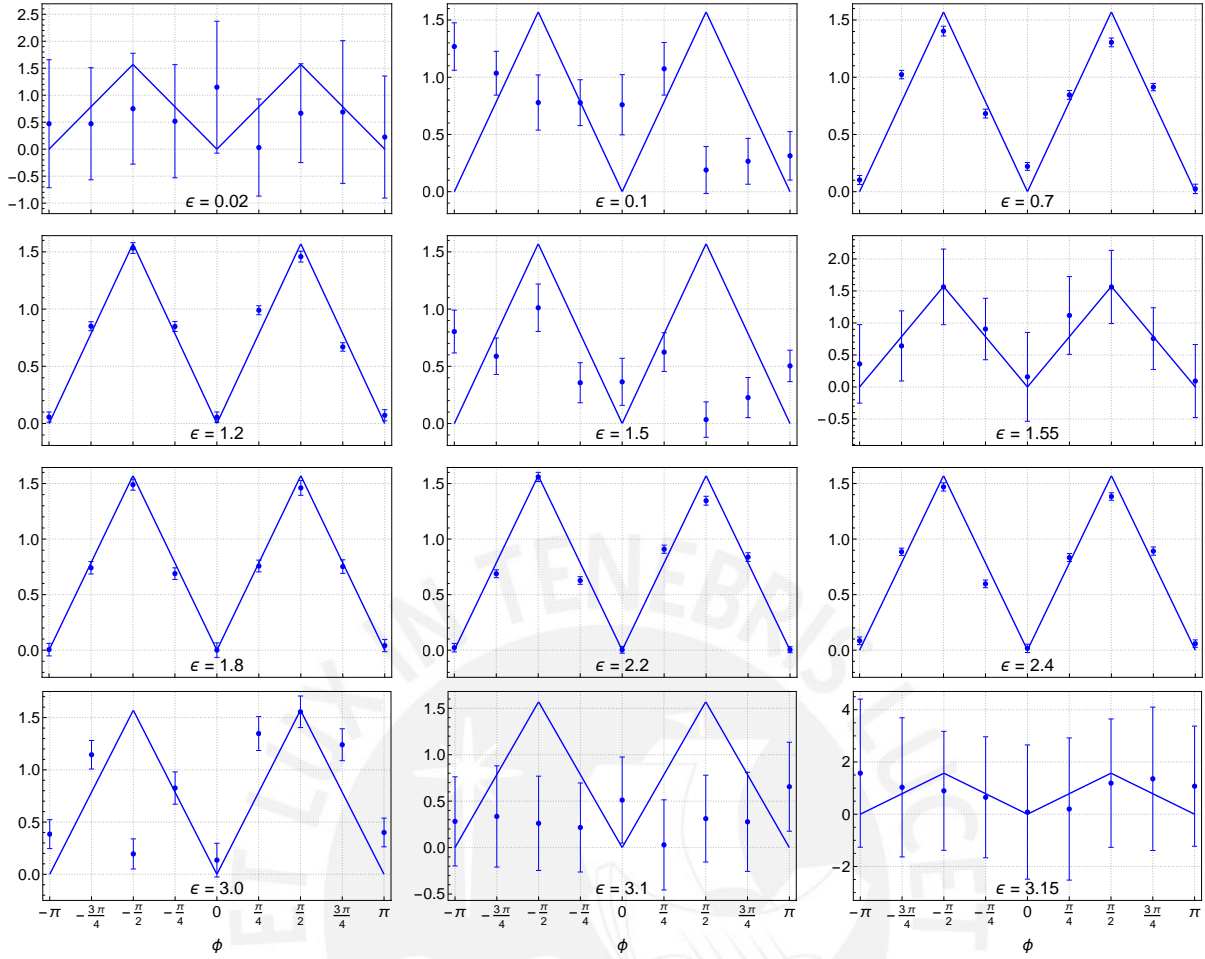
Figure 3.9: Phase ϕ of the preselection state $|A_i\rangle$ as a function of the sample rotation angle ϕ_j for different measurement strengths ϵ. The solid lines contain the theoretical values, which for our case are $0, \pi/4 \approx 0.79$, and $\pi/2 \approx 1.57$. The dots represent the average experimental values of ϕ, calculated via equation 3.53, and the error bars are given by σ_ϕ in equation 3.50c.

et al. [96] referred to Zou et al.'s protocol as "the formula for the strongest possible measurement"; Vallone and Dequal explicitly stated that their parameter belongs to the interval $[0, \pi/2]$; and as late as 2018, Calderaro et al. asserted that they had carried out their schemes "at maximum strength" with the coupling set to $\pi/2$. Denkmayr et al. [45, 46] employed essentially the same closed-form formula as us but even further restricted: in their matter interferometry experiments, $\alpha = \pi/2$, which corresponds to $\epsilon = \pi/4$ in our notation, was the strongest system-pointer interaction available. That these precedents omitted a significant fraction of the allowed values of the coupling parameter in their analyses should serve as a cautionary tale: the domain of a function
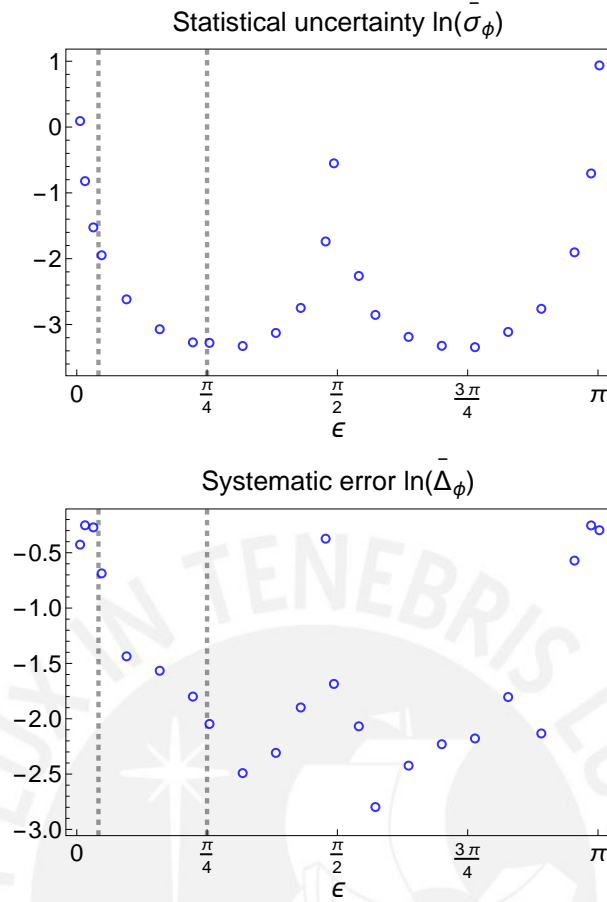
Figure 3.10: Logarithmic plot of the statistical uncertainties and systematic errors (see equations 3.52) of the phase ϕ of the preselection state $|A_i\rangle$ (see equations 3.41 and 3.45) as functions of the measurement strength parameter ϵ. The vertical dashed lines represent $\epsilon = \pi/24$ and $\epsilon = \pi/4$.

must always be specified.

Unlike previous measurement schemes [87, 88, 90, 160, 161] in which the real and imaginary parts of weak values were, to first order in the coupling, proportional to the expectation values of two pointer observables, Vallone and Dequal's model, as well as Denkmayr *et al.*'s and, by extension, ours (all arising from exact, closed-form evolution operators) are self-evidently of an indirect nature.[11] The state characterization schemes associated to these three procedures, on top of not being direct, are not universal, and hence not tomography protocols, for they fail when the postselection state is nearly or outright orthogonal to the preselection (unknown) state. Their utility resides in their

---

11. See equation (S6) of [94], equations (7a)–(7c) of [45], and equations 3.16a–3.16c earlier in this chapter, respectively.

potential for studying the effects of system-pointer interaction strength on the statistical uncertainty and systematic errors of the reconstructed weak values or states. Preliminary analytical assessments of said effects by Gross *et al.* [96] and, within the framework of coupling-deformed observables, by Zhu *et al.* [92] suggested that the best outcomes are produced neither in the weak regime nor at the strongest coupling available, but rather somewhere in between.

Both weak value and state measurement schemes have, since the early days of their respective fields, been realized in classical [19, 40–43] as well as quantum [45, 46, 56, 77, 84, 87, 160] contexts. As sections 3.2.1 and 3.2.2 illustrate, our proposal lends itself to both kinds of treatment. Just as Pryde *et al.*'s paper enjoys pride of place as "the first unambiguously quantum-mechanical experimental" demonstration of weak values [84], and Sponar *et al.*'s article "provides a novel experimental aspect for weak measurements with massive particles" [77], our work represents the first experimental and, moreover, quantum-mechanical survey on how the coupling strength affects the precision and accuracy of weak value and state measurement procedures. Our results largely agree with the theoretical predictions. As a corollary, it bears repeating, strong measurements do not always outperform weak measurements.

Chapter 4

Summary and Outlook

In this final chapter, I first summarise the frameworks and contributions of the two works that comprise this dissertation. Afterwards, I point out possibilities for further research that stem from both the studies reviewed in chapter 1 and the advances presented thereafter–possibilities that, to the best of my knowledge, have not yet been realized. To conclude, I invite researchers to capitalize on the capabilities of currently-existing quantum computers.

4.1 Summary

By way of presenting a theoretical framework, in chapter 1 I examined three strands that unfurl from the fabric of quantum mechanics: quantum state tomography, quantum weak values, and quantum computing. Threading these strands brought forth the topics at the core of this thesis: optimal measurement sets, strong measurements of weak values, and present-day use of cloud-based, superconducting quantum computers. With regard to the first, in section 1.2 I sketched the road leading to James *et al.*'s landmark tomography and estimation protocol [68], and then laid out arguments for the adoption of algorithms that assume state purity. Whereas James *et al.* had outlined how to reconstruct arbitrary two-qubit states by performing 16 measurements, Heinosaari *et al.* [74] proved that pure states of dimension $d = 4$ can be uniquely determined among all pure states from just 9. Gonzales *et al.*'s scheme [75] appeared to achieve this optimal value, but it actually requires additional information, so it became the starting point for the contributions reported here and in [44].

Afterwards, chapter 2 dealt with three proposals set in an all-optical setting: one for state generation and two for state tomography. The procedures for pure states built

on Gonzales *et al.*'s work and overcame both its practical difficulties as well as, most crucially, its crux: not being a proper tomography protocol. The proposal of section 2.1.2 consists of a prescription for characterizing a state by carrying out 12 measurements through a setup highly similar to the one employed in traditional polarization tomography–which greatly simplifies the data recollection process in comparison with measurements on different spatially-separated qubits. The results of experiments done with classical light have shown good agreement with theoretical predictions, thereby stressing the method's usefulness and applicability. A scheme that addresses only pure states, such as the one at hand, could be used by researchers in quantum information science to gauge how reliable pure state sources are, without need for the more resource-intensive full tomography. As a complement, in section 2.2.1, I put forward the mixed state generalization of the pure state protocol. It achieves arbitrary state reconstruction with the minimal amount of measurements possible for a two-qubit system, 16, and, like its pure counterpart, conveniently prescribes data acquisition on a single output port.

Moving on to the remaining topics of this dissertation, section 1.3 broached the subject of weak and strong measurements via the von Neumann model with a continuous Gaussian pointer that mediates the measurement process of a system's observable. Figure 1.1 illustrated strong measurements as those where the coupling strength, the eigenvalue separation, and the pointer spread satisfy $\epsilon(a_{n+1} - a_n) \gg \sigma$. Likewise, figure 1.2 evinced that the weak regime is characterized by $\epsilon(a_{n+1} - a_n) \ggg \sigma$. I then derived the weakness conditions (equations 1.18) under which the evolved state of such a pointer approximates a Gaussian wave function centered, somewhat perplexingly, at a complex number proportional to the weak value. After tracing the historical development of weak values and so-called direct state measurement schemes, I expounded the traits and benefits of the strong regime and arrived at Denkmayr *et al.*'s proposals [45, 46] for weak values and state characterization with arbitrary coupling strength. Their results seemed to suggest that strong measurements always outperform weaker ones. So as to prepare the terrain for the implementation which my colleagues and I carried out of a protocol based on Denkmayr *et al.*'s, section 1.4 gave a primer on quantum computation and, in particular, the use of IBM's superconducting quantum processors.

Lastly, chapter 3 extended Denkmayr *et al.*'s model to arbitrary Pauli spin operators. A small but significant byproduct of this derivation was the domain found for the coupling

strength: $\epsilon \in]0, \pi[$, which authors in several previous works [45, 46, 93, 94, 96] did not consider in its entirety. After introducing the proposal in its most general form, I explained how to realize it in an optical context, either classical or quantum, as well as in a quantum computing context. The latter account included a weak value-based state measurement protocol. Both schemes were implemented in an IBM quantum system. The results revealed that the statistical uncertainties and systematic errors of the weak values and the state parameters do not decrease monotonically as ϵ increases. Rather, they depend on the mathematical nature of the model–which, in this case, performed inconveniently around certain values of ϵ throughout its domain. All the same, there appear to exist measurement settings beyond the weak regime that maximize precision and accuracy. In all, the work done by my coworkers and I represents the first comprehensive experimental study of the effect of coupling strength in the reconstructed quantities.

4.2 Outlook

A pure-state tomography protocol that materializes Heinosaari *et al.*'s prediction of a 9-measurement set for systems of dimension $d = 4$ [74] has not been formulated. Besides finding that any pure, two-qubit state can be uniquely determined among all states by making 11 measurements, Ma *et al.* [73] also proved that the same holds true for pure, three-qubit states with 31 measurements, instead of the 64 demanded by full state tomography. In contrast, Heinosaari *et al.* had already shown that, when further restricted to the set of pure states, such a reconstruction could be achieved with a minimum of either 23 or 24 measurements. An exact number and a corresponding experimental realization are still pending.

To compare the results and theoretical predictions of the pure state protocol of section 2.1, my colleagues and I employed fidelity as a figure of merit. However, several works have questioned the widespread use of fidelity as the end-all be-all benchmark of state reconstruction [162−165]. Furthermore, a demonstration of the mixed, path-polarization tomography scheme proposed in section 2.2 could greatly benefit from using, à la De Burgh *et al.* [71], overcomplete sets of measurements that yield better results (as assessed by more than one quantifier) than the optimal set prescribed by

equations 2.20. In any case, how either tomographic procedure in chapter 2 would perform under different metrics – e.g., the Chernoff bound [71] – is an open question.

Quantum state tomography of high-dimensional states ($d \gg 1$) bears the onus of unmanageable complexity for both measurement and reconstruction processes. As stated in [152], by early 2009, an eight-qubit state characterization [166] was the "most complicated [...] tomographic measurement performed to date". Indeed, it had "required hundreds of thousands of measurements and weeks of postprocessing" [167]. Although I have repeatedly extolled the virtues of the purity assumption, there exist tomographic techniques that, despite not adopting it, have enabled astonishing achievements. One of them, known as compressed-sensing quantum tomography [167, 168] is valid for arbitrary states, employs incomplete measurement sets, and its performance does not decay significantly when the purity constraint is relaxed [168]. This procedure has been combined with Lundeen *et al.*'s [87] to determine a 256×256 pixel wave front efficiently from just $10\,000$ random projections [169], as well as a 1.2 million-dimensional photonic state state [170]. Whatever astounding higher-dimensional reconstructions and applications thereof could emerge remain a thrilling prospect.

Zhang *et al.*'s proposal of coupling-deformed pointer observables [91] engendered a universal, bias-free tomography protocol [92]. Zhu *et al.* have continued to work on this model: they formulated a tomographic procedure with a continuous pointer and showed analytically how it could be optimized with two concurrent coupling parameters [171]; and they also derived and explored an adaptive tomography scheme that can outperform other widely-used protocols, in terms of precision, at higher dimensions [172]. The various techniques that fall under the umbrella of coupling-deformed observables have not, as of yet, been realized in a laboratory. In addition, equipping the original framework [91] with an accessible motivation and, more fundamentally, interpretation could push it back into the spotlight of current research.

As illustrated by the results in section 3.3, weak values and state parameters can be experimentally reconstructed from measurements of almost arbitrary coupling strength. Given the evidence that the quality of state reconstruction is independent of the pointer's dimensionality [90], the fact that more closed-form evolution operators like the one in equation 3.9 are in principle obtainable, and the existence of universal state measurement methods [56, 91, 92], protocols for systems defined in higher-dimensional

spaces, their mixed-state extensions, and their tomographic generalizations could be constructed. These results also suggest that statistical uncertainties and systematic errors can be minimized by selecting an appropriate coupling strength. How the precision and accuracy of system-pointer-based measurement schemes fare vis-à-vis traditional tomography procedures could be answered by a comprehensive comparison of the two methods, such as was previously done, e.g., by Gross *et al.* [96].

Finally, as experience has shown time and again, cloud-based quantum computing systems have unleashed a terrific potential for empirical research. The low barriers to access to these systems are an entreaty to workers from all walks of science, not just physics, to join in. Scientists would be remiss not to sail with the tailwinds of quantum computation.
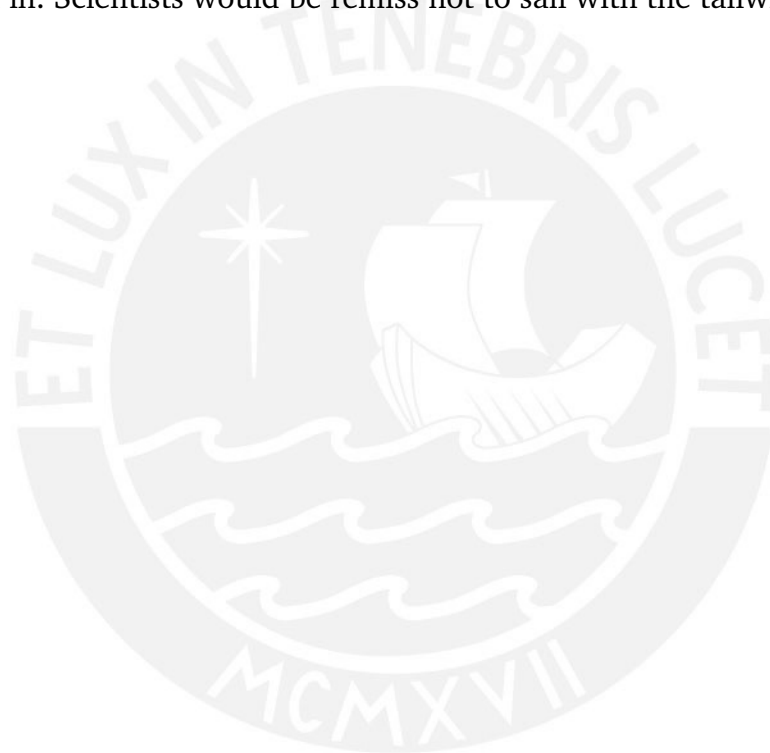
Bibliography

[1]   E. SCHRÖDINGER. "Die gegenwärtige Situation in der Quantenmechanik". *Die Naturwissenschaften* **23**, 807–812 (1935). (See p. 1).

[2]   E. SCHRÖDINGER. "Discussion of Probability Relations between Separated Systems". *Mathematical Proceedings of the Cambridge Philosophical Society* **31**, 555–563 (1935). (See p. 1).

[3]   A. EINSTEIN, B. PODOLSKY, and N. ROSEN. "Can Quantum-Mechanical Description of Physical Reality Be Considered Complete?" *Physical Review* **47**, 777–780 (1935). (See p. 1).

[4]   J. H. EBERLY et al. "Quantum and classical optics–emerging links". *Phys. Scr.* **91**, 063003 (2016). (See p. 1).

[5]   J. VON NEUMANN. *Mathematical Foundations of Quantum Mechanics*. Princeton University Press, 1955. (See pp. 1, 8).

[6]   E. KNILL and R. LAFLAMME. "Power of One Bit of Quantum Information". *Physical Review Letters* **81**, 5672–5675 (1998). (See p. 2).

[7]   H. OLLIVIER and WOJCIECH H. ZUREK. "Quantum Discord: A Measure of the Quantumness of Correlations". *Physical Review Letters* **88**, 017901 (2001). (See p. 2).

[8]   ANIMESH DATTA, STEVEN T. FLAMMIA, and CARLTON M. CAVES. "Entanglement and the power of one qubit". *Physical Review A* **72**, 042316 (2005). (See p. 2).

[9]   ANIMESH DATTA, ANIL SHAJI, and CARLTON M. CAVES. "Quantum Discord and the Power of One Qubit". *Physical Review Letters* **100**, 050502 (2008). (See p. 2).

[10] PETER W. SHOR. "Polynomial-Time Algorithms for Prime Factorization and Discrete Logarithms on a Quantum Computer". *SIAM Journal on Computing* **26**, 1484–1509 (1997). (See pp. 2, 18).

[11] LOV K. GROVER. "Quantum Mechanics Helps in Searching for a Needle in a Haystack". *Physical Review Letters* **79**, 325–328 (1997). (See pp. 2, 18).

[12] EVAN R. MACQUARRIE, CHRISTOPH SIMON, STEPHANIE SIMMONS, and ELICIA MAINE. "The emerging commercial landscape of quantum computing". *Nature Reviews Physics* **2**, 596–598 (2020). (See p. 2).

[13] YUDONG CAO et al. "Quantum Chemistry in the Age of Quantum Computing". *Chemical Reviews* **119**, 10856–10915 (2019). (See p. 2).

[14] M. CEREZO et al. "Variational quantum algorithms". *Nature Reviews Physics* **3**, 625–644 (2021). (See p. 2).

[15] DANIEL J. EGGER et al. "Quantum Computing for Finance: State-of-the-Art and Future Prospects". *IEEE Transactions on Quantum Engineering* **1**, 1–24 (2020). (See p. 2).

[16] FRANK GAITAN. "Finding Solutions of the Navier-Stokes Equations through Quantum Computing–Recent Progress, a Generalization, and Next Steps Forward". *Advanced Quantum Technologies* **4**, 2100055 (2021). (See p. 2).

[17] YAKIR AHARONOV, DAVID Z. ALBERT, and LEV VAIDMAN. "How the result of a measurement of a component of the spin of a spin-$1/2$ particle can turn out to be 100". *Physical Review Letters* **60**, 1351–1354 (1988). (See pp. 2, 8).

[18] Y. AHARONOV and L. VAIDMAN. "Complete description of a quantum system at a given time". *Journal of Physics A: Mathematical and General* **24**, 2315 (1991). (See p. 2).

[19] K.J. RESCH, J.S. LUNDEEN, and A.M. STEINBERG. "Experimental realization of the quantum box problem". *Physics Letters A* **324**, 125–131 (2004). (See pp. 2, 67).

[20] YAKIR AHARONOV, SANDU POPESCU, DANIEL ROHRLICH, and PAUL SKRZYPCZYK. "Quantum Cheshire Cats". *New Journal of Physics* **15**, 113015 (2013). (See p. 2).

[21] TOBIAS DENKMAYR et al. "Observation of a quantum Cheshire Cat in a matter-wave interferometer experiment". *Nature Communications* **5**, 4492 (2014). (See p. 2).

[22] SACHA KOCSIS et al. "Observing the Average Trajectories of Single Photons in a Two-Slit Interferometer". *Science* **332**, 1170–1173 (2011). (See pp. 2, 46).

[23] KONSTANTIN Y. BLIOKH, ALEKSANDR Y. BEKSHAEV, ABRAHAM G. KOFMAN, and F. NORI. "Photon trajectories, anomalous velocities and weak measurements: a classical interpretation". *New Journal of Physics* **15**, 073022 (2013). (See p. 2).

[24] LUCIEN HARDY. "Quantum mechanics, local realistic theories, and Lorentz-invariant realistic theories". *Physical Review Letters* **68**, 2981–2984 (1992) . (See p. 2).

[25] YAKIR AHARONOV et al. "Revisiting Hardy's paradox: counterfactual statements, real measurements, entanglement and weak values". *Physics Letters A* **301**, 130–138 (2002). (See p. 2).

[26] DYLAN H. MAHLER et al. "Experimental nonlocal and surreal Bohmian trajectories". *Science Advances* **2**, e1501466 (2016). (See p. 2).

[27] JOSHUA FOO, ESTELLE ASMODELLE, AUSTIN P. LUND, and TIMOTHY C. RALPH. "Relativistic Bohmian trajectories of photons via weak measurements". *Nature Communications* **13**, 4002 (2022). (See p. 2).

[28] JUSTIN DRESSEL et al. "Colloquium: Understanding quantum weak values: Basics and applications". *Reviews of Modern Physics* **86**, 307–316 (2014). (See pp. 2, 4, 13, 14).

[29] ROBERT J. C. SPREEUW. "A Classical Analogy of Entanglement". *Foundations of Physics* **28**, 361–374 (1998). (See p. 2).

[30] ROBERT J. C. SPREEUW. "Classical wave-optics analogy of quantum-information processing". *Physical Review A* **63**, 062302 (2001). (See p. 2).

[31] MATIAS A. GOLDIN, DIEGO FRANCISCO, and SILVIA LEDESMA. "Simulating Bell inequality violations with classical optics encoded qubits". *Journal of the Optical Society of America B* **27**, 779–786 (2010). (See p. 2).

[32] C. V. S. BORGES, M. HOR-MEYLL, J. A. O. HUGUENIN, and A. Z. KHOURY. "Bell-like inequality for the spin-orbit separability of a laser beam". *Physical Review A* **82**, 033833 (2010). (See p. 2).

[33] KUMEL H. KAGALWALA, GIOVANNI DI GIUSEPPE, A. F. ABOURADDY, and E. A. SALEH. "Bell's measure in classical optical coherence". *Nature Photonics* **7**, 72–78 (2013). (See p. 2).

[34] XIAO-FENG QIAN, BETHANY LITTLE, JOHN C. HOWELL, and J. H. EBERLY. "Shifting the quantum-classical boundary: theory and experiment for statistically classical optical fields". *Optica* **2**, 611–615 (2015). (See pp. 2, 33).

[35] N. SANDEAU, H. AKHOUAYRI, A. MATZKIN, and T. DURT. "Experimental violation of Tsirelson's bound by Maxwell fields". *Physical Review A* **93**, 053829 (2016). (See pp. 2, 33).

[36] J. GONZALES et al. "Experimental Bell violations with classical, non-entangled optical fields". *Journal of Physics B: Atomic, Molecular and Optical Physics* **51**, 045401 (2018). (See p. 2).

[37] P. G. KWIAT, J. R. MITCHELL, P. D. D. SCHWINDT, and A. G. WHITE. "Grover's search algorithm: An optical approach". *Journal of Modern Optics* **47**, 257–266 (2000). (See p. 2).

[38] NANDINI BHATTACHARYA, H. B. VAN LINDEN VAN DEN HEUVELL, and ROBERT J. C. SPREEUW. "Implementation of Quantum Search Algorithm using Classical Fourier Optics". *Physical Review Letters* **88**, 137901 (2002). (See p. 2).

[39] DIEGO FRANCISCO and SILVIA LEDESMA. "Classical optics analogy of quantum teleportation". *Journal of the Optical Society of America B* **25**, 383–390 (2008). (See p. 2).

[40] NICHOLAS W. M. RITCHIE, J. G. STORY, and RANDALL G. HULET. "Realization of a measurement of a "weak value"". *Physical Review Letters* **66**, 1107–1110 (1991). (See pp. 2, 13, 67).

[41] D. R. SOLLI et al. "Fast Light, Slow Light, and Phase Singularities: A Connection to Generalized Weak Values". *Physical Review Letters* **92**, 043601 (2004). (See pp. 2, 67).

[42] JEFF Z. SALVAIL et al. "Full characterization of polarization states of light via direct measurement". *Nature Photonics* **7**, 316–321 (2013). (See pp. 2, 14, 54, 67).

[43]   G. S. THEKKADATH et al. "Direct Measurement of the Density Matrix of a Quantum System". *Physical Review Letters* **117**, 120401 (2016) . (See pp. 2, 14, 67).

[44]   DAVID R. A. RUELAS PAREDES et al. "Synthesis and characterization of pure, two-qubit states encoded in path and polarization". *Journal of Optics* **23**, 085201 (2021). (See pp. 3, 7, 27, 39, 68).

[45]   TOBIAS DENKMAYR et al. "Experimental Demonstration of Direct Path State Characterization by Strongly Measuring Weak Values in a Matter-Wave Interferometer". *Physical Review Letters* **118**, 010402 (2017) . (See pp. 3, 8, 17, 45, 54–57, 60, 63, 65–67, 69, 70).

[46]   TOBIAS DENKMAYR et al. "Weak values from strong interactions in neutron interferometry". *Physica B: Condensed Matter* **551**, 339–346 (2018) . (See pp. 3, 8, 17, 45, 65, 67, 69, 70).

[47]   C. COHEN-TANNOUDJI, B. DIU, and F. LALOE. *Quantum Mechanics*. Wiley, 1991. (See p. 3).

[48]   JUN JOHN SAKURAI. *Modern Quantum Mechanics, Revised Edition*. Addison-Wesley Publishing Company, 1994. (See p. 3).

[49]   ROGER G. NEWTON and BING-LIN YOUNG. "Measurability of the spin density matrix". *Annals of Physics* **49**, 393–402 (1968). (See p. 4).

[50]   WILLIAM BAND and JAMES L. PARK. "The empirical determination of quantum states". *Foundations of Physics* **1**, 133–144 (1970). (See p. 4).

[51]   JAMES L. PARK and W. BAND. "A general theory of empirical state determination in quantum physics: Part I". *Foundations of Physics* **1**, 211–226 (1971) . (See p. 4).

[52]   WILLIAM BAND and JAMES L. PARK. "A general method of empirical state determination in quantum physics: Part II". *Foundations of Physics* **1**, 339–357 (1971). (See p. 4).

[53]   K. VOGEL and H. RISKEN. "Determination of quasiprobability distributions in terms of probability distributions for the rotated quadrature phase". *Physical Review A* **40**, 2847–2849 (1989). (See p. 4).

[54]   G. MAURO D'ARIANO, MATTEO G.A. PARIS, and MASSIMILIANO F. SACCHI. "Quantum tomography". In *Advances in Imaging and Electron Physics*. Vol. 128. Edited by PETER W. HAWKES. Elsevier Academic Press, 2003, 206–309 (see p. 4).

[55]   A. I. LVOVSKY and M. G. RAYMER. "Continuous-variable optical quantum-state tomography". *Reviews of Modern Physics* **81**, 299–332 (2009). (See p. 4).

[56]   LUCA CALDERARO et al. "Direct Reconstruction of the Quantum Density Matrix by Strong Measurements". *Physical Review Letters* **121**, 230501 (2018). (See pp. 4, 14–16, 64, 67, 71).

[57]   LIANG XU et al. "Direct Characterization of Quantum Measurements Using Weak Values". *Physical Review Letters* **127**, 180401 (2021). (See pp. 4, 16).

[58]   D. T. SMITHEY, M. BECK, M. G. RAYMER, and A. FARIDANI. "Measurement of the Wigner distribution and the density matrix of a light mode using optical homodyne tomography: Application to squeezed states and the vacuum". *Physical Review Letters* **70**, 1244–1247 (1993). (See p. 4).

[59]   G. BREITENBACH, S. SCHILLER, and J. MLYNEK. "Measurement of the quantum states of squeezed light". *Nature* **387**, 471 (1997). (See p. 4).

[60]   J. W. WU, P. K. LAM, M. B. GRAY, and H.-A. BACHOR. "Optical homodyne tomography of information carrying laser beams". *Optics Express* **3**, 154–161 (1998). (See p. 4).

[61]   J. R. ASHBURN et al. "Experimentally determined density matrices for H(n=3) formed in H^+-He collisions from 20 to 100 keV". *Physical Review A* **41**, 2407–2421 (1990). (See p. 4).

[62]   T. J. DUNN, I. A. WALMSLEY, and S. MUKAMEL. "Experimental Determination of the Quantum-Mechanical State of a Molecular Vibrational Mode Using Fluorescence Tomography". *Physical Review Letters* **74**, 884–887 (1995). (See p. 4).

[63]   ISAAC L. CHUANG, NEIL GERSHENFELD, and MARK KUBINEC. "Experimental Implementation of Fast Quantum Searching". *Physical Review Letters* **80**, 3408–3411 (1998). (See pp. 4, 20).

[64] ANIRUDH ACHARYA, THEODORE KYPRAIOS, and MĂDĂLIN GUŢĂ. "A comparative study of estimation methods in quantum tomography". *Journal of Physics A: Mathematical and Theoretical* **52**, 234001 (2019). (See pp. 4, 39).

[65] Z. HRADIL. "Quantum-state estimation". *Physical Review A* **55**, R1561–R1564 (1997). (See pp. 4, 37).

[66] KONRAD BANASZEK. "Maximum-likelihood estimation of photon-number distribution from homodyne statistics". *Physical Review A* **57**, 5013–5015 (1998). (See p. 4).

[67] K. BANASZEK, G. M. D'ARIANO, M. G. A. PARIS, and M. F. SACCHI. "Maximum-likelihood estimation of the density matrix". *Physical Review A* **61**, 010304(R) (1999). (See p. 4).

[68] DANIEL F. V. JAMES, PAUL G. KWIAT, WILLIAM J. MUNRO, and ANDREW G. WHITE. "Measurement of qubits". *Physical Review A* **64**, 052312 (2001). (See pp. 5, 6, 13, 37, 38, 68).

[69] S.P. WALBORN, C.H. MONKEN, S. PÁDUA, and P.H. SOUTO RIBEIRO. "Spatial correlations in parametric down-conversion". *Physics Reports* **495**, 87–139 (2010). (See p. 5).

[70] JAMES SCHNEELOCH and JOHN C. HOWELL. "Introduction to the transverse spatial correlations in spontaneous parametric down-conversion through the biphoton birth zone". *Journal of Optics* **18**, 053501 (2016). (See p. 5).

[71] MARK D. DE BURGH, NATHAN K. LANGFORD, ANDREW C. DOHERTY, and ALEXEI GILCHRIST. "Choice of measurement sets in qubit tomography". *Physical Review A* **78** (2008). (See pp. 5, 6, 70, 71).

[72] M.A. NIELSEN and I.L. CHUANG. *Quantum Computation and Quantum Information: 10th Anniversary Edition*. Cambridge University Press, 2010. (See pp. 5, 16, 42).

[73] XIAN MA et al. "Pure-state tomography with the expectation value of Pauli operators". *Physical Review A* **93**, 032140 (2016). (See pp. 6, 70).

[74] TEIKO HEINOSAARI, LUCA MAZZARELLA, and MICHAEL M. WOLF. "Quantum Tomography under Prior Information". *Communications in Mathematical Physics* **318**, 355–374 (2013). (See pp. 6, 43, 68, 70).

[75] J. GONZALES et al. "Unrestricted generation of pure two-qubit states and entanglement diagnosis by single-qubit tomography". *Optics Letters* **44**, 3310–3313 (2019). (See pp. 7, 30, 33, 68).

[76] G.M. D'ARIANO and M.F. SACCHI. "Optical von Neumann measurement". *Physics Letters A* **231**, 325–330 (1997). (See p. 8).

[77] S. SPONAR et al. "Weak values obtained in matter-wave interferometry". *Physical Review A* **92**, 062121 (2015). (See pp. 8, 17, 67).

[78] I. M. DUCK, P. M. STEVENSON, and E. C. G. SUDARSHAN. "The sense in which a "weak measurement" of a spin-$1/2$ particle's spin component yields a value 100". *Physical Review D* **40**, 2112–2117 (1989). (See pp. 11, 13).

[79] JEFFREY STEPHEN LUNDEEN. "Generalized measurement and post-selection in optical quantum information". Ph.D. thesis, University of Toronto, 2006. (See p. 12).

[80] LARS M. JOHANSEN. "Weak Measurements with Arbitrary Probe States". *Physical Review Letters* **93**, 120402 (2004). (See p. 12).

[81] NATHAN S. WILLIAMS and ANDREW N. JORDAN. "Weak Values and the Leggett-Garg Inequality in Solid-State Qubits". *Physical Review Letters* **100**, 026804 (2008). (See p. 12).

[82] L. M. JOHANSEN. "Reconstructing weak values without weak measurements". *Physics Letters A* **366**, 374–376 (2007). (See pp. 12, 14).

[83] S. POPESCU. "Weak measurements just got stronger". *Physics* **2**, 32 (2009). (See p. 13).

[84] G. J. PRYDE et al. "Measurement of Quantum Weak Values of Photon Polarization". *Physical Review Letters* **94**, 220405 (2005). (See pp. 13, 17, 67).

[85] P. BEN DIXON, DAVID J. STARLING, ANDREW N. JORDAN, and JOHN C. HOWELL. "Ultrasensitive Beam Deflection Measurement via Interferometric Weak Value Amplification". *Physical Review Letters* **102**, 173601 (2009). (See p. 13).

[86] ONUR HOSTEN and PAUL KWIAT. "Observation of the Spin Hall Effect of Light via Weak Measurements". *Science* **319**, 787–790 (2008). (See p. 13).

[87] JEFF S. LUNDEEN et al. "Direct measurement of the quantum wavefunction". *Nature* **474**, 188–191 (2011). (See pp. 13–15, 44, 54, 55, 66, 67, 71).

[88] JEFF S. LUNDEEN and CHARLES BAMBER. "Procedure for Direct Measurement of General Quantum States Using Weak Measurement". *Physical Review Letters* **108**, 070402 (2012). (See pp. 14, 15, 66).

[89] ERKKA HAAPASALO, PEKKA LAHTI, and JUSSI SCHULTZ. "Weak versus approximate values in quantum state determination". *Physical Review A* **84**, 052107 (2011). (See pp. 14, 44).

[90] LORENZO MACCONE and COSIMO C. RUSCONI. "State estimation: A comparison between direct state measurement and tomography". *Physical Review A* **89**, 022122 (2014). (See pp. 14, 15, 66, 71).

[91] YU-XIANG ZHANG, SHENGJUN WU, and ZENG-BING CHEN. "Coupling-deformed pointer observables and weak values". *Physical Review A* **93**, 032128 (2016). (See pp. 14, 15, 71).

[92] XUANMIN ZHU, YU-XIANG ZHANG, and SHENGJUN WU. "Direct state reconstruction with coupling-deformed pointer observables". *Physical Review A* **93**, 062304 (2016). (See pp. 14–16, 44, 67, 71).

[93] PING ZOU, ZHI-MING ZHANG, and WEI SONG. "Direct measurement of general quantum states using strong measurement". *Physical Review A* **91**, 052109 (2015). (See pp. 15, 64, 70).

[94] GIUSEPPE VALLONE and DANIELE DEQUAL. "Strong Measurements Give a Better Direct Measurement of the Quantum Wave Function". *Physical Review Letters* **116**, 040502 (2016). (See pp. 15, 16, 57, 64, 66, 70).

[95] DEBMALYA DAS and ARVIND. "Estimation of quantum states by weak and projective measurements". *Physical Review A* **89**, 062121 (2014) . (See pp. 15, 16).

[96]   JONATHAN A. GROSS, NINNAT DANGNIAM, CHRISTOPHER FERRIE, and CARL-
       TON M. CAVES. "Novelty, efficacy, and significance of weak measurements for
       quantum tomography". *Physical Review A* **92**, 062133 (2015). (See pp. 16, 44,
       65, 67, 70, 72).

[97]   PAUL BENIOFF. "The computer as a physical system: A microscopic quantum me-
       chanical Hamiltonian model of computers as represented by Turing machines".
       Journal of Statistical Physics **22**, 563–591 (1980). (See p. 18).

[98]   Y. MANIN. *Computable and uncomputable*. Sovetskoye Radio, Moscow, 1980.
       (See p. 18).

[99]   RICHARD P. FEYNMAN. "Simulating physics with computers". *International
       Journal of Theoretical Physics* **21**, 467–488 (1982). (See p. 18).

[100] P. A. BENIOFF. "Quantum mechanical Hamiltonian models of discrete processes
       that erase their own histories: Application to Turing machines". *International
       Journal of Theoretical Physics* **21**, 177–201 (1982). (See p. 18).

[101] PAUL ANTHONY BENIOFF. "Quantum Mechanical Hamiltonian Models of Turing
       Machines". *Journal of Statistical Physics* **29**, 515–546 (1982). (See p. 18).

[102] W. K. WOOTTERS and W. H. ZUREK. "A single quantum cannot be cloned".
       Nature **299**, 802–803 (1982). (See p. 18).

[103] BENJAMIN SCHUMACHER. "Quantum coding". *Physical Review A* **51**, 2738–2747
       (1995). (See p. 18).

[104] CHARLES H. BENNETT and GILLES BRASSARD. "Quantum cryptography: Public
       key distribution and coin tossing". *Theoretical Computer Science* **560**, 7–11
       (2014). (See p. 18).

[105] ASHER PERES. "Reversible logic and quantum computers". *Physical Review A*
       32, 3266–3276 (1985). (See p. 18).

[106] CHARLES H. BENNETT et al. "Purification of Noisy Entanglement and Faithful
       Teleportation via Noisy Channels". *Physical Review Letters* **76**, 722–725 (1996)
       . (See p. 18).

[107] DAVID DEUTSCH and RICHARD JOZSA. "Rapid solution of problems by quantum computation". *Proceedings of the Royal Society of London. Series A: Mathematical and Physical Sciences* **439**, 553–558 (1992). (See p. 18).

[108] DANIEL R. SIMON. "On the Power of Quantum Computation". *SIAM Journal on Computing* **26**, 1474–1483 (1997). (See p. 18).

[109] LOV K. GROVER. "A Fast Quantum Mechanical Algorithm for Database Search". In *Proceedings of the Twenty-Eighth Annual ACM Symposium on Theory of Computing*. Association for Computing Machinery, Philadelphia, Pennsylvania, USA, 1996, 212–219. (See p. 18).

[110] DAVID P. DIVINCENZO. "The Physical Implementation of Quantum Computation". *Fortschritte der Physik* **48**, 771–783 (2000). (See pp. 18, 19).

[111] IULIA GEORGESCU. "The DiVincenzo criteria 20 years on". *Nature Reviews Physics* **2**, 666 (2020). (See p. 18).

[112] T. WILK et al. "Entanglement of Two Individual Neutral Atoms Using Rydberg Blockade". *Physical Review Letters* **104**, 010502 (2010). (See p. 19).

[113] MAXIMILIAN SCHLOSSHAUER. "Quantum decoherence". *Physics Reports* **831**, 1–57 (2019). (See p. 19).

[114] P. KRANTZ et al. "A quantum engineer's guide to superconducting qubits". *Applied Physics Reviews* **6**, 021318 (2019). (See pp. 19, 20).

[115] D. P. DIVINCENZO. "Two-bit gates are universal for quantum computation". *Physical Review A* **51**, 1015–1022 (1995). (See p. 20).

[116] IBM QUANTUM. *System properties*. https://web.archive.org/web/20230512140821/https://quantum-computing.ibm.com/composer/docs/iqx/manage/systems/properties (see p. 20).

[117] C. MONROE et al. "Demonstration of a Fundamental Quantum Logic Gate". *Physical Review Letters* **75**, 4714–4717 (1995). (See p. 20).

[118] JONATHAN A. JONES, MICHELE MOSCA, and RASMUS H. HANSEN. "Implementation of a quantum search algorithm on a quantum computer". *Nature* **393**, 344–346 (1998). (See p. 20).

[119] NOAH LINDEN, HERVÉ BARJAT, and RAY FREEMAN. "An implementation of the Deutsch–Jozsa algorithm on a three-qubit NMR quantum computer". *Chemical Physics Letters* **296**, 61–67 (1998). (See p. 20).

[120] R. MARX et al. "Approaching five-bit NMR quantum computing". *Physical Review A* **62**, 012310 (2000). (See p. 20).

[121] YASUNOBU NAKAMURA, YU A. PASHKIN, and J. S. TSAI. "Coherent control of macroscopic quantum states in a single-Cooper-pair box". *Nature* **398**, 786–788 (1999). (See pp. 20, 21).

[122] R.A. SERWAY, C.J. MOSES, and C.A. MOYER. *Modern Physics*. 3rd edition. Thomson Brooks/Cole, 2005. (See p. 21).

[123] J.M. MARTINIS. "Superconducting qubits and the physics of Josephson junctions". In *Quantum Entanglement and Information Processing: Lecture Notes of the Les Houches Summer School 2003*. Edited by D. ESTÈVE, J.-M. RAIMOND, and J. DALIBARD. Les Houches, France, 2004. (See p. 21).

[124] YU. A. PASHKIN et al. "Josephson charge qubits: a brief review". *Quantum Information Processing* **8**, 55–80 (2009). (See p. 21).

[125] HE-LIANG HUANG, DACHAO WU, DAOJIN FAN, and XIAOBO ZHU. "Superconducting quantum computing: a review". *Science China Information Sciences* **63**, 180501 (2020). (See p. 21).

[126] JENS KOCH et al. "Charge-insensitive qubit design derived from the Cooper pair box". *Physical Review A* **76**, 042319 (2007). (See p. 21).

[127] MEHDI BOZZO-REY and ROBERT LOREDO. "Introduction to the IBM Q Experience and Quantum Computing". In *Proceedings of the 28th Annual International Conference on Computer Science and Software Engineering*. IBM Corp., Markham, Ontario, Canada, 2018, 410–412. (See p. 21).

[128] IBM QUANTUM. *The qubit*. `https://web.archive.org/web/20230502013627/https://quantum-computing.ibm.com/composer/docs/iqx/guide/the-qubit` (see p. 21).

[129] DANIEL ALSINA and JOSÉ IGNACIO LATORRE. "Experimental test of Mermin inequalities on a five-qubit quantum computer". *Physical Review A* **94**, 012314 (2016). (See p. 22).

[130] SIMON J. DEVITT. "Performing quantum computing experiments in the cloud". *Physical Review A* **94**, 032329 (2016). (See p. 22).

[131] BIBEK POKHAREL, NAMIT ANAND, BENJAMIN FORTMAN, and DANIEL A. LIDAR. "Demonstration of Fidelity Improvement Using Dynamical Decoupling with Superconducting Qubits". *Physical Review Letters* **121**, 220502 (2018) . (See p. 22).

[132] DEBJIT GHOSH et al. "Automated error correction in IBM quantum computer and explicit generalization". *Quantum Information Processing* **17**, 153 (2018). (See p. 22).

[133] YANZHU CHEN, MAZIAR FARAHZAD, SHINJAE YOO, and TZU-CHIEH WEI. "Detector tomography on IBM quantum computers and mitigation of an imperfect measurement". *Physical Review A* **100**, 052315 (2019). (See p. 22).

[134] BIKASH K. BEHERA, SWARNADEEP SETH, ANTARIKSHA DAS, and PRASANTA K. PANIGRAHI. "Demonstration of entanglement purification and swapping protocol to design quantum repeater in IBM quantum computer". *Quantum Information Processing* **18**, 108 (2019). (See p. 22).

[135] NICOLAS SCHWALLER, MARC-ANDRÉ DUPERTUIS, and CLÉMENT JAVERZAC-GALY. "Evidence of the entanglement constraint on wave-particle duality using the IBM Q quantum computer". *Physical Review A* **103**, 022409 (2021). (See p. 22).

[136] GADI ALEKSANDROWICZ et al. *Qiskit: An Open-source Framework for Quantum Computing*. https://zenodo.org/record/2562111. 2019 (see p. 22).

[137] SHELDON M. ROSS. *Introduction to Probability and Statistics for Engineers and Scientists*. 3rd edition. Academic Press, 2004. (See p. 26).

[138] KET.G. *¿Cuántos shots debo utilizar?* https://www.youtube.com/watch?v=00fMTHhqD7o. 2021 (see p. 26).

[139] TIRTHAK PATEL et al. "Experimental Evaluation of NISQ Quantum Computers: Error Measurement, Characterization, and Implications". In *SC20: International Conference for High Performance Computing, Networking, Storage and Analysis*. Association for Computing Machinery, Atlanta, Georgia, USA, 2020. (See p. 26).

[140] DAVID R. A. RUELAS PAREDES. "Quantum state tomography for a polarization-path two-qubit optical system". M.Sc. thesis, Pontificia Universidad Católica del Perú, Lima, Peru, 2019. (See p. 27).

[141] PHILIP WALTHER et al. "Experimental one-way quantum computing". *Nature* **434**, 169 (2005). (See p. 37).

[142] L. DICARLO et al. "Demonstration of two-qubit algorithms with a superconducting quantum processor". *Nature* **460**, 240–244 (2009). (See p. 37).

[143] B. P. LANYON et al. "Simplifying quantum logic using higher-dimensional Hilbert spaces". *Nature Physics* **5**, 134–140 (2009). (See p. 37).

[144] ROBIN BLUME-KOHOUT. "Optimal, reliable estimation of quantum states". *New Journal of Physics* **12**, 043034 (2010). (See pp. 38, 39).

[145] ROBIN BLUME-KOHOUT. *Robust error bars for quantum tomography*. 2012. `http://arxiv.org/abs/1202.5270` (see pp. 38, 39).

[146] CHRISTIAN SCHWEMMER et al. "Systematic Errors in Current Quantum State Tomography Tools". *Physical Review Letters* **114**, 080403 (2015). (See pp. 38, 39).

[147] U. FANO. "Description of States in Quantum Mechanics by Density Matrix and Operator Techniques". *Reviews of Modern Physics* **29**, 74–93 (1957) . (See p. 43).

[148] HUANGJUN ZHU and MASAHITO HAYASHI. "Efficient Verification of Pure Quantum States in the Adversarial Scenario". *Physical Review Letters* **123**, 260504 (2019). (See p. 44).

[149] ZIHAO LI, YUN-GUANG HAN, and HUANGJUN ZHU. "Efficient verification of bipartite pure states". *Physical Review A* **100**, 032316 (2019). (See p. 44).

[150] KUN WANG and MASAHITO HAYASHI. "Optimal verification of two-qubit pure states". *Physical Review A* **100**, 032315 (2019). (See p. 44).

[151] SAM PALLISTER, NOAH LINDEN, and ASHLEY MONTANARO. "Optimal Verification of Entangled States with Local Measurements". *Physical Review Letters* **120**, 170502 (2018). (See p. 44).

[152] MAX S. KAZNADY and DANIEL F. V. JAMES. "Numerical strategies for quantum tomography: Alternatives to full optimization". *Physical Review A* **79**, 022109 (2009). (See pp. 44, 71).

[153] F. DE ZELA. "Role of weak values in strong measurements". *Physical Review A* **105**, 042202 (2022). (See p. 46).

[154] F. DE ZELA. "Weak Values in Strong Measurements". In *Proceedings of the 11th International Conference on Mathematical Modeling in Physical Sciences (IC-MSQUARE 2022)*. AIP. (See p. 49).

[155] BERTHOLD-GEORG ENGLERT, CHRISTIAN KURTSIEFER, and HARALD WEINFURTER. "Universal unitary gate for single-photon two-qubit states". *Physical Review A* **63**, 032303 (2001). (See pp. 49–51).

[156] R. SIMON and N. MUKUNDA. "Minimal three-component SU(2) gadget for polarization optics". *Physics Letters A* **143**, 165–169 (1990). (See p. 50).

[157] RAJENDRA BHANDARI and TARAKESHWAR DASGUPTA. "A spin-1/2 interferometer using light beams". *Physics Letters A* **143**, 170–175 (1990). (See p. 50).

[158] T. DURT, BERTHOLD-GEORG ENGLERT, INGEMAR BENGTSSON, and KAROL ŻYCZKOWSKI. "On mutually unbiased bases". *International Journal of Quantum Information* **08**, 535–640 (2010). (See p. 55).

[159] IFAN HUGHES and THOMAS HASE. *Measurements and their Uncertainties: A practical guide to modern error analysis*. Oxford University Press, USA, 2010. (See p. 57).

[160] MEHUL MALIK et al. "Direct measurement of a 27-dimensional orbital-angular-momentum state vector". *Nature Communications* **5**, 3115 (2014). (See pp. 66, 67).

[161] J.S. LUNDEEN and K.J. RESCH. "Practical measurement of joint weak values and their connection to the annihilation operator". *Physics Letters A* **334**, 337–344 (2005). (See p. 66).

[162] CLAUDIA BENEDETTI et al. "Experimental estimation of quantum discord for a polarization qubit and the use of fidelity to assess quantum correlations". *Physical Review A* **87**, 052136 (2013). (See p. 70).

[163] MATTEO BINA, ANTONIO MANDARINO, STEFANO OLIVARES, and MATTEO G. A. PARIS. "Drawbacks of the use of fidelity to assess quantum resources". *Physical Review A* **89**, 012305 (2014). (See p. 70).

[164] ANTONIO MANDARINO, MATTEO BINA, STEFANO OLIVARES, and MATTEO G. A. PARIS. "About the use of fidelity in continuous variable systems". *International Journal of Quantum Information* **12**, 1461015 (2014). (See p. 70).

[165] ANTONIO MANDARINO et al. "Assessing the significance of fidelity as a figure of merit in quantum state reconstruction of discrete and continuous-variable systems". *Physical Review A* **93**, 062118 (2016). (See p. 70).

[166] H. HÄFFNER et al. "Scalable multiparticle entanglement of trapped ions". *Nature* **438**, 643–646 (2005). (See p. 71).

[167] DAVID GROSS et al. "Quantum State Tomography via Compressed Sensing". *Physical Review Letters* **105**, 150401 (2010). (See p. 71).

[168] STEVEN T. FLAMMIA, DAVID GROSS, YI-KAI LIU, and JENS EISERT. "Quantum tomography via compressed sensing: error bounds, sample complexity and efficient estimators". *New Journal of Physics* **14**, 095022 (2012). (See p. 71).

[169] GREGORY A. HOWLAND, DANIEL J. LUM, and JOHN C. HOWELL. "Compressive wavefront sensing with weak values". *Optics Express* **22**, 18870–18880 (2014). (See p. 71).

[170] Z. SHI et al. "Scan-free direct measurement of an extremely high-dimensional photonic state". *Optica* **2**, 388–392 (2015). (See p. 71).

[171] XUANMIN ZHU and QUN WEI. "Direct state tomography using continuous variable measuring device". *Annals of Physics* **376**, 283–295 (2017). (See p. 71).

[172] XUANMIN ZHU et al. "Adaptive quantum state tomography via weak value". *Results in Physics* **31**, 104999 (2021). (See p. 71).